POLITECNICO
MILANO 1863

SCUOLA DI INGEGNERIA INDUSTRIALE
E DELL'INFORMAZIONE

Synthesis and characterization of magnetron sputtered $ZnSnN_2$ thin films for novel photovoltaics

TESI DI LAUREA MAGISTRALE IN

Materials Engineering and Nanotechnology
Ingegneria dei materiali e delle nanotecnologie

Author: **Davide Giughello**

Student ID: 988149
Advisor: Prof. David Dellasega
Co-advisor: Dr. Cristina Mancarella
Dr. Davide Vavassori
Academic Year: 2022-2023

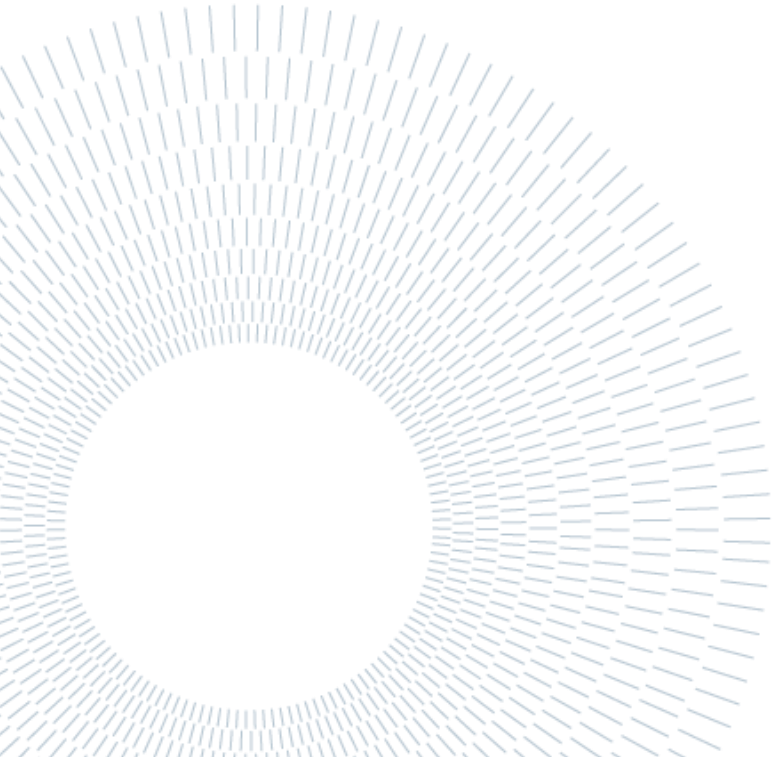

That you are here,
That life exists and identity,
That the powerful play goes on, and you
may contribute a verse.

O Me! O Life!
Walt Whitman

It's all about the people.

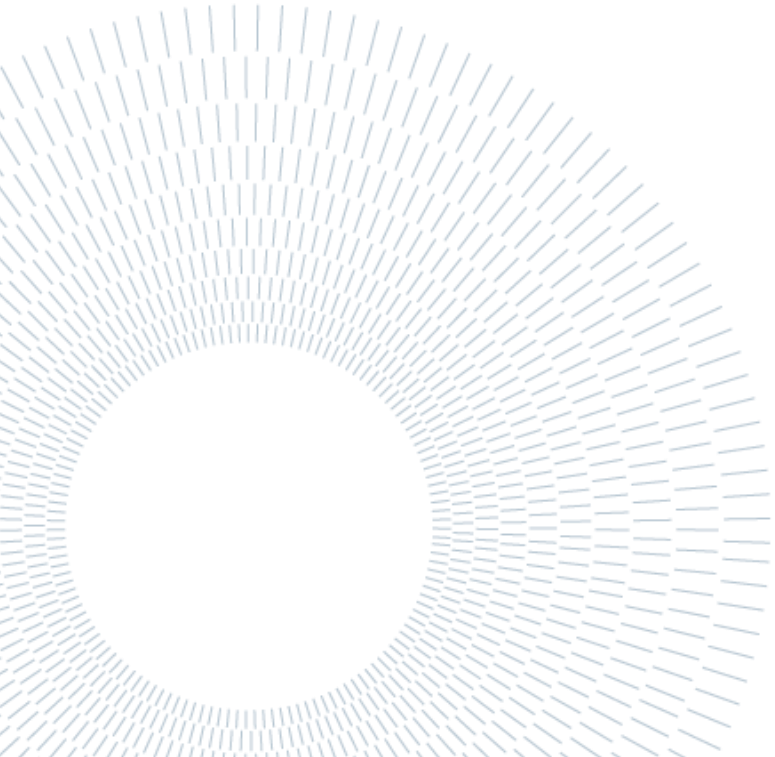

Abstract

Nowadays harnessing the solar energy through photovoltaics applications is considered one of the most promising paths to meet the escalating demand for energy. To exploit most of the solar spectra, engineered devices are needed, and tandem solar cells represent an innovative approach within the field of photovoltaics. For this purpose, a new type of semiconductor has captured the attention of the scientific community, $ZnSnN_2$, mostly known as ZTN. Is made of earth-abundant, cheap, and non-toxic elements, these characteristics make it an excellent candidate for photovoltaics application. The optoelectronic properties of ZTN primarily depend on its composition and since it shows a high intrinsic carrier concentration, the understanding of carrier tuning is of paramount importance for the development a performant device. Moreover, the bandgap can be tuned accordingly to the disorder of the structure. It is a relatively new material since it was first synthesized in 2013, from that time on, different techniques were implied to fabricate ZTN but in this work the Magnetron Sputtering in Direct Current regime is utilized. To have a precise control of the film's composition, two independent cathodes of tin and zinc were utilized. The films are deposited within a high vacuum chamber filled with nitrogen. This research is aimed to understanding the correlation between different deposition conditions and the related material properties. In this work the role of zinc content, gas pressure, and growth temperature on the morphology, vibrational modes and optoelectronic properties will be analyzed. A total of 31 samples were deposited featuring different Zn/(Zn+Sn) composition and were characterized through SEM, EDXs, XRD, Raman and optoelectrical measurements. Moreover, a particular attention was given toward the oxidation process in zinc rich samples. In this research are shown the correlation between the Zn/(Zn+Sn) on the material's structure as well as the bandgap value. Is intended to be an explorative research project, giving a solid base for future research as more branches were investigated.

Key words: magnetron sputtering, thin films, ZTN, tandem solar cells, bandgap tuning.

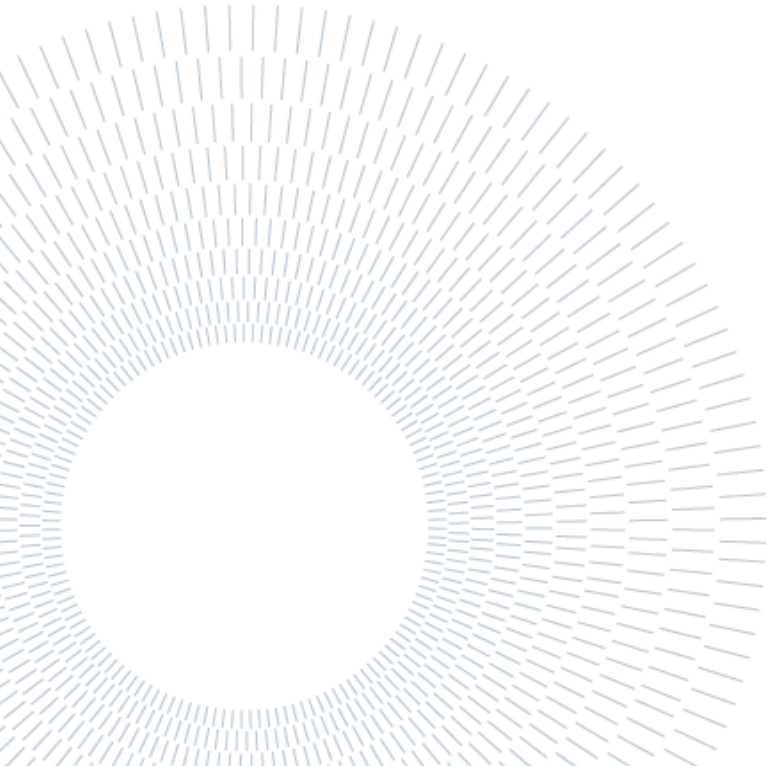

Sommario

Attualmente, utilizzare l'energia solare tramite il fotovoltaico è considerato uno dei percorsi più promettenti per soddisfare la crescente domanda di energia. Per sfruttare la maggior parte dello spettro solare, sono necessari dei dispositivi innovativi e le celle solari tandem ne sono un esempio. A tale scopo, un nuovo tipo di semiconduttore ha attirato l'attenzione della comunità scientifica, lo ZnSnN2, noto principalmente come ZTN. Composto da elementi abbondanti sulla Terra, economici e non tossici, per questo, lo rendono un eccellente candidato per le particolari applicazioni fotovoltaiche. Le proprietà optoelettroniche dello ZTN dipendono principalmente dalla sua composizione e, poiché mostra una elevata concentrazione intrinseca di portatori, il controllo del loro sviluppo è di fondamentale importanza per ottenere un dispositivo performante. Inoltre, il bandgap può essere regolato in base al disordine della struttura. Si tratta di un materiale recentemente scoperto, sintetizzato per la prima volta nel 2013; da allora, sono state impiegate diverse tecniche per fabbricare lo ZTN, ma in questo lavoro viene utilizzato il Magnetron Sputtering in regime a Corrente Continua. Per avere un controllo preciso della composizione del film, sono stati utilizzati due catodi indipendenti di stagno e zinco. I film sono depositati all'interno di una camera ad alto vuoto riempita di azoto. Questa ricerca mira a comprendere la correlazione tra diverse condizioni di deposizione e le relative proprietà del materiale. In questo lavoro, verrà analizzato il ruolo del contenuto di zinco, della pressione del gas e della temperatura di crescita sulla morfologia, le modalità vibrazionali e le proprietà optoelettroniche. Sono stati depositati complessivamente 31 campioni con diverse composizioni di Zn/(Zn+Sn) e sono stati caratterizzati tramite SEM, EDX, XRD, Raman e misurazioni ottiche ed elettriche. Inoltre, è stata prestata particolare attenzione al processo di ossidazione nei campioni ricchi in zinco. In questa ricerca vengono mostrate le correlazioni tra Zn/(Zn+Sn) sulla struttura del materiale e sul valore del bandgap. Si tratta di un progetto di ricerca esplorativo, che fornisce una solida base per ricerche future in quanto sono stati esplorati diversi rami.

Parole chiave: magnetron sputtering, film sottili, ZTN, celle solari tandem, bandgap.

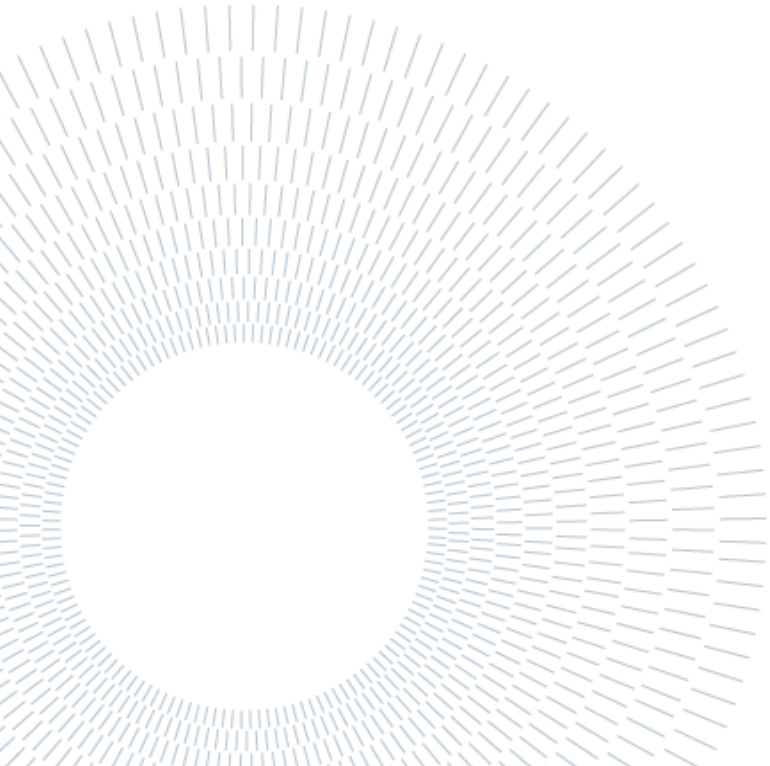

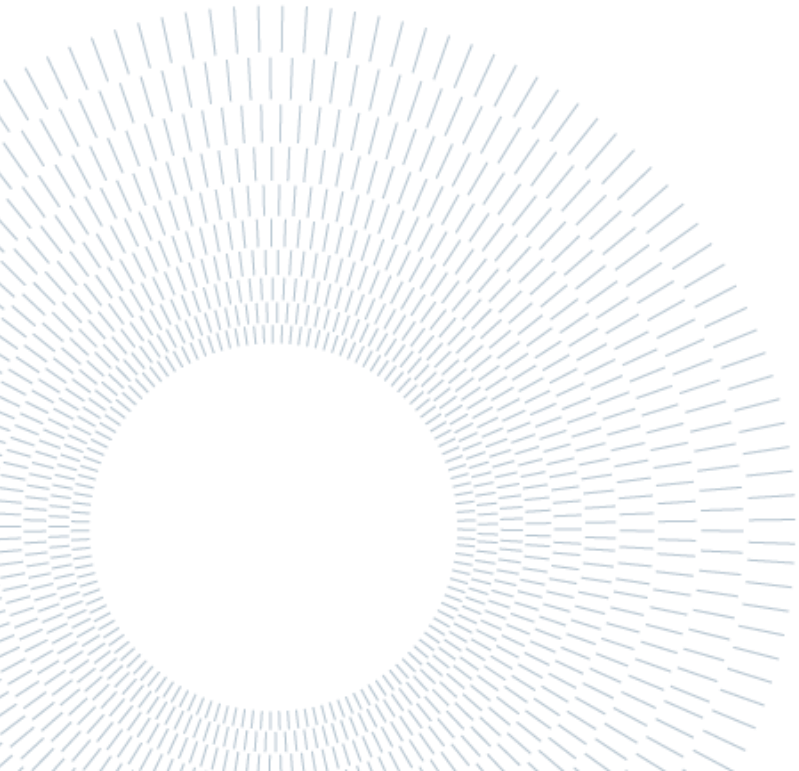

Contents

1 Materials for photovoltaics

This chapter is intended to give a complete vision of the materials used for photovoltaics world. A brief explanation of the semiconductor class of materials is given, aiming the attention to p-n junctions, the simplest device used in solar cells application. Then the focus will move toward the promising class of ternary nitride which the $ZnSnN_2$ is a part.

1.1. Semiconductors

Semiconductors are a variety of materials that show a gap between the conduction band and the valence band less than 5 eV [1]. They possess characteristics in between metals and insulators: metals have no energy gap, and the electrons are free to move allowing a high conductivity. Insulators exhibit a very high bandgap and have no free electrons, so the conductivity Is equal to zero. Semiconductors instead relies on free electrons and a little bandgap in order to be conductive. These qualities put semiconductors as best candidates in electronic applications such as transistor or solar cells [1], [2].

To be conductive, the semiconductors must have free carriers such as electrons in conduction band or holes in valence band. At 0 K al the electrons occupies the valence band, and that level is called Fermi energy level. Thermal energy at room temperature can excite the electrons rendering low-bandgap semiconductors conductive [1]. When considering a crystalline structure, the energy depends on the **k**-vector, that describes the momentum of an electron. So, the energy levels of conduction and valence bands are undulating and the difference between the minimum of conduction band and the maximum of valence band is the bandgap value (Figure 1.1). If the position of the minimum of conduction band matches with the maximum of valence band, the

semiconductor is labelled as direct, otherwise is indirect. When considering direct bandgap, only a photon is needed to excite the electron, if indirect also a phonon to change the momentum of the electron [1].

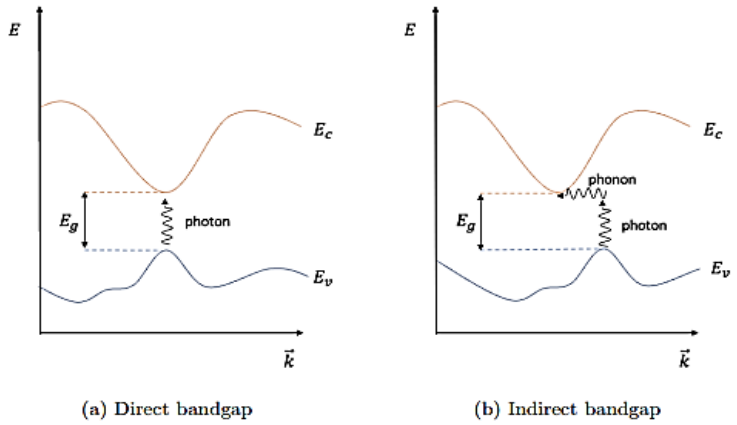

Figure 1.1: The figure (a) shows a direct bandgap energy, where the minimum of the conduction band is above the maximum of the valence band, the figure (b) shows an indirect bandgap, so the maximum of the valence band is shifted with respect to the minimum of the conduction band, hence a phonon take place in the reaction [1].

Although there is a little bandgap in semiconductors, charge carriers are of paramount importance for the material to be conductive [2].

The energy gap can be tuned controlling the career density [3] in the film thanks to the Burstein Moss shift (Figure 1.2) where the free electrons fill the conduction band.

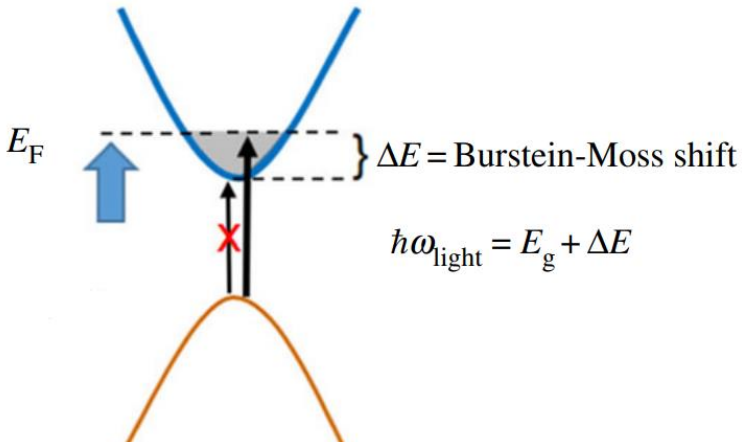

Figure 1.2: Illustration of Burstein-Moss effect due to band filling of the conduction band for a high carrier density, the Fermi energy level is shifted upward, resulting in an apparent increasing of optical bandgap [3].

That is an upward shifting of the energy gap, since the electrons could be promoted only with an energy higher than the initial energy gap [4]

In semiconductors, when electrons are excited thanks to phonon whose energy matches the bandgap energy, they move from the valence toward the conduction state leaving behind a hole. That create a coupling between the electron and it respective hole developing an electron hole pair. It is possible to dope (Figure 1.3) the material both positively or negatively for having a greater conductivity. When the material isn't doped, it's called intrinsic and the number of carriers at 0K are equal to zero. A higher temperature the number of carriers is given by the material's properties and this equation holds [4]:

$$n = p = n_i$$

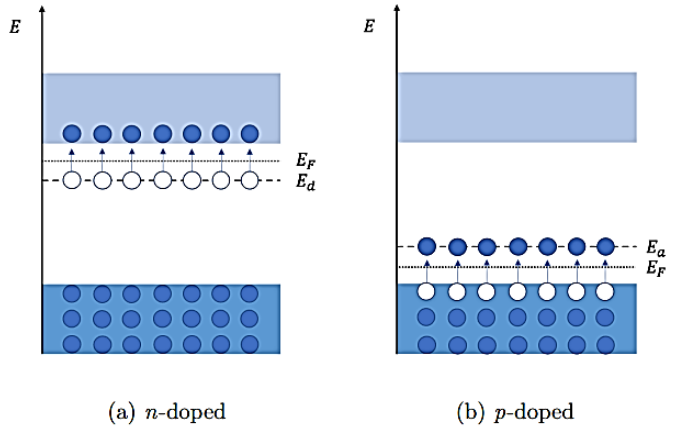

Figure 1.3: Shifting of the energy states due to partial occupation of electrons (a) or holes (b) for n-doped or p-doped condition respectively [1].

1.2. Photovoltaics: an overview

Nowadays solar energy is the cheapest form of energy that we can exploit on Earth. As the market is continuously growing, it is forecasted to be the largest form of energy source by 2035 [5].

Solar cells exploit semiconductors materials in order to transform the solar energy to produce electricity. The most basic solar cells are designed with a p-doped and a n-doped layer. If properly designed they can exploit photons to excite electrons and leave holes inside the valence band, these free carriers will move accordingly to a built-in potential thus creating current [6].

1.2.1. p-n junction

A p-n junction is a device that is constituted by the same material having opposite doping (p and n). The interface of these two charged regions is called p-n junction and exploits the separation of charges to be conductive. Devices as LED, transistor or solar cells relies on this principle. More in detail, at the interface, the negatively charged region led the electrons to diffuse in the positive region and vice versa for the holes. This region at the interface is called depletion region (W). Due to charge difference, an electric filed E is spontaneously created in W. At a certain point, the opposing effect of the drift current due to E and the diffusion current will annihilate each other, resulting in an absence of net current when in a state of equilibrium [1]

What happens to the Fermi energy levels is that for n-type the level is upshifted while for the p-type is downshifted. The difference between the conduction band of p-type and n-type is called built in potential, V_{bi} that is the potential to overcome to have the circulation of current.

1.2.2. Working principle

When a light ray strikes the surface of the material, the incident photons can be absorbed near the cell surface and every photon will give its energy to excite an electron, if the photon's energy matches the bandgap of the semiconductor, it will

move freely inside the material, leaving a hole. For indirect bandgap semiconductors, also a phonon that gives the momentum is needed to free an electron.

Electron – holes pair created near the junction are separated by a strong electric field. The minority carriers are swept across the interface and becomes majority carriers, each exchange contributes to the final output current. The efficiency limit intrinsic to a solar cell with only a single junction is first theorized in 1961 by Schokley and Queisser and is around 31.6% with an optical bandgap of 1.1 eV. (solar cells – 2004) In order to fully exploit the solar cells potentiality they need to absorb the majority of the solar spectrum and so the bandgap need to be engineered.

The performance is determined by minority carriers that are electrons and holes respectively for p-type and n-type semiconductors [6].

1.2.3. Tandem solar cells

New ways of solar harvesting need to be exploited such as multijunction [7] photovoltaics like tandem solar cells (Figure 1.4). New materials have to be found in order to reach high performances despite of the defects intrinsically present [5]. Tandem solar cells are designed to collect as many incidents photons as possible by exploiting different bandgaps that matches the solar radiation spectra [8].

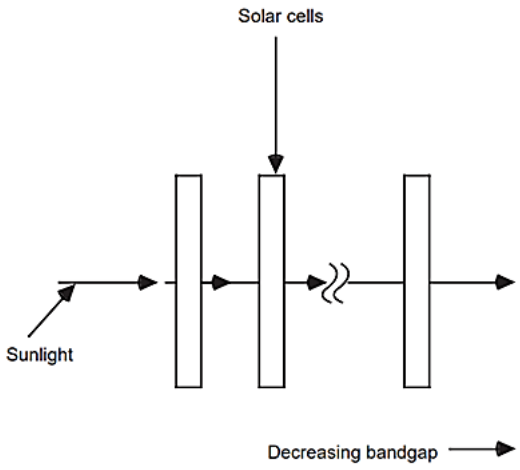

Figure 1.4: Coupling of solar cells based on the bandgap value in tandem solar cell [7] .

Basically, tandem solar cells, are a stacking of multiple p-n junction of different materials. To achieve the maximum gain, different bandgaps are needed in order to act on different wavelengths [6]. That is, the top cell exhibits a higher bandgap with respect to the bottom one. Therefore, the top layer absorbs the high energy photons while the lower absorb the lower energy photons [6], [8]. In the Figure 1.5 is shown the maximum range of absorption for a tandem solar cell, at maximum efficiency the top cell has a bandgap of 1.63 eV, while the bottom cell features a bandgap of 0.96 eV.

For having a better match between the different materials, a similar thermal expansion

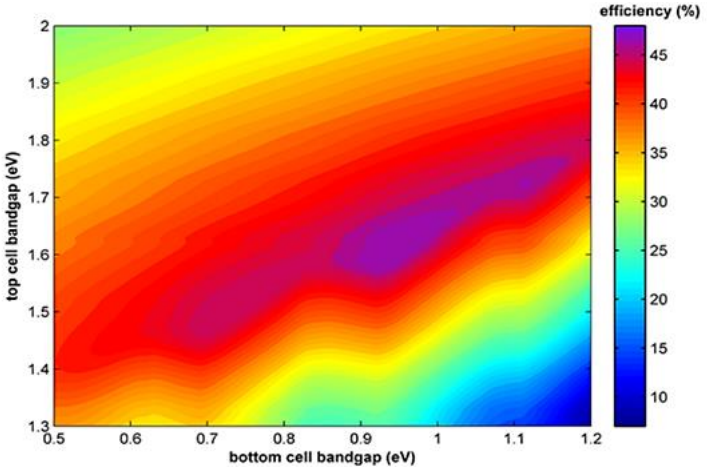

Figure 1.5: The efficiency of a tandem solar cells is shown based on the coupling of two different semiconductors that features two different bandgap values [8].

coefficient is needed, and the bandgap must be optimized for the solar spectrum [6]. The two solar cells have to work in different spectrum for enhancing the solar absorption that ideally matches [9] the AM1.5 spectra (Figure 1.6) that is a simulation of the terrestrial solar spectrum where the light hit directly the earth without any contribution of diffused rays. The spectral p-n junction model is introduced to assess the theoretical maximum efficiency of solar cells and provide data for the design of tandem solar cells [10].

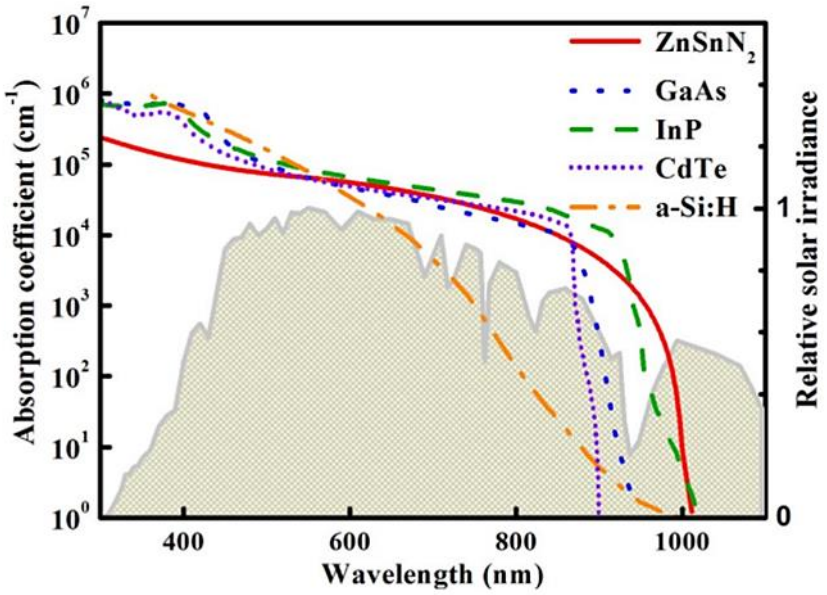

Figure 1.6: Graph of AM1.5 solar spectrum with corresponding absorption coefficient for different materials: $ZnSnN_2$, GaAs, InP. CdTe and a-Si:H [9].

1.3. Towards II-IV-N_2

To fulfil the annual demand of energy, converting sunlight into electricity seem to be the most promising path to be follow. Semiconductors for photovoltaics must possess some requirements such as affordability, good scalability without constraints and efficiency. An outstanding class of materials are nitrides that shows a mixed covalent/ionic bonding properties since they're in between the more ionic oxides (*e.g.*, GaO) and the more covalent pnictides (*e.g.*, GaAs, $InGaP_2$). This ionic behavior permits increased tolerance to structural defects due to the proximity of the constituent atomic orbitals to the band edge. Therefore, when breaking the atomics bonds, the defect states that arise would be shallower. The fact that nitrides are more covalent than oxides, transmute in a better hybridization while improving charge transport properties [11]. They are worth studying since their degree of ionic characters show a great tolerance towards structural defects because of the atomic orbitals proximity to the band edges and the partially covalent character. The main reason is that the high energy of 2p nitrogen orbital result in a better hybridization with metal orbitals giving to lower bandgap [12].

1.3.1. Nitride semiconductors

Today the family of binary III nitrides found their application as semiconductors thanks to the tunability of the bandgap value ranging from the ultraviolet to infrared spectrum, they are largely used in photovoltaics, for photo detection or as LEDs [13]. Most known material of this family is InGaN that absorb most of the solar spectrum. Some disadvantages that hinder the worldwide spreading of this material is the high cost of raw materials, as well as the difficulty of a large-scale production due to the peculiar deposition methods. Moreover, the problem that arises during fabrication as phase segregation must be considered. The phase segregation is faced in rich In-Alloys due to lattice mismatch of InN and GaN. Moving toward a more sustainable route for semiconductor industry, the promising class of II-IV-N_2 is considered (Figure 1.7). Even if the performances are quite lower, the gain stands in the availability of the materials. Hence the III metal is replaced by a Zinc and an IV element [1]. Above all $ZnSnN_2$, $ZnGeN_2$ and $ZnSiN_2$ are the most promising since they're made of earth-abundant, non-toxic, and cheap material. Furthermore, they're easier to fabricate due to more accessible techniques such as sputtering [14]. $ZnGeN_2$ structure is very similar to that of $ZnSnN_2$ and is expected to be wurtzite in most of experiments [15]. The effect of the deposition parameters is analyzed increasing the growth temperature of $ZnGeN_2$ an increasing in crystallinity degree is obtained [1]. Considering the optical properties, the controlling of cation disorder is expected to modify the bandgap [16].

$ZnGeN_2$ was the first material to be created in 1970 while $ZnSiN_2$ was synthesized in 1992. The less studied semiconductor of this group is $ZnSnN_2$ that was first synthesized in 2013 [17], [18]. That explain why there's a little literature and a great interest in studying this fascinating material. To give an idea, there is more than an order of magnitude more oxides than nitrides in crystallographic databases [19].

Both $ZnSnN_2$ and $ZnGeN_2$ are n-type semiconductor [20], but the latter has a lower carrier density. This is a desired characteristic in semiconductors since the risk of a degeneracy of carrier need to be avoided [1]. $Zn(Si,Ge,Sn)N_2$ materials have a bandgap that can be tuned in the range of 1 to 5 eV [11].

Another family of semiconductors that resemble $ZnSnN_2$ are Kesterites and Delafossites. Ternary nitride materials such as $CuTaN_2$ and $CuNbN_2$ crystallize in the layered delafossites crystal and found their application as p-type transparent conducting oxides. $CuTaN_2$ shows an indirect bandgap of 1.3 eV, thanks to its absorption coefficient higher than 10^5 cm^{-1} above 1.5 eV it can be used in applications where ultrathin absorber layers are necessary. While $CuNbTa_2$ shows an indirect bandgap of 0.9 eV, a further study on tunable $Cu(Nb,Ta)N_2$ is suggested.

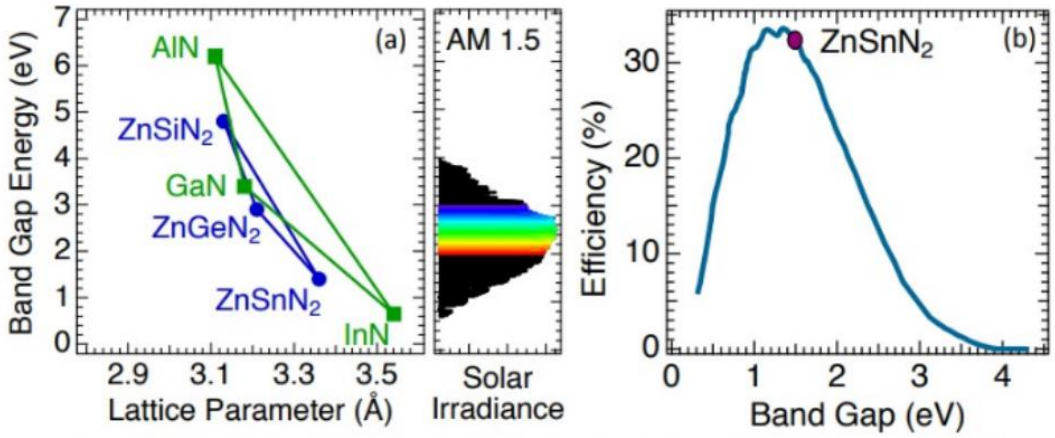

Figure 1.7: (a) Bandgap value versus lattice constant of III-N semiconductors and their ternary II-IV-N_2 analogs with AM1.5 solar spectrum. (b) Efficiency for $ZnSnN_2$ based on calculated Shockley-Queisser limit for a single junction solar cell [4][20].

In particular, the structure of $ZnSnN_2$ is similar to the kesterite tetragonal Cu_2ZnSnS_4 [11]. CZTS thin films are made of earth abundant and non-toxic materials. Due to their high absorption coefficient in the order of 10^4 cm^{-1} with an optimal bandgap of 1.4 eV, kesterites are promising candidates for solar cells [21]. Alloying CZTS with Se and Ge successfully boost the performances and allow for a better tailoring of the bandgap. In the last year, research done on CZGSe (without Sn) shows efficiencies up to 8.5%.

1.3.2. $ZnSnN_2$ applications

Films of $ZnSnN_2$ can serve as semiconductors for either photovoltaic applications or for LEDs. The main difference between these two functions is that when considering Solar cells, a separation of photogenerated holes and electrons is needed while in LEDs the carrier must be delimited at the same interface [13]. The main limitation that

hinders the development of a p-n junction using ZnSnN2 is the degenerate carrier density, that for film made with DC magnetron sputtering, is reported to be in the range of 10^{20} cm^{-3}. So, to decrease the carrier density a post annealing treatment is necessary, giving a carrier concentration of 10^{17} cm^{-3}. Treated films can be used coupled with Si as p material to form a heterojunction solar cell. To make the contact semiconductor/electrodes, two strips made by Ni/Au are deposited on Si and then all the pieces undergo to a post annealing treatment [22].

A theoretical model proposed by Arca et al. based on a ZnSnN2/Mg:$CuCrO_2$ solar cell shows an efficiency of 23%, if considering a defect free material [23]. ZnSnN2 can be used also coupled with InGaN for the development of quantum wells for high-efficiency orange light emitting diodes [24]. A numerical study based on tandem $CuCrO_2$ – ZTN solar cells highlight an efficiency up to 23% In the limit of no defects present.

ZTN can find application also in gas sensing, it is used to detect NH_3 in several context such as pharmaceutical or food process industries. The sensing device can detect the presence of a certain gas due to a change in material's resistance inside the sensor. $ZnSnN_2$ has the capability of tracing Ammonia. NH_3 is a colorless gas, harmful for human body and reactive towards water. Ammonia is widespread in refrigerants, textile and pharmaceutical, only to cite a few. Detectors made of ZTN fabricated via CVD on glass substrate using metal as contacts [25].

1.3.3. Experimental studies on $ZnSnN_2$

$ZnSnN_2$ films were synthesized with various techniques starting a decade ago, here some fundamental research is presented (Figure 1.8). In 2013 the material was fabricated by three different group's researchers using different methods, Plasma assisted solid vapor liquid deposition [26], molecular beam epitaxy and radiofrequency sputtering. As the first researchers discovered that this novel semiconductor strongly modifies its properties when deposited with different deposition conditions, each parameter as the temperature, the pressure and the

composition of the film gained a lot of attention [12]. $ZnSnN_2$ is predicted to exhibits different structure based on the intrinsic cation disorder of the material. In 2014 a group of research synthesized ZTN stoichiometric films using plasma assisted molecular beam epitaxy and, even if the most favorable structure is the orthorhombic one, only the monoclinic structure was shown by the samples due to lattice disorder [27].

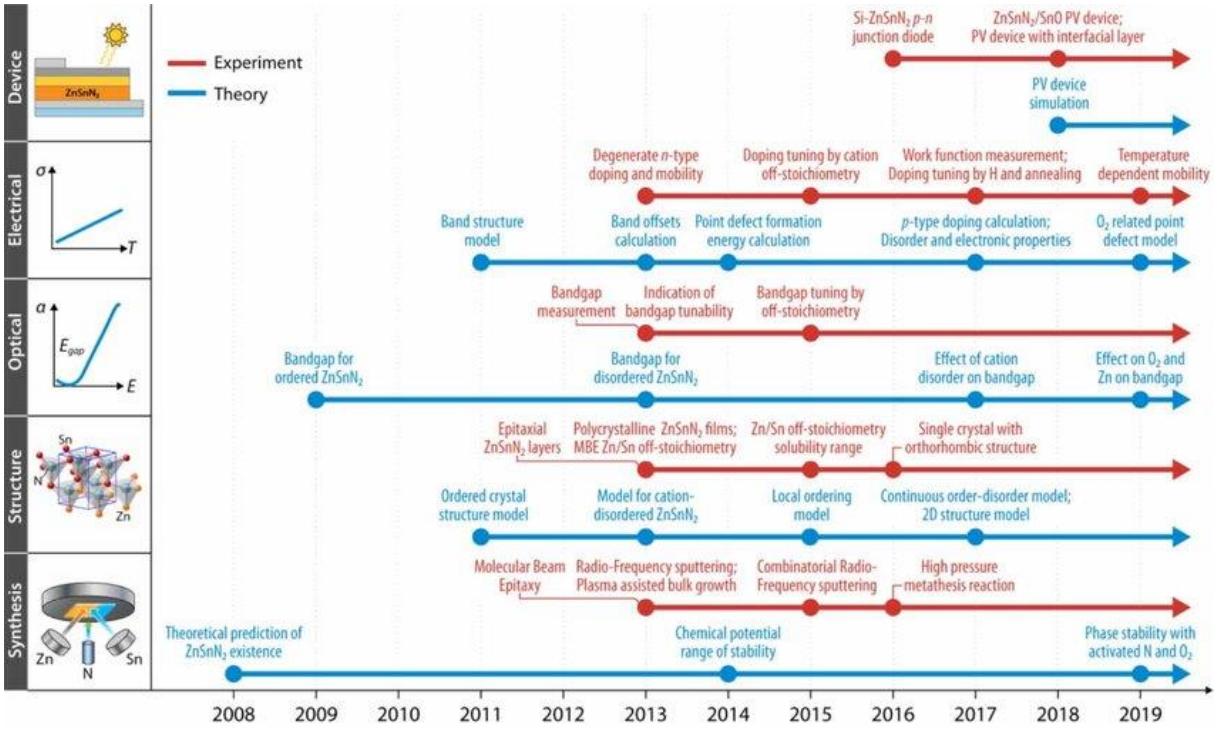

Figure 1.8: Key stages in studies and syntesis of ZTN films from 2008 to 2019 [12].

Experimentally is very difficult to synthesize a precise film with a precise structure since various parameters needs to be taken into consideration, hence the most shown structure is the disordered wurtzite. The orthorhombic ZTN was first [19] fabricated using plasma assisted vapor deposition on Lithium Gallate substrates. $LiGaO_2$ has an orthorhombic structure that helps the formation of pure single crystal Pna21 phase of $ZnSnN_2$. With Yttria Stabilized Zirconia (111) as substrate, at 550°C a switch in phase from wurtzite to orthorhombic is observed [28].

The parameter that most influences the properties of the material is the Zinc/(Zinc+Tin) ratio inside the deposited film. The effect of over-stoichiometry in zinc

is investigated, showing a lower carrier concentration in the film [29]. Research on the off stoichiometric ZTN films were conducted by Wang et al. using reactive sputtering.

The results are very promising since their off stoichiometric zinc films with 0.72 Zn/Zn+Sn ratio shows a low carrier concentration of 2.7 * 10^{17} cm^{-3} at 300K in ultrahigh vacuum with a partial pressure of nitrogen of 1.56 Pa [29]. Through the last decade all the synthesis method led to a carrier concentration that span over 10^{16} to 10^{21} cm^{-3}, showing a n-type intrinsic doping [30]. The bandgap achieved range from 1.0 eV to 2.0 eV accordingly to Density Functional Theory (DFT) [31].

1.4. $ZnSnN_2$: Material properties

$ZnSnN_2$ exhibits features of semiconductors for having a bandgap but also has free electron in the conduction band [18]. Based on the information found in the literature, $ZnSnN_2$ has the potential to form crystalline structures in various arrangements (Figure 1.9): orthorhombic *Pna2₁*, orthorhombic *Pmc2₁*, hexagonal *P6₃mc* or monoclinic [15], [32][18]. However, there are different hypothesis on the exact structure shown by ZTN, that's why a further investigation is needed. Some researchers state that phase remains orthorhombic for both ordered and disordered phases with a mixture of the two Pna21 and Pmc21 orthorhombic phases for disordered materials [18].

1.4.1. Structure

The ordering atoms of the sublattice must locally satisfy the charge neutrality, that is known as octet rule. While forming alloys of binary compounds usually shows disordered structure, ternary compounds tend to arrange in an ordered form. During the last years the study of $ZnSnN_2$ structure has gained importance in order to better tailor the material for photovoltaics applications, since it affect the bandgap value. For $ZnSnN_2$ and $ZnGeN_2$ the parent binary materials are the III nitrides, and the phase is wurtzite, a hexagonal crystal [15] , [27].

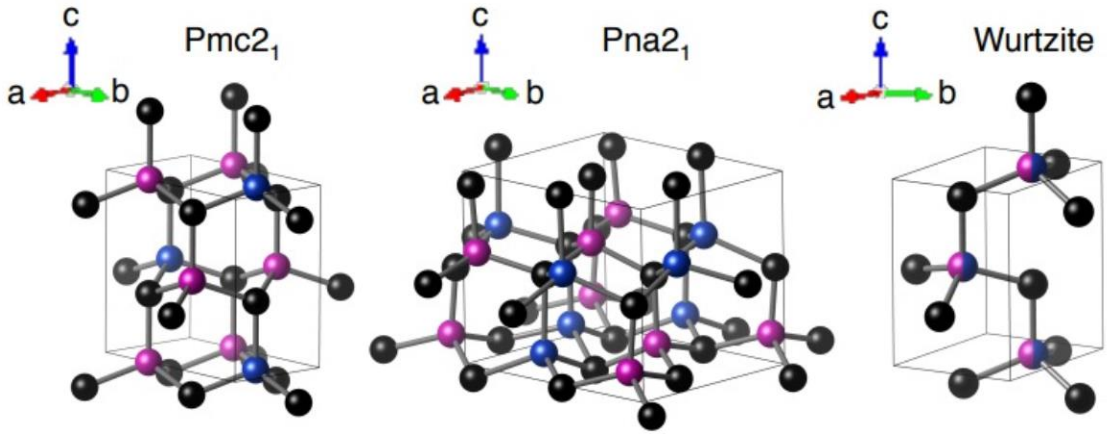

Figure 1.9: The arrangement of Pmc21 ordered structure only theorized but never claimed experimentally, (b) structure of most stable Pna21 arrangement observed experimentally and (c) disordered wurtzite structure composed by a repetition of Zn and Sn atoms in the cation sub-lattice [4].

Based on Density functional theory, $ZnSnN_2$ shows orthorhombic features when fully ordered while wurtzitic structure when fully disordered [28]. There are two high symmetry ways to alternate the Zn and Sn atoms in cation sublattice, orthorhombic Pmc21 and Pna21 space groups. These two groups are difficult to distinguish with experiments since they differ only in the planar ordering of Zn and Sn atoms [33]. The first recognized structure consists with a unit cell of 16 atoms that shows orthorhombic symmetry, when structural constraints are applied, this led to a superstructure. The relation between Pna21 superstructure and wurtzite is $\mathbf{a}_o = 2\mathbf{a}_w1$, $\mathbf{b}_o = \mathbf{a}_w1 + 2\mathbf{a}_w2$, $\mathbf{c}_o = \mathbf{c}_w$ where w stands for wurtzite and o for orthorhombic. There is another possible structure, based on 8-atom per unit cell, and its superstructure is the Pmc21. This relation holds: $\mathbf{a}_o = \mathbf{a}_w1$, $\mathbf{b}_o = \mathbf{a}_w1 + 2\mathbf{a}_w2$, and $\mathbf{c}_o = \mathbf{c}_w$. Calculated formation energy for ZnSnN2 structures shows the same value for both the superstructures [15]. The lattice structure of the wurtzite-based II-IV-N2 nitrides is derived from the III-N wurtzite structure where pair of group-III elements is substituted with a Zn Atom and a group IV atom [12] First principle method's calculations indicate that the most energetically favorable structure of ZTN is the orthorhombic β-$NaFeO_2$ corresponding to the Pna21 space group [17], [26], [29]. Even if in theory the most stable structure is orthorhombic, when synthesizing the Zinc Tin Nitride films, the two most showed structure are wurtzite-like [29] and monoclinic structure that derives from a partially ordered cation sublattice typical of wurtzite [34].

A better distinction between the ordered orthorhombic structure and the average wurtzite structure (based on a random arranging of Zn and Sn atoms) can be done with an XRD analysis. However, experimentally, the orthorhombic structures are very rare to obtain.

Another structure can be found in $ZnSnN_2$ that doesn't preserve the local charge neutrality and is labelled as Pm31 that shows a high formation energy and a lower bandgap with respect to Pna21 and Pmc21. Random configuration of this structures lead to a disordered polytype, while regular arrangements lead to ordered polytype. With high temperature during growth, the ordered structure is more prone to form

due to the increase of cation mobility [15]. Furthermore, a randomly placed cation structure led to a monoclinic structure [35].

As mentioned previously the structure's order plays a significant role when considering the bandgap, in fact the ZTN films that have a greater cation disorder shows the lower fundamental band gap while films with less cation disorder shows the higher fundamental band gap. Monoclinic ZTN shows a bandgap of 1.12 eV while that of fully orthorhombic is equal to 2.09 eV [35].

1.4.2. XRD analysis

When considering a thin film, the crystalline structure is of paramount importance to characterize the material and Xray diffraction is the most used method to obtain information on crystalline phases. $ZnSnN_2$ exhibits seven peaks while performing Xray diffractometry, more precisely located at 30.6°, 32.7°, 34.9°, 45.8°, 54.7°, 60.0°, and 65.0° [22]. Since this material features different types of cations sublattice ordering, the XRD data must be discerned as seen in Figure 1.10. As seen, the peaks of wurtzite and orthorhombic, are superimposed and they can be distinguished to peaks related at lower degree (<30°) or by seeing a peak splitting at 30,6° or 34,9°.

With a post annealing treatment, the peak related to 32.7° slightly increase since the grain size became bigger, from 13.1 to 14.7 nm. These results are in good agreement with Scherrer analysis performed on the XRD spectra [22]. This trend is also found in a previous work by Fioretti et al. were the 32.7° peak increase with increasing the temperature.

Peaks located in the range of 30° to 35° became sharper when increasing the Zinc content. The XRD's samples that features a ratio between 0.45 and 0.70 in Zn/Zn+Sn grown at 120-340°C displays the same wurtzite structure with no evident differences in position or broadening that can be related to other secondary phases such as Zn_3N_2 or Sn_3N_4 [18]. As deposited films show instead a very low intensity and broad bands over 45°. It suggests that post annealing treatment could be beneficial for obtaining a more crystalline structure.

The structure is difficult to precisely determine the structure only with x-ray-diffractometry measurements, in particular Paul Quayle et al. observed through an X-ray diffraction measurement a wurtzite structure, but the value energy gap obtained with photoluminescence is very close to the energy gap typical of a Pna21 structure. This suggests that the lattice disorder found in the XRD spectra is related not to a disordered arrangement of cations but from a controlled repetition of sublattices that locally preserve the charge neutrality. (charge neutral disorder) That is XRD spectra can shows wurtzitic structure not only when the structure has a complete random

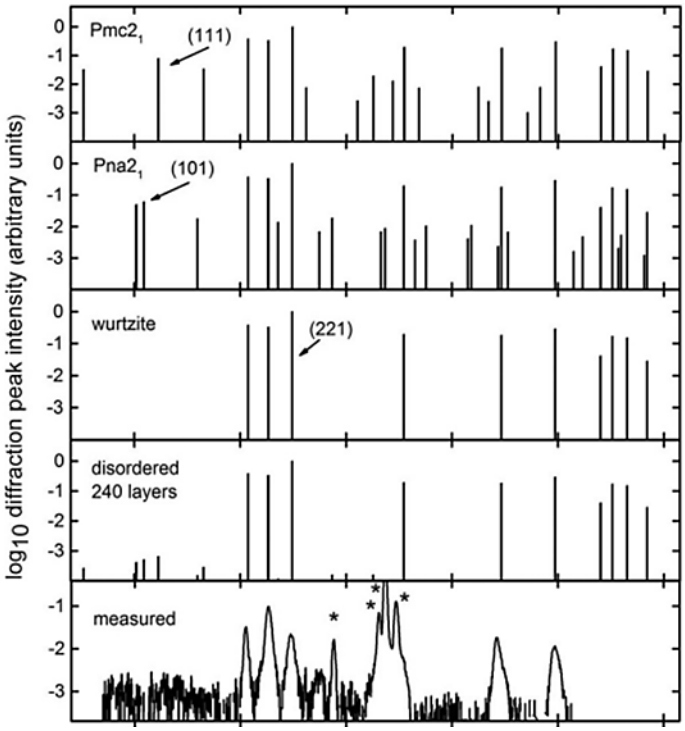

Figure 1.10: Calculated Xray diffraction spectra for orthorhombic $ZnSnN_2$ with Pmc21 and Pna21 arrangement and wurtzite structure, a pattern for a crystal composed of 240 pseudospin layers with a 50:50 mixture of the Pna21 and Pmc21 structure and a measured spectrum [15].

cation arrangement but also when the two sublattices that respect the octet rule are randomly placed [15].

Moreover, the crystallinity of the film is modified by the substrate's lattice [9]. There is a correlation also between the power applied to cathodes and the structure itself. In

a work presented by Ye et al. a series of ZTN films were deposited using RF sputtering technique using a Zn/Sn alloy target (3:1), with a power of 35 W at room T no peaks can be observed in the XRD spectra while they are clearly shown when the substrate temperature reaches more than 200°C or the sputtering power increase up to 50 W. This suggest that high sputtering power helps the crystallization of the film [36].

As stated before, obtaining the orthorhombic structure is very challenging and few experimental spectra are available. A work of Alnjiman et al. hypothesized their DC-sputtered film to be orthorhombic in the $Pna2_1$ phase according to two matching peaks, but further investigation is needed to better classify the peaks [32]. Lahourcade et al. claims to have fabricated orthorhombic $Pna2_1$ ZnSnN2 films, according to XRD's spectra [37]. Moreover, the peaks related to the first two peaks found in 30-35° region appears when Zn/(Zn+Sn) increases [18] and a broadening of 34.6° peak occurs [34].

1.4.3. Raman analysis

In 2008 was presented a theoretical study on phonon density of Zn-IV-N_2 compounds, including $ZnSnN_2$ using a density-functional perturbation theory. What it can be achieve by considering the phonon dispersion in Figure 1.11 is that there are four

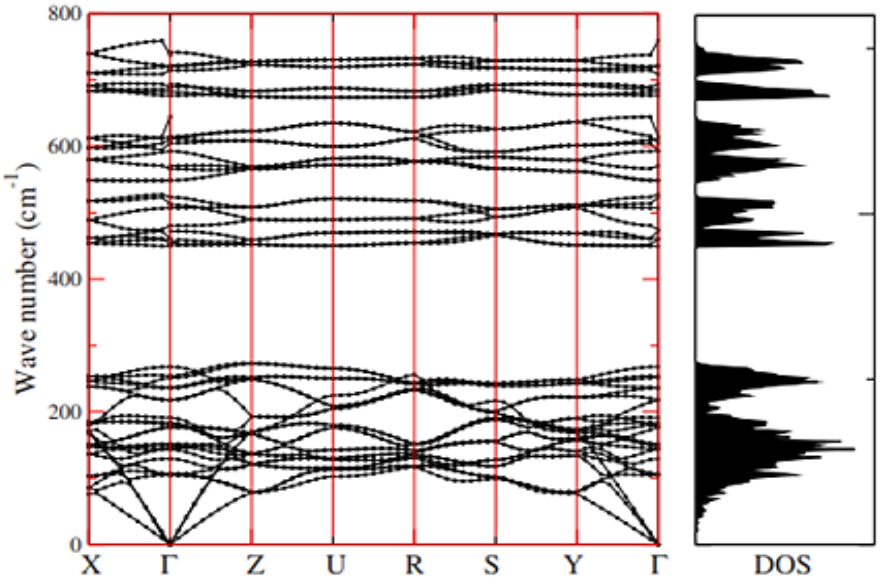

Figure 1.11: Phonon dispersion and density of states exhibits by $ZnSnN_2$ [38].

separate branches. The top of the acoustic bands is related to folded Brillouin-zone-edge modes dominated by the heaviest atoms, hence Sn in $ZnSnN_2$.

Within this folded acoustic range, there are 24 bands present. In the identified transverse optic region (450-750 cm^{-1}) two main peaks can be observed. The first peak (450 cm^{-1}) situated at lower wave number could correspond to Zn-N bond, while the second peak situated near 690 cm^{-1} may be correlated to Sn-N bond. Zn-N is characterized by a longer bond and shows a weaker force constant; hence a lower frequency is observed [38]. However, the peaks are associated to different bonds in literature [31] and identifying the correct vibrational pattern for a specific bond is under investigation.

It's worth noting that none of the forecasted vibrational peak is matched during experiments, neither the prevalent one is observed in the fabricated ZTN film. In contrast, the Raman spectrum of $ZnSnN_2$ closely replicates the Gaussian broadened phonon density of states as seen in Figure 1.12. The obtained spectrum shows a phonon-glass-like structure, resulting in complete breakdown of the **k**-vector selection

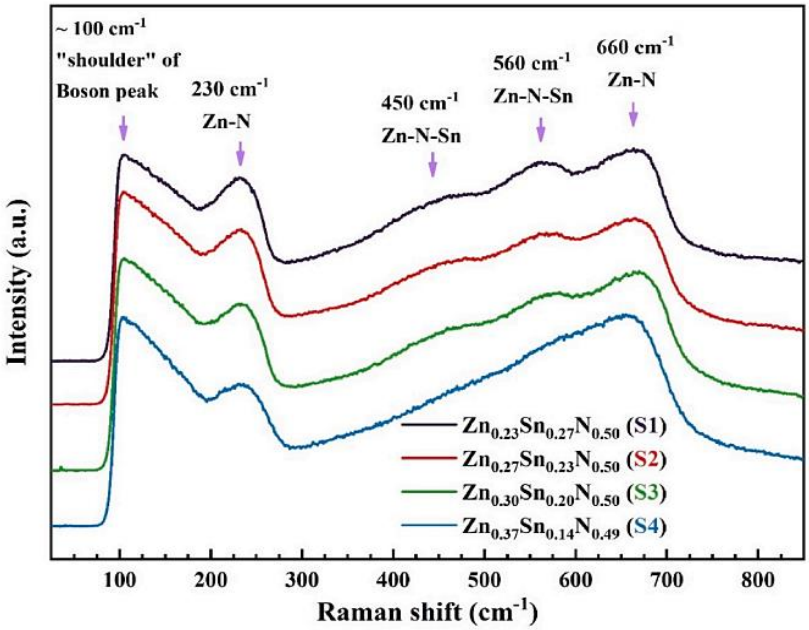

Figure 1.12: Vibrational modes of $ZnSnN_2$ with different film composition, each peak has a label that indicates the vibration of a precise bond [31].

rule. The sample obtained shows a complete disordered structure in XRD, unfortunately with Raman spectra it's not possible to determine the type of disorder [15].

Polycrystalline samples obtained by Ran et al. shows peaks slightly shifted than previous works. Investigated polycrystalline $ZnSnN_2$ samples possesses a Zn/(Zn+Sn) ratio of 0.6-0.85 and broader and shifted peaks appear, precisely at 236, 451, 556 and 654 cm^{-1} [34]. Through various experiments 4 broad bands at 230, 450, 560 and 660 cm^{-1} can be identified [31]. In accordance with findings from other experiments, [26] the peaks positions align with the calculated density of states [38].

It is worth noting that the peaks related to 450 and 560 cm^{-1} appears only when the Sn content is increased in the film [31]. The peaks corresponding to 230 and 660 cm^{-1} could be related to Zn-Sn-N_2 itself since none of the binary compounds shows that peak positions. As the Zn content increase up to 0.85 Zn/(Zn+Sn) a shift from 654 to 609 cm^{-1} occurs as can be seen in Figure 1.13, as well as a broadening of the nearest peaks [34]. The peak at 100 cm^{-1} may be a "shoulder" of the boson peak [39]. associated to a lack

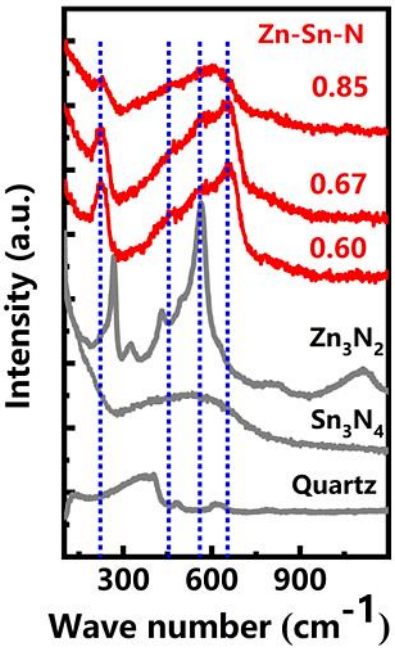

Figure 1.13: Raman spectra for different samples that possesses Zn/(Zn+Sn) equal to 0.60, 0.67 and 0.85. In addition, the Raman spectra of Zn3N2 and Sn3N4 is presented [34].

of long-range order. Furthermore, the absence of sharp peaks corresponds to a mixed crystallography phase for all the samples [31].

1.5. Optoelectronic properties

The way that $ZnSnN_2$ interact with light is of paramount importance for determining the best suitable film composition for PV applications. Experimental bandgap values are higher than predicted values because of the band-filling due to degenerate carrier density, or to changing the order of the cation sublattice [4]. There's a bond between optical and electrical properties and here are subdivided in 3 sub chapters for better understand the complexity of this intertwining.

1.5.1. Conductivity and transport

The conductivity of ZTN is expected to vary over four orders of magnitude when considering different growth temperature as seen in Figure 1.14 and cation composition considering the RF sputtering deposition technique. As the Zinc content increases, the conductivity falls from 100 S cm^{-1} to 0.1 S cm^{-1} [4], [40].

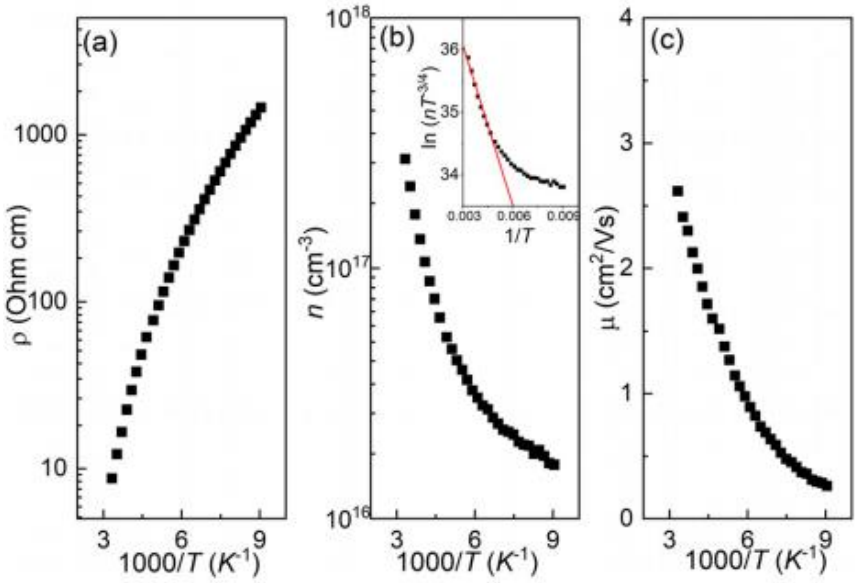

Figure 1.14: Plot of resistivity (a), carrier concentration (b) and mobility (c) of Zn/(Zn+Sn) of 0.72 and grown at room temperature [29].

At values over 0.7 Zn/(Zn+Sn) the conductivity increases, but the phase may be not stable. The trend of the growth temperature effect is clear, increasing the temperature will lead to an increase in conductivity, that is one order of magnitude if considering a shifting from room temperature to 280°C [4].

It's worth noting that the resistivity value is very sensitive to the deposition technique and parameters, it can reach values as low as 2.14 x 10^{-2} Ω cm [41]. The resistivity is found to decrease from over 100 Ω cm to 4.61 Ω cm when increasing the annealing temperature up to 350°C [22].

In literature the carrier mobility value is in between 0.37 [22] and 10 cm^2/Vs [33], although from theory it should be much higher. This behavior could be derived from to the small grain size typical of thin films [33]. Elemental composition affects the mobility, indeed, increasing the Zinc content in the film will transmute in a lowering of the carrier concentration of two order of magnitude and an increasing in mobility from 2 to 8 cm^2/Vs [4].

The growth temperature seems to increase the mobility in zinc rich samples shifting from 0.37 toward 2.07 cm^2/Vs [33], while near stoichiometric samples doesn't show a correlation between growth temperature and mobility [4]. Moreover, a post annealing treatment is proven to lower the mobility of stoichiometric and non-stoichiometric samples up to 6 hours [40].

1.5.2. Carrier density

The main problem that can hinder the using of ZTN in photovoltaics applications is the degeneracy of electrons carrier concentrations in the range of 10^{18} to 10^{21} cm^{-3} [29]. This high electron concentration in a thin film, create a region that is incapable of effectively absorbing sunlight [37].

The obstacle to overcome is to understand how the defects of the semiconductor contribute to the carrier concentration of the film [42]. A carrier concentration density of 10^{21} cm^{-3} has often been noticed in $ZnSnN_2$ literature [4]While the best suitable carrier concentration for PV applications is in the range between 10^{13} to 10^{16} cm^{-3} [43].

It is noticed that the donor defects have a lower energy formation, so they are more prone to form rather than the acceptor defects. This causes an intrinsic n-doping of the material. The donor defects are: Sn_{Zn} antistites, that is Sn substituting Zn, Nitrogen vacancy VN and Zn on the interstitial site surrounded by four N anions (Zn_i). While the acceptor defects are Zn_{Sn}, vacancy of Zn and interstitial Nitrogen [42]. Treating gas defects, Nitrogen vacancies are formed because of nitrogen is slightly prone to incorporate due to its intrinsic inertness while O_N arise due to the tendency of nitride materials to uptake oxygen [4]. However, the most favorable donor defect is Sn_{Zn} antistites due to the higher volatility of Zinc with respect to Tin that allow the desorption of Zinc [4], [42].

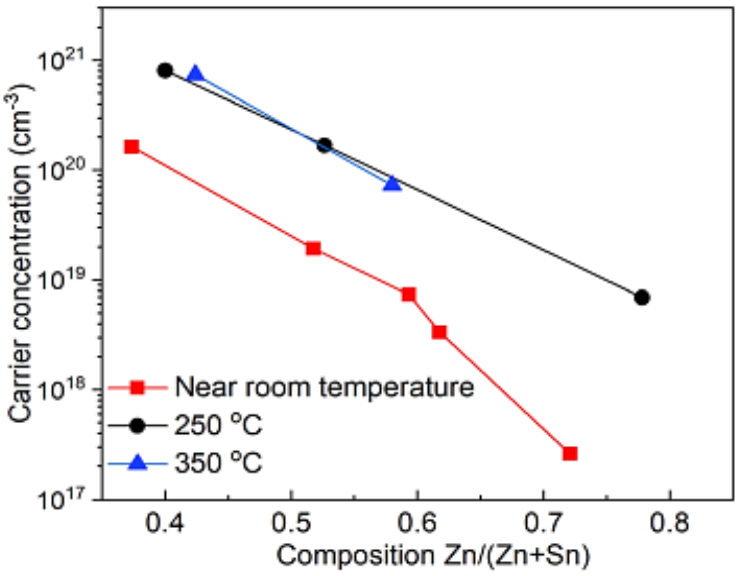

Figure 1.15: Carrier concentration of films with different Zn/(Zn+Sn) deposited at different temperatures, Room, 250 and 350°C [29].

Carrier concentration can be modified varying the ratio of Zn over Sn in the film. Increasing the amount of Zinc in the film to form an over stoichiometric zinc film, yields to a lower carrier density of 1.8×10^{18} cm^{-3}. In the range of 0.35 to 0.70 of Zn/Zn+Sn content in the film, the carrier density value span over two orders of magnitude. Also, post-annealing treatment has been proven to be a suitable way to reduce the carrier concentration in stoichiometric films ($10^{17} – 10^{18}$ cm^{-3}) [18].

Another option is to synthesize films with a high concentration of Zinc to form an over stoichiometric Zinc film that will suppress suppresses the intrinsic donor defect such as Sn_{Zn}^{2+} giving a carrier concentration of about 4 x 10^{16} cm^{-3} with a ratio of 0.68 Zn/(Zn+Sn) [17], [29]. That is because Tin has four valence electrons and when it substitutes a Zinc atom that has only two valence electrons, the two redundant electrons given by the Tin will contribute to increase the carrier density.

Moreover, adding Zinc, promotes the formation of Zn_{Sn} that act as acceptor. It is important to consider that when the ratio Zn/Zn+Sn is higher than 0.8, other phases such as Zn_3N_2 can form, giving instability to the formation of ZTN films [29]. So, the problem of degeneracy in ZTN films can be overcome by either modifying the Zn quantity in film or with a post annealing treatment [17], [18] . Another defect that contributes to increase the degenerate the carrier density is the oxygen present during the growth of the film, the oxygen remains entrapped in the structure acting as anion, substituting nitrogen atoms [17].

Low temperature growth can also modify the carrier density reducing the unintentionally donor defects such as Oxygen on Nitrogen and interstitial Hydrogen impurities that have lower formation energy than Sn_{Zn}^{2+}, so they act as shallow donor. When considering the carrier density at various growth temperature a difference of one order of magnitude is observed. As observed in Zn_3N_2 when the temperature of growth is higher than room T, the O_N^+ and H_i^+ are increasing, giving a raise in electrons concentration [29].

When increasing the annealing and growth temperature, in over-stoichiometric samples the carrier density arises accordingly to first principles calculations. Oxygen substitute Nitrogen forming the O_N defect that acts as shallow donor [22].

1.5.3. Light absorption

To have a full comprehension of this material, transmittance, and reflection values of near-stoichiometric ZTN are discussed. Since they are strictly related to the deposition parameters as well as the deposition techniques, a detailed explanation of this curves can be found in the next chapter, based on our results. In literature transmittance and

reflectance curve are hard to found since they are mainly used for obtaining the bandgap value (Figure 1.16).

ZTN features a direct bandgap [17] that is mainly affected by the cation ratio Zn/Sn and the presence of oxygen impurities [43]. As said $ZnSnN_2$ is outstanding from this point of view since it is intrinsically n-doped, so an excess of free electron is present [42].

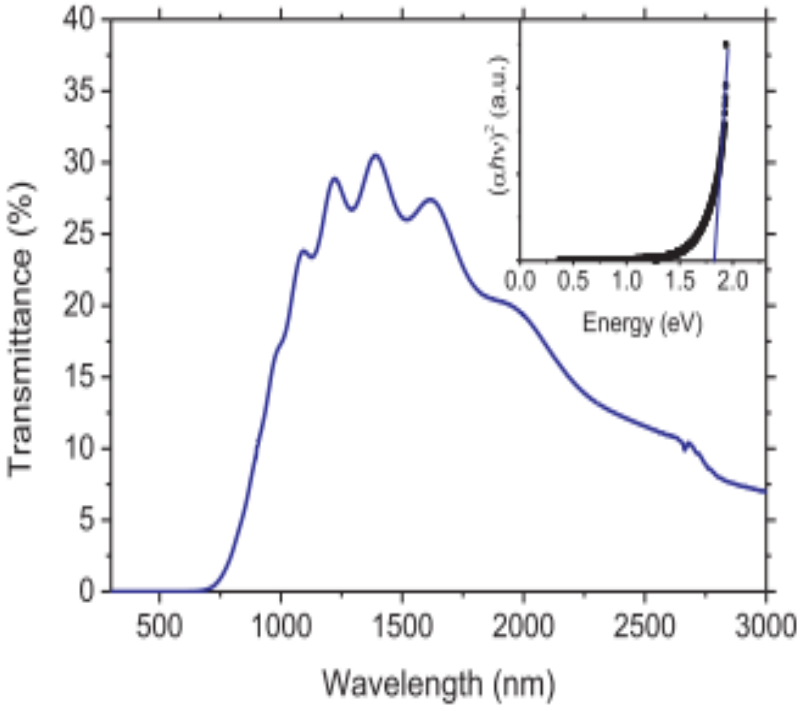

Figure 1.16: Transmittance and Tauc plot showing the bandgap value for $ZnSnN_2$ [32].

For this semiconductor, accurately determining the precise bandgap value is very challenging since calculated bandgap values range from 0.35 to 2.64 eV due to the different approximation used and the crystal structure considered. Experimental values instead range from 1.7 to 2.1 eV. This difference emerges because of the different arranging of cations that modulate the bandgap [18] With first principles calculations the ordered phase is expected to have a Eg of 2.3 eV while the disordered phase of 0.98 eV [30].The most accurate energy gap was proposed by Lahourcade et al. of Eg = 1.42 eV for an orthorhombic ZnSnN2 structure with a hybrid functional

(HSE06) [17]. As accomplished, further studies need to be done to find the exact intrinsic Eg. $ZnSnN_2$ shows configurations characterized by the disordered distribution of cations, while still adhering to the local octet rule. Computational predictions suggest that the material's bandgap remains stable in the presence of this type of charge-conserving disorder. This projection sets $ZnSnN_2$ apart from other II-IV-V2 materials, such as ZnGeN2, where long-range and local orderings tend to influence each other [44].

Fioretti et al. investigate the Burstein Moss effect (Figure 1.17) and proved that also $ZnSnN_2$ exhibits this behavior [18]. Experiments were done on quasi stoichiometric $ZnSnN_2$ obtaining a bandgap of 1.0 eV in good agreement with theory for cation disordered structures.

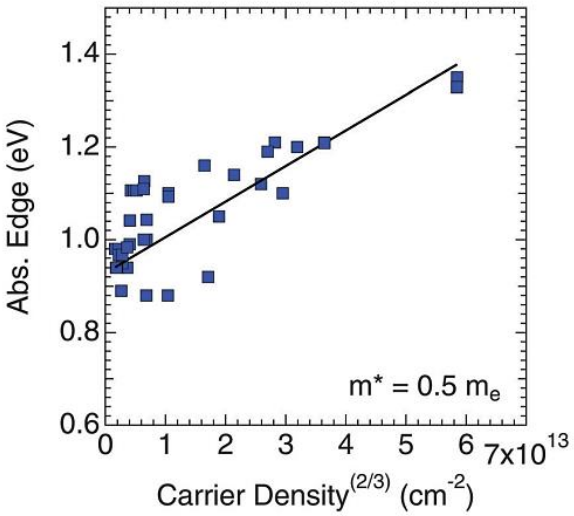

Figure 1.17: Variation of the Absorption edge with the carrier density, here the Burstein Moss effect is evident since an increasing in carrier density will transmute in an increasing of the absorption edge value [18].

Therefore, the optical absorption and Hall effect indicate a complex interaction between the Burstein-Moss shift due to conduction band filling and the continuous fundamental gap changes associated with various levels of cation disorder [35]. However, a study shows that this effect is not so predominant in $ZnSnN_2$ since the free electrons prefer to occupy the donor defect level below the conduction band rather than filling it [42]. When tuning the bandgap, it must be considered also the deposition

parameters that can affect the cation ordering as seen in Figure 1.18. Growing a film with a low amount of nitrogen flux will origin a more metal rich film thus translating in a greater cation ordering [35].

Qin et al. noticed a little variation from 1.64 to 1.70 eV by ranging the temperature from 0°C to 350°C [22]. ZTN films display a direct bandgap, hence the bandgap can be calculated as follows [9]:

$$(\alpha h\nu)^2 \propto h\nu - E_g$$

Specifically, only the direct transitions from the valence band to the Fermi level contribute to the absorption spectra [35]. Also, the effect of post annealing is unsure since in some works the bandgap shifts from 1.82 to 1.95 eV when annealed [9], while in another work the bandgap lowers when from 2.75 to 2.11 eV with a post annealing treatment [36].

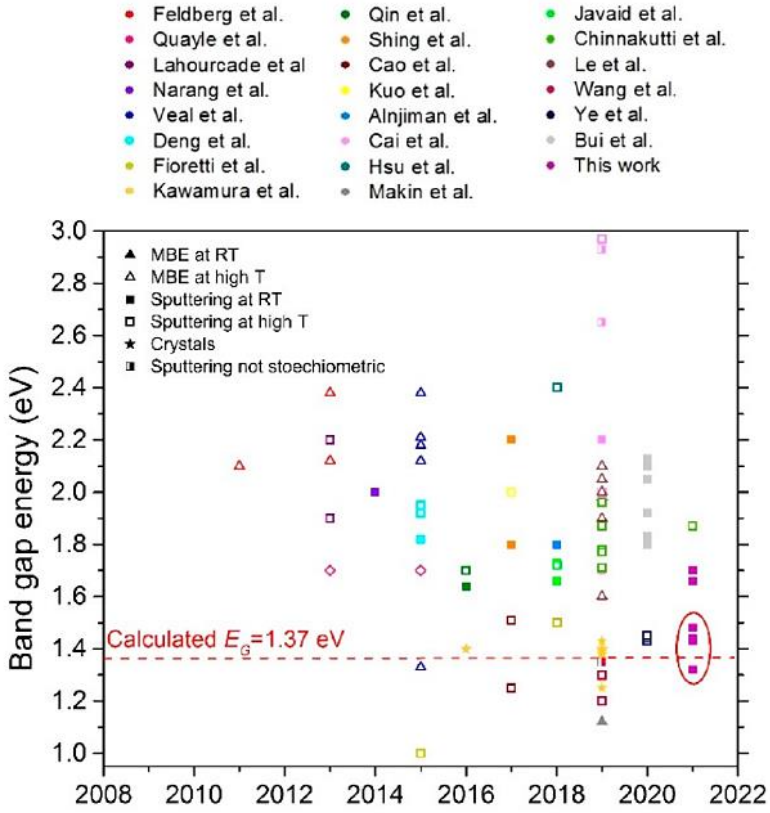

Figure 1.18: Bandgap values of ZTN of samples deposited in different deposition condition [17].

1.6. Deposition parameters

As in the previous paragraphs is stated that the material properties are strictly correlated with the deposition parameters, in this chapter the effect of the main variable is explained. In particular, the composition of the film, the role of oxygen content as well as the temperature, intended as growth temperature and annealing treatment. These parameters will be recalled in the next chapter as they were investigated in this thesis work.

1.6.1. Zinc content in the film

The main parameter that affects the cation disorder and the carrier concentration is the zinc content inside the thin film. More precisely in literature the Zinc content is considered as Zn/(Zn+Sn). The ZTN can be synthesized with Plasma-assisted vapor-liquid-solid deposition [45] RF and DC magnetron sputtering [9], [33].Some experimental studies will be here proposed to better understand the correlation between the metal target source and its related content in the ZTN film.

With sputtering process, the most used configuration is RF sputtering and radiofrequency is applied on the Zinc cathode while direct current regime is utilized for Tin cathode when two cathodes were exploited. In order to vary the film composition, different voltages (or currents) are applied to the cathodes. In a work presented by Virfeu et al. [17] a current of 0.1 and 0.25 A applied respectively on Zinc and Tin cathodes transmute in a Zn/(Zn+Sn) of 0.54 while in the work of Alnjiman [32] a fixed voltage of 250 V for Zinc and 460 V for Tin will lead a Zn/(Zn+Sn) of 0.53 in the film.

In most of works the metal target was an alloy of Zn:Sn and the difference in x:y ratio was investigated to consider the different Zn/(Zn+Sn) ratio in the film. In particular in the work proposed by Ren et al. [34] they exploited a Zn:Sn alloy with a ratio of 2:1, 3:1, 4:1 giving a value of Zn/(Zn+Sn) of 0.60, 0.67 and 0.85 respectively.

1.6.2. Role of Oxygen

Controlling the quantity of oxygen during growth phase is of paramount importance for better tailoring the semiconductor properties. Oxygen contaminations can be derived by the purity of reactive gas or raw target materials, furthermore oxygen can be adsorbed by the chamber's walls during the deposition [29]. It is claimed that a little concentration of oxygen in the film lead to lowering the carrier concentration based on a ZTN/ZnO solid solution model [12].

In the work of Fioretti et al. the role of oxygen defect introduced in the film is investigated. For this purpose, Zn rich films containing 14 % of oxygen were analyzed. An alloy model quite probable is combining stoichiometric $ZnSnN_2$ with ZnO as they share the same wurtzitic structure. To form this kind of alloy, the oxygen must be found as substitutional towards the nitrogen. Experimental results shown that oxygen promotes the formation of Zinc rich structure as well as the zinc prefer to occupy cation sites instead of forming new phases [46]. In most of works while observing XRD peaks, no evidence of oxygen content can be found, since it may be amorphous [22].

As verified by analysis done via transmission electron microscopy on films, the primary oxygen contamination arises from the oxidation of grain boundaries following exposure to air (Figure 1.19). The results achieved by STEM analyses shown that there are two types of oxygen inside the film. The first one is located in the columns and is bonded in the material. The second scenario corresponds to the presence of oxygen atoms concentrated at the boundaries of the columns, which could result from the diffusion of molecular oxygen into the film following its synthesis [32].

Fioretti et al. synthesized ZTN films using RF co-sputtering at 230°C exhibits an oxygen concentration equal to 4% [18]. A recent study of Pan et al. proposed a theory for non-diluted solid solutions and non-stoichiometric materials that was implemented to Zinc rich ZTN films containing oxygen impurities. In non-equilibrium synthesis, defect formation, off-stoichiometry condition and impurities must be considered. Substitutional oxygen impurities in the film are correlated to the formation

of Zn_{Sn} such that x = O/(O+N) ≈ 2[Zn/(Zn+Sn) - ½]. That means a slight concentration of oxygen can give a strong donor feature to the material [47].

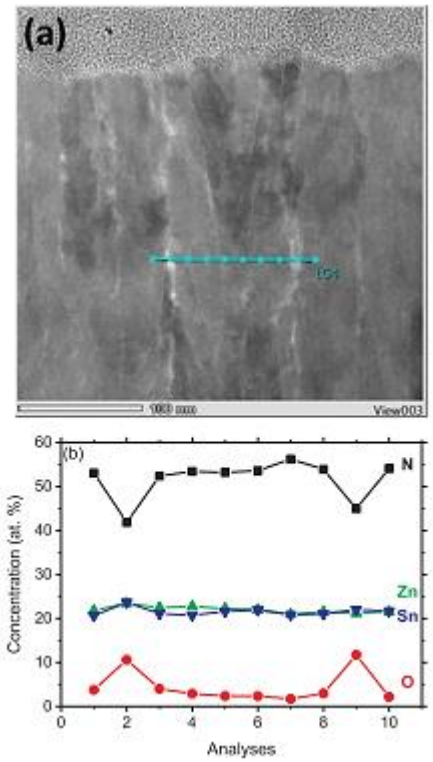

Figure 1.19: STEM image of ZTN in cross section inspection (a) and (b) EDXs compositional data. It can be noted that the content of Oxygen is higher in the boundary of the grains [32].

1.6.3. Role of temperature

In this paragraph the main role of the temperature is discussed, focusing on the effect of the temperature during the deposition step as well as the effect of the post annealing treatment.

1.6.3.1. Growth temperature

During the growth phase, the temperature has an important impact on the morphology. Similarly, to III-N semiconductors, higher temperatures lead to an increasing adatom mobility, thus resulting in a better surface morphology [27]. Higher substrate temperatures are proven to be beneficial for the crystallization of the films [36]. While if the temperature is higher than 400°C the Zinc doesn't have the time to

react properly with Tin with a subsequent poor crystallization [18], [27]. If the temperature is brought above 500°C the films show area where deposition doesn't take place. In fact, above 500°C the decomposition of the film occurs [27]. So, using an RF technique deposition, 340°C seems to be the limit temperature of deposition[18]. However, works show that also temperature of 550°C can be reached using plasma assisted deposition, obtaining orthorhombic structure [28]. NREL used RF sputtering through combinatorial experiments, investigation was done with various growth temperature from 35° to 340°C and a composition Zn/Zn+Sn ranging between 0.40 – 0.60 Zn/(Zn+Sn) and areas of stability were recognized in Figure 1.20 [12], [18].

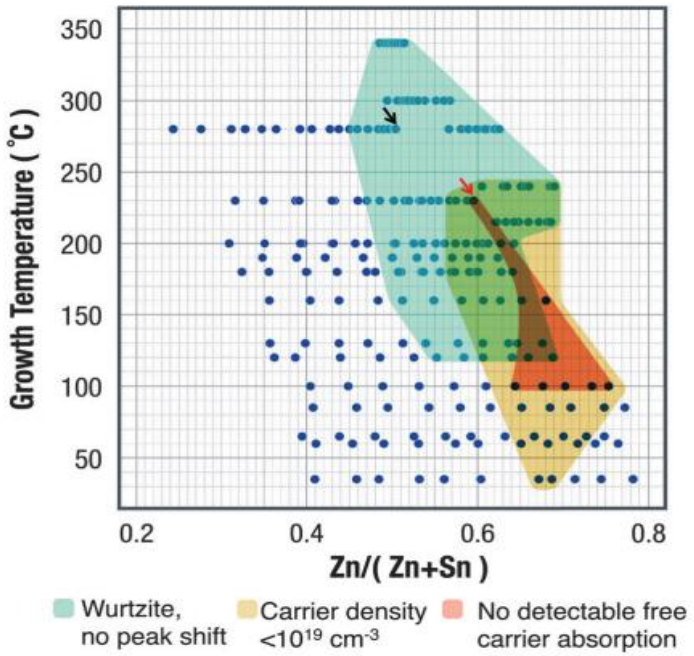

Figure 1.20: Combinatorial data taken from 6 different libraries. The teal region indicates the condition where no XRD peak shifts are observed for wurtzite structure. The yellow region underlines the samples that features a carrier density lower than 10^{19} cm^{-3} while the orange region gives the condition in which the ZTN possess a carrier concentration lower than 10^{18} cm^{-3}. The red arrow indicates the sample that shown high crystal size while the black arrow is referred to the sample with the best XRD matching with orthorhombic phase [18].

1.6.3.2. Post annealing

As stated in previous paragraphs, post annealing treatment led to beneficial consequences, improving the film properties. A temperature of 300°C is needed to induce an equiaxial grain growth. A research group try to correlate the annealing time with the carrier concentration in different stepwise composed ZTN film (Figure 1.21). Annealing was performed at 300°C for 3hr, 6hr and 14 hr. under nitrogen activated atmosphere, in the same chamber directly after the deposition. Results shows that films containing higher concentration of Zinc exhibits a significant decrease in free electron density. Another interesting outcome is that annealing time higher than 6 hours led to a higher electron's concentration.

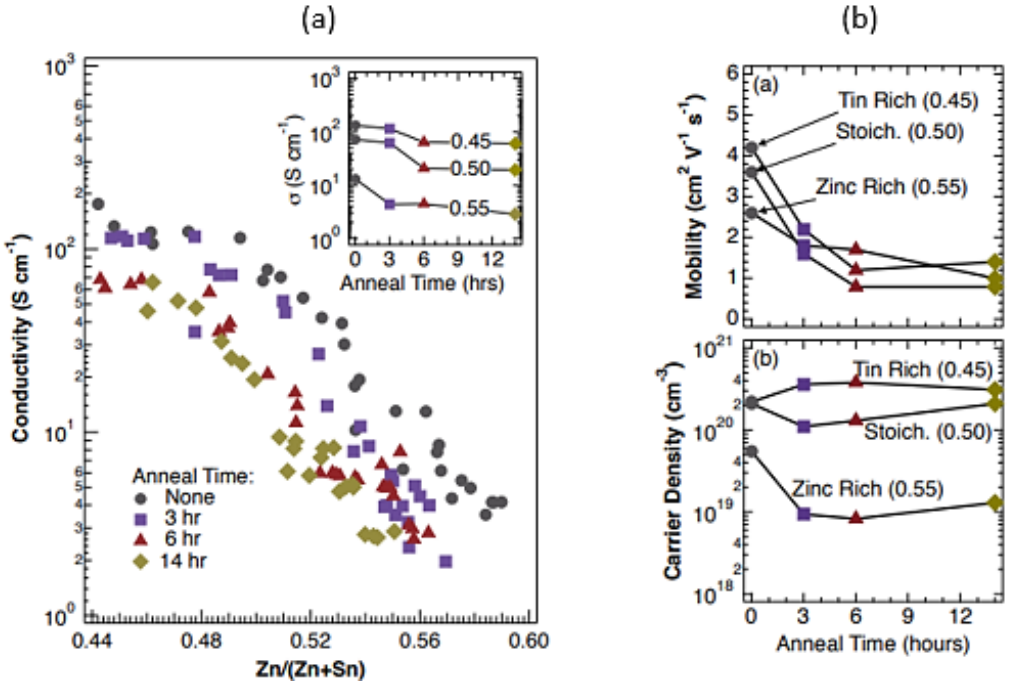

Figure 1.21: (a) Conductivity variation with different annealing time. The trend is that increasing the annealing time will decrease the conductivity value, times over 6 hours does not lead to an additional decrease. (b) Carrier density and mobility trends for three different film composition correlated to the annealing time. Mobility decrease consistently and the major effect are shown after 3 hours of annealing [40].

Moreover, higher annealing time transmute in lower mobility of the carriers. The conductivity is decreasing as increasing the annealing time and it is more emphasized for Zinc rich samples. Analyzing these results, the most proficient annealing time

seems to be 3 hours. The conductivity trend may be derived from a clustering induced by high temperature, this could be avoided by depositing ZTN on a lattice-matched substrate. The post annealing treatment at 300°C doesn't show any effect on the morphology, since all samples shows columnar structure independently on the annealing time. Some structural changes indeed can be arisen when exposing the film at temperature higher than 300°C or for more than 14 hr. to obtain uniaxial texturing to have a more cation ordered structure [40].

Post annealing treatment turns ineffective for converting an amorphous to crystalline structure when using RF sputtering [36]. While with DC magnetron sputtering a post annealing treatment is needed to develop crystallinity in amorphous films [13].

1.7. Aim of the thesis

During this Master thesis work I investigated the role of the main deposition parameters for the synthesis of a novel semiconductor ternary nitride material, the $ZnSnN_2$ also known as ZTN. This nitride semiconductor finds potential application in photovoltaics, more precisely as a component of a tandem solar cell due to the possibility of tailoring the bandgap to a desired value.

This work in intended to be a first exploration toward the deposition and characterization of this novel semiconductor. It's worth noting that nitrides are relatively underexplored in comparison to many other materials families. This material was synthesized with many different techniques such solid vapor deposition, magnetron sputtering in RF and DC regime using alloys target. As the aim is the investigation of the material's behavior with different composition, two separate metal target was utilized to control properly the zinc or tin content inside the film. This deposition technique gives uniform films and it's optimal for an industrial point of view. In the NanoLab of Politecnico di Milano, this material was never synthesized till now, so for this reason different deposition condition were considered to find the better path to follow for having a perfect material.

The power ratio of the two cathodes were controlled independently, allowing a differentiation in film composition from Zn poor to Zn rich films. Moreover, different growth temperature (from room to 380°C) and different gas pressures (from 0.5 to 1.2Pa) of nitrogen were exploited. Numerous characterizations were conducted on samples to gain a comprehensive understanding of $ZnSnN_2$ regarding the morphology as well as the electronic and optical properties.

The aim of this thesis is to correlate the deposition parameters of ZTN to its related properties, ranging from structure, electrical and optical properties.

During this master thesis I personally synthesized 31 samples through DC Magnetron sputtering, I also performed Raman, EDXs, Resistivity and Hall measurements and done SEM images both in plane and in cross section. All these deposition and

measurements were performed at Nanolab – Department of energy – Politecnico di Milano. Optical measurements were performed by Dr. Cristina Mancarella at IIT, while XRD were performed by RSE.

Further research on post annealing treatment for improve the material's properties as well as the effect of using Magnetron sputtering in High Impulse configuration for Zinc cathode are under development.

2 Experimental methods

2.1. Magnetron sputtering

The technique chosen for the synthesis of thin films was the Magnetron Sputtering that belongs to the Physical Vapour Deposition family [48] of techniques where the films are grown atom by atom directly on substrates [49]. The atoms are sputtered by two anodes forming a plasma while a reactive gas is present, the charged species and the gas atoms then react on the substrate, re-condensing and forming the thin film. In the sputtering process the energetic ions bombard the surface of the anode metal targets knocking off the atoms [50].

The process needs to be done in a vacuum chamber filled with nitrogen and the Si substrate act as cathode while the two separate metal targets act as cathodes. A constant voltage is applied with a direct current supply (as we are in DC regime) to the two cathodes and can be changed independently. The voltage applied on the cathodes lead to a formation of the glow discharge [51], so once the process it's started, the positive ions impinge the metal targets as they act as cathodes (Figure 2.1). It may be that the charged ions don't release any metal atoms so the sputter yield must be introduced.

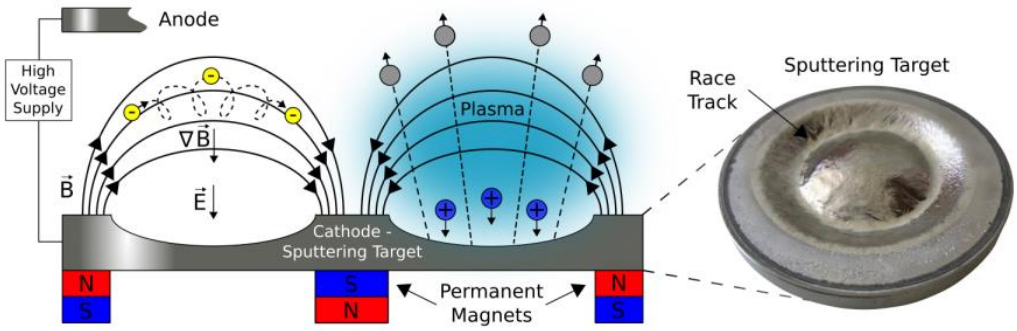

Figure 2.1: Scheme of Magnetron sputtering working principle including the configuration of the magnetic field and on the right an eroded target is shown [51].

The sputter yield gives an information about the capability of a certain atom to be sputtered and it's calculated as the fraction of the emitted atoms per unit of incident atoms.

In Direct Current Magnetron Sputtering (DCMS) the magnets are applies behind the metal targets, the magnetic field generated allows to trap the electrons in the proximity of the circular cathodes [52] (Figure 2.2). Since the cathodes are circular, one pole is the centre while the other has a circular shape and follows the edge of the target. Since the process involves the release of metal target atoms, the erosion involves mainly a

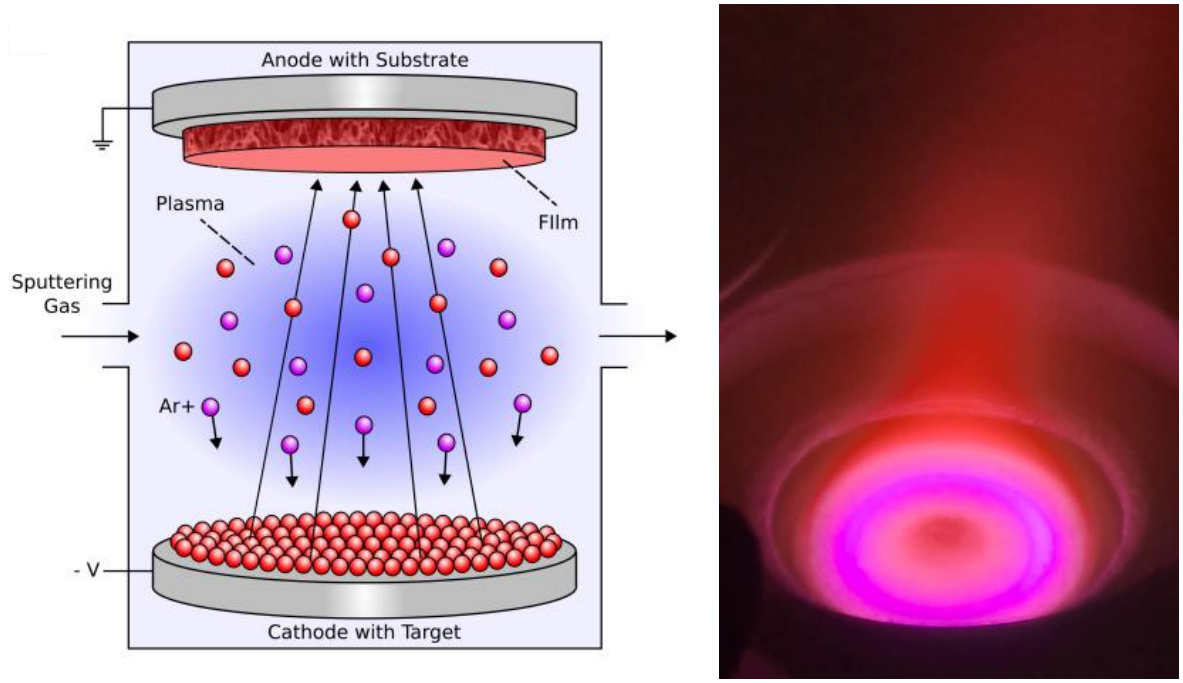

Figure 2.2: On the left is depicted a typical magnetron sputtering apparatus with a single cathode [52]. On the right is shown a cathode while sputtering metal (Image taken from NanoLab of PoliMi).

circular path leaving untouched the centre and the edges as seen in Figure 2.1. With this configuration about the 50% of the metal target remains unused. The deposition time for each sample were 15 min with a substrate rotation of 5 rpm. The deposition parameters are here listed in Table 1. (For ZTN_30 a mixture of N_2 and A_r for a total of 1Pa were exploited, for ZTN_19 the substrate Temperature falls from 350 to 300°C during the deposition).

ID	Gas	V Sn	I Sn	W Sn	V Zn	I Zn	W Zn	T	Z/Z+S
ZTN_08	117	465	0.2	102	348	0.1	30	Room	0.380
ZTN_24	112	466	0.2	101	329	0.1	41	350°C	0.424
ZTN_15	117	462	0.2	103	344	0.1	41	300°C	0.437
ZTN_20	118	460	0.2	101	347	0.1	48	250°C	0.444
ZTN_09	120	466	0.2	103	356	0.1	42	Room	0.450
ZTN_23	140	457	0.2	101	326	0.1	48	350°C	0.452
ZTN _19	115	459	0.2	101	336	0.1	48	350°C	0.457
ZTN _21	115	463	0.2	101	327	0.1	48	380°C	0.457
ZTN _30	51.5	420	0.2	101	535	0.1	49	Room	0.458
ZTN _18	115	457	0.2	102	344	0.1	45	200°C	0.469
ZTN_12	140	452	0.2	102	347	0.1	49	Room	0.471
ZTN _22	115	458	0.2	101	345	0.1	48	Room	0.481
ZTN _10	117	463	0.2	103	362	0.1	49	Room	0.500
ZTN _25	113	460	0.2	101	359	0.1	71	350°C	0.520
ZTN _01	115	466	0.1	98	387	0.1	47	Room	0.54
ZTN _11	120	461	0.2	103	373	0.1	60	Room	0.544
ZTN _07	116	472	0.2	102	428	0.2	104	300°C	0.600
ZTN _03	116	432	0.1	58	388	0.1	49	Room	0.610
ZTN _31	117	463	0.2	102	578	0.2	130	350°C	0.617
ZTN _06	114	467	0.2	103	436	0.2	105	200°C	0.630
ZTN _13	142	453	0.2	102	386	0.2	104	Room	0.669
ZTN _26	113	462	0.2	101	505	0.1	100	Room	0.683
ZTN _28	115	461	0.2	101	575	0.1	93	Room	0.685
ZTN _17	117	457	0.2	103	401	0.2	104	Room	0.689

ZTN _27	115	464	0.2	102	611	0.1	123	200°C	0.693
ZTN _02	118	465	0.2	102	434	0.2	104	Room	0.710
ZTN _14	90	477	0.1	102	420	0.2	104	Room	0.720
ZTN _29	117	461	0.2	102	585	0.1	112	100°C	0.724
ZTN _05	55.2	522	0.1	102	474	0.2	104	Room	0.730
ZTN _16	117	421	0.1	57	396	0.2	104	Room	0.773
ZTN _04	116	430	0.1	57	441	0.2	104	Room	0.780

Table 1: This table shows the deposition parameters used during the deposition, in particular the pressure of Gas value is given in sccm and V, I, W stands for Voltage, Current and Power applied to Sn or Zn cathodes. the growth temperature value is given in °C and the last column indicates the value of Zn/(Zn+Sn) in the synthesized film.

2.2. Scanning Electron Microscopy

Scanning electron microscope is employed as non-destructive technique for obtaining visual information about the microstructure, external morphology, and composition [53]. The fastness and high spatial resolution (up to 1nm) of this technique make it an optimal candidate for observing the samples at magnification up to 500.000 x.

In the thesis is utilized for seeing the difference in microstructure related to the changing of the deposition parameters such as growth temperature and gas pressure. In Figure 2.3 is shown a simplified scheme of the SEM apparatus.

The SEM [54] is composed by a vacuum chamber (5-10 mbar) where the sample holder is positioned, an electron gun and a detector to allow the measurements. An electron

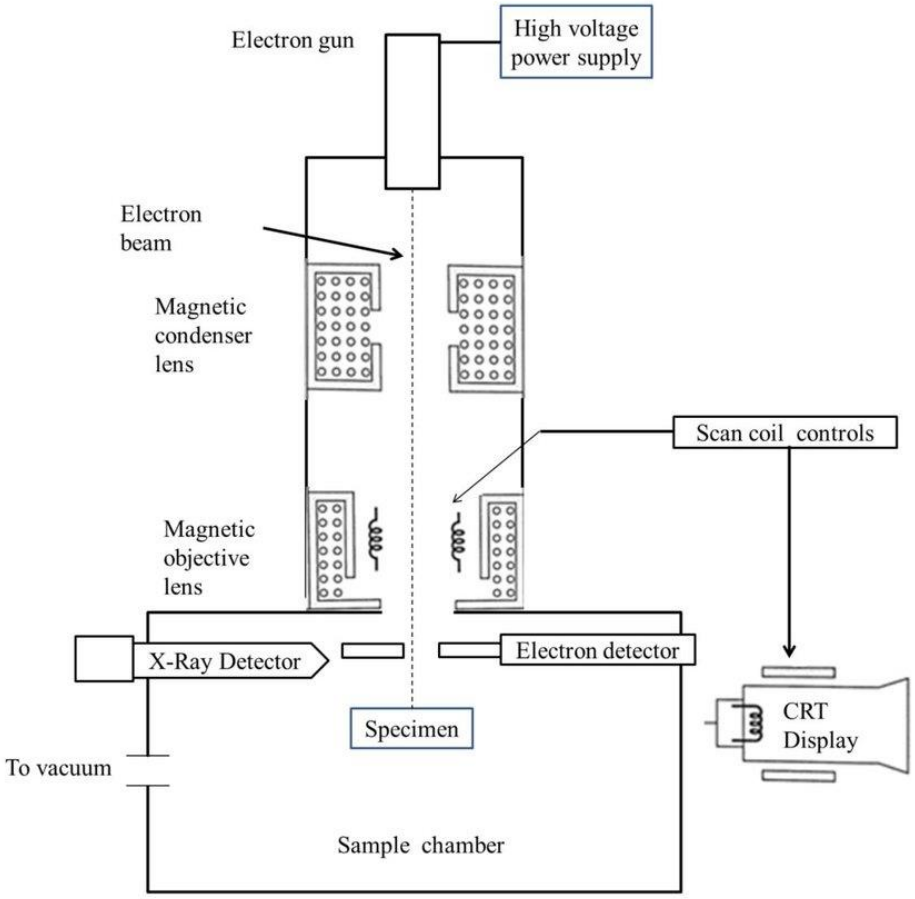

Figure 2.3: Schematical representation of SEM apparatus, the main components are presented [54].

gun emits monochromatic electrons that are accelerated and focused inside a tube due to electromagnetic lenses. The electrons impinge on the sample giving different signals that are collected by different detectors. The two main signals detected are given by Back scattered electrons (BSE) and secondary electrons (SE), the former giving compositional information while the latter giving morphological and topological information [55] [56].

The microscope used in this thesis is a Field Emission Zeiss SEM Supra 40 based on a GEMINI column. It's used also to measure the thickness of the film in cross section observations. The in plane and cross images were taken using 5,0 KeV with an aperture of 60 μm and a working distance of 5 mm. The images presented were taken using InLens signal. The height of each sample was taken in three different spots in order to have an exact thickness. Due to the magnetron sputtering deposition the thickness was homogeneous all over the sample as well as the composition.

2.2.1. EDXS

The Scanning Electron Microscope used for this thesis was equipped with a detector for Energy Dispersive X-Ray Spectroscopy (EDXS). During the measurements, an electron coming from the electron source impinge the core electrons of the atoms in the sample: the core electron could eject leaving a hole suddenly occupied by a second electron coming from an outer shell, this led to an emission of energy as an Xray, with and energy specific for each atom.

This kind of measurement was of paramount importance for this thesis in order to obtain the precise content of each element forming the film. A value of 13,0 KeV is used in order to excite properly both Tin and Zinc, also 10 and 15 KeV was taken into consideration but with 10 KeV the Zinc atoms were poorly excited while with 15 KeV too much Silica was detected because of the small thickness of the samples. All measurements were done with a detection time of around 60 seconds and the scan was repeated 3 times for each sample in different zones to obtain a precise value. A working distance of 8.5 mm and an aperture of 120 μm was used for all the measurements.

2.3. Raman spectroscopy

Raman spectroscopy (Figure 2.4) is a non-destructive technique that is employed in materials analyses [57] for giving information about crystal structure due to detection the vibrational modes related to the bonds of the elements inside the material [58].

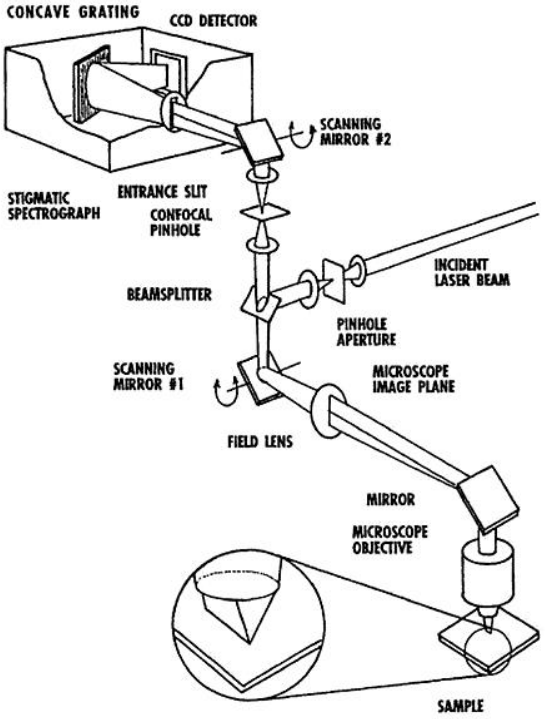

Figure 2.4: Scheme of Raman apparatus [58].

The measurement relies on the interaction between the monochromatic laser and the sample [59] [60].

The interaction is possible due to different masses and bond lengths present in the material, which gives rise to vibrational modes when oscillating around their equilibrium position. Each crystalline structure present different quantized vibrational modes that are labelled as phonons, their energy is defined as follows:

$$E = \left(n + \frac{1}{2}\right)\hbar v_{vib}$$

Where n in an integer number (≥0) associated to the vibrational levels (Figure 2.5) and $\hbar v_{vib}$ is the energy of a quantum vibrational level. When a laser beam impinges the surface of the material, the system is excited to a 'virtual' higher energy state [61]. The

excess of energy is then released by emission of a photon, and three scenarios can be observed:

1. ***Rayleigh scattering***: The system returned to its initial vibrational state. The energy is not acquired, and the scattering is considered elastic. It's the most probable path to follow for the system, with a probability of 99%.

When the system doesn't return to its initial state and the scattered light differs from the incident one, an anelastic scattering occurs and two situations can be found [61]

2. ***Stokes scattering***: The final vibrational level of the system is higher than the starting one and the frequency of emitted photon is lower than the incident one.
3. ***Anti-Stokes scattering***: The final vibrational level of the system is lower than the starting one and the emitted photon has higher energy than the initial one. This implies that this process needs an empty vibrational state at higher energy to be occupied by the final photon. As phonons follow the Bose-Einstein statistic, this process is even less probable than the stokes scattering.

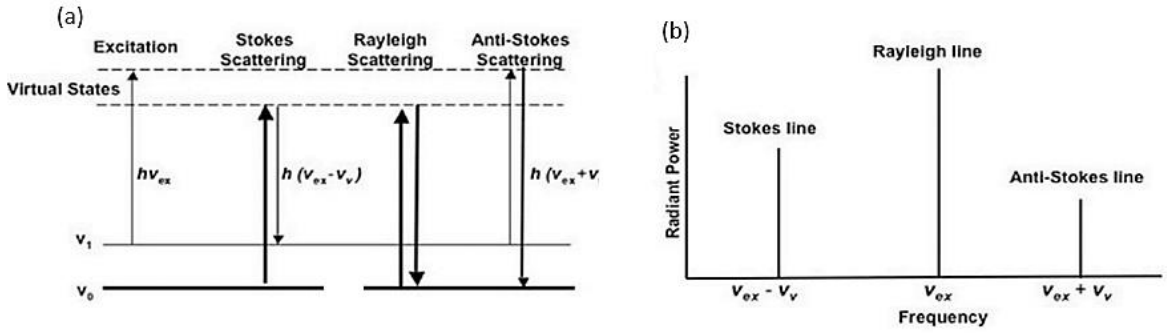

Figure 2.5: (a) Stokes, Rayleigh and Anti-stokes vibrational modes resulting from an interaction between the light source and the material, (b) Intensity of the power for the possible vibrational modes [53].

In order to observe the vibrational modes in a crystalline structure, the system must satisfy two requirements: the system has to change the polarizability during the interaction and the wavevector **q** needs to be around zero. That is, only the optical phonons at the centre of the Brillouin zone contribute to the Raman spectra due to the conservation of energy and wavevector. Raman spectra is intrinsically related to the

structure of the material since with different atoms arrangements, the active modes changes. It is worth noting that, as the disorder increase, more modes became active inside the Brillouin zone and the peaks became broader [57].

The Raman spectrometer used for this thesis work is a Renishaw InVia micro Raman spectrometer, equipped with an optical microscope (50x objective). The laser used is an argon ion laser, a monochromatic light source with wavelength λ= 514nm, with a power of 1 mW, with the real power on the sample of 0,39 mW in order to avoid any modification of the material.

In our samples the peaks are broad due to the presence of various phase and the oxygen content that will deform the exact peaks shape. Each sample was analysed three times, the scanning limits where from 100 to 3200 cm^{-1} and two times from 100 to 1500 cm^{-1}. The ranges of this scans were chosen in accordance with the presence of the ZTN related peaks found in literature. The scanning parameters varies depending on the range. Measurements in the range of 100-3200 cm^{-1} were performed with ten accumulations each one with a scanning time of 10 seconds each. While for more precise measurement (100-1500 cm^{-1}) thirty and fifty accumulations with a scanning time of 10 seconds each were utilized. In our samples, the difference in scanning accumulations from 30 to 50 doesn't affect the shape of the peaks.

In this thesis the Raman spectroscopy is used to observe a correlation between the content of the zinc inside the film and the shape of the peaks will help to determine the crystalline structure when used coupled with XRD measurement.

2.4. X-Ray diffraction

X-Ray diffraction is a non-destructive technique largely used in materials characterization since it allows to detect crystalline features of materials [56].

The working principle of the XRD can be described as follows: First, a highly energetic electrons beam is accelerated toward a metal target located in a vacuum tube, causing the excitation of ground state levels with subsequent formation of X-rays, characteristic of the material. The generated X-rays are then oriented toward the

sample and a detector collects all the information about the detected peaks and the angle of measurement. Only the X-rays that follows this relationship can be detected by the instrument [62].

$$n\lambda = 2d\ sin\theta$$

Where n is an integer, λ is the wavelength of the X-ray, d is the interplanar distance peculiar from each crystalline structure and θ is the diffraction angle in degree (Figure 2.6).

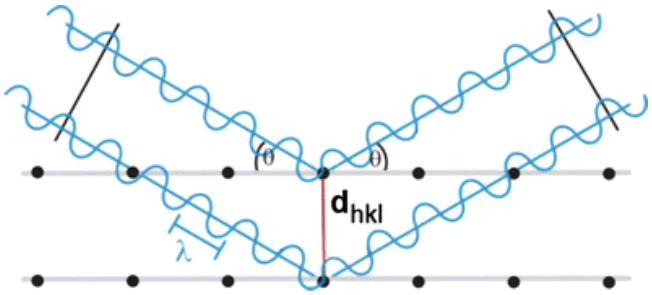

Figure 2.6: Representation of the Bragg law [62].

XRD measurements (Figure 2.7) were done to compare our spectra with literature, for knowing the crystalline structure that is very sensitive to the deposition condition, although peaks values are slightly different in literature, a deep analysis is done in the next chapter. XRD wasn't taken on each sample since these measurements were done by R.S.E. Surely a further investigation on crystalline structure need to be done on each sample.

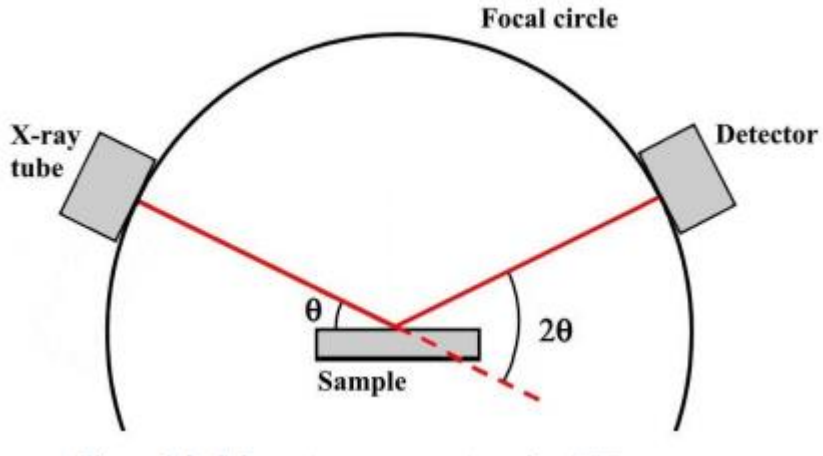

Figure 2.7: Schematic representation of an XRD apparatus.

2.5. Van der Pauw method

Electrical properties of thin films such as the resistivity ϱ and Hall coefficients (mobility μ and carrier density n) are usually derived from the Van der Paw four-probe method. To apply this method some condition must be satisfied:

- The thickness of the sample must be uniform, and the shape must be flat (i.e. square).
- The film must be continuous and without scratches or isolated holes.
- The material should be isotropic and homogeneous.
- The pins must be placed in the corner or edges of the sample.

Four metals pins are placed on the sample respecting the previous precautions. For these measurements an electrical current is applied between two probes while the other two probes measure the voltage, different configuration are possible by changing the flow of the current in different probes.

If this is repeated for all possible configurations (two probes implied in the current flow and the other two for reading the voltage), eight resistivity values can be obtained:

$$R_{21,34} = R_{12,43}$$
$$R_{32,41} = R_{23,14}$$
$$R_{43,12} = R_{34,21}$$
$$R_{14,23} = R_{41,32}$$
$$R_{21,34} + R_{12,43} = R_{43,12} + R_{34,21}$$
$$R_{32,41} + R_{23,14} = R_{14,23} + R_{41,32}$$

In this thesis is used to evaluate the relationship between disorder of the film and electrical properties, since from theory the variation of Zinc content induces a net change in electrical parameters which are strictly related to the bandgap of the material due to the Burstein Moss shift. Electrical measurements [63] were performed on samples deposited on square glass substrate of 1x1 cm. To obtain the resistivity ρ, the sheet resistance R_S has to be calculated though eq. xx where R_A and R_B are the average resistance of each sample sides.

$$e^{-\pi\frac{R_a}{R_S}} + e^{-\pi\frac{R_b}{R_S}} = 1$$

Therefore, the resistivity can be calculated as follows:

$$\rho = R_S \cdot d$$

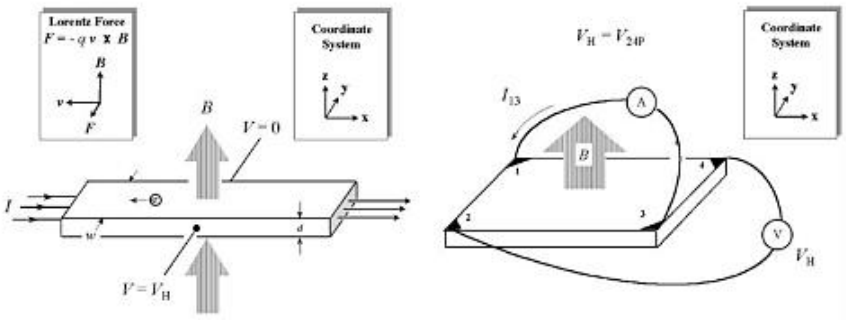

Figure 2.8: Scheme of Hall effect on the left, on the right the Hall effect measurements configuration is depicted [63].

After calculating the resistivity, maintaining the same configuration the Hall measurements are performed. What can be acquired is the carrier type and concentration a well as the mobility μ. A magnet is placed orthogonally on the sample plane generating a magnetic field B of 0,57 T. For these measurements the current is applied on the diagonal opposite probes while the other two measures the voltage. The possible configurations are two and became four with an inversion of the current. The magnet is then reversed, and the possible configuration are doubled, hence eight V_H values can be found:

$$V_H = \frac{IB}{qdn}$$

In the eq x, q indicates the charge of the carriers, d the film thickness and n the charge carrier density. Having the value of V_H, the mobility μ and the carrier density n can be calculated reversing the equation:

$$n = \frac{IB}{qdV_H}$$

$$\mu = \frac{1}{qn\rho} = \frac{dV_H}{IB\rho}$$

With Hall measurement also the type of carriers is obtained, since if the Hall voltage is positive the material has *p-type* carriers otherwise *n-type* carriers [64].

To establish the error of each set of measure a parameter, called Figure of Merit (FoM) is introduced and is calculated as follows:

$$FoM = \frac{zero\_check}{V_H}$$

Where zero_check is the potential calculated without any applied magnetic field and data are taken into consideration when the FoM < 1.

2.6. UV-Vis-NIR Spectrophotometry

The spectrophotometer is used to do UV-Vis measurements that gives information about optical properties of the material. Zinc Tin Nitride films have a potential in photovoltaic applications hence the absorption of light need to be investigated and this measurement allows to obtain Transmittance and Reflectance curves that are needed to found Absorption curves. When the incident light hits the sample, can be absorbed, reflected, transmitted, or diffused by bulk or defects present in the film. The sum of all these contributions in percentage is equal to the unity.

$$A + R + T + S = 1$$

The instrument used for this thesis is a spectrophotometer with an integrated sphere (Figure 2.9) [65], the inner side of the sphere is made of *Spectralon*, a fluoropolymer for which the diffuse reflectance is about 100%. Inside the spectrophotometer there's a monochromator that select a precise wavelength for the laser beam that will hit the sample. A detector is present to calculate the ratio of incident and transmitted or reflected radiation. Three different measurements were employed to determine three different parameters.

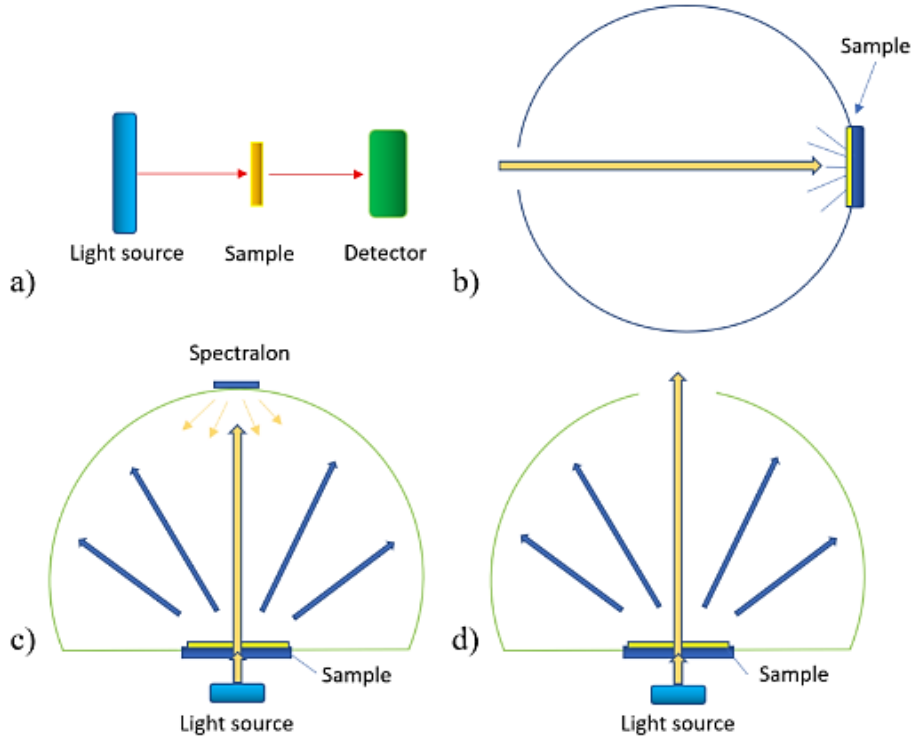

Figure 2.9: Setup for optical measurements: (a) acquisition method using to calculate the transmittance, (b) configuration used to calculate the reflectance (c) configuration used for calculating the total transmittance and diffused transmittance (d) [65].

With these three different measurements that differ only for the position of the sample and for the opening in the other side of the sphere, the absorbance A and Haze Factor can be calculated.

$$HF = \frac{S}{T}$$

All the measurements were done on glass substrates and so a normalization of the data is needed and was done as follows:

$$T_{Film} = \frac{T_{Tot}}{T_{Glass}}$$

$$R_{Film} = R_{Tot} - (R_{Glass} T_{Film}^2)$$

The measurements were performed by Dr. Cristina Mancarella at the Centre for Nanoscience and Technology (CNST) of the Italian Institute of Technology (IIT) in Milan, using a Lambda 1050 UV/vis/NIR system with a Perkin Elmer 150 nm integrating sphere. Transmittance and reflectance measurements were performed in the range 250-2500 nm, with a data interval of 2 nm.

3 Results and discussion

3.1. Thin film deposition

The deposition of thin Films of $ZnSnN_2$ was done via magnetron sputtering through direct current configuration. A total of 31 samples was done during the master thesis and four deposition sets were necessary to explore the impact of the different parameters as growth temperature, power ratio applied at the Zn and Sn cathodes, deposition pressure, and type of gas. This deposition configuration based on two separate DC cathodes is poorly studied in ZTN synthesis and it's very effective in controlling finely the environment. In this work we obtained stoichiometric and non-stoichiometric films, with a composition of Zn/(Zn+Sn) ranging from 0,38 to 0,78 by changing independently the power of each cathode. The voltage values applied to the cathodes were taken from theoretical considerations based on the bonding energy of Zn and Sn elements [31]. To obtain the nitride, most of research work [17], [18], [31], [37], [41] used a mixture of N_2 and Argon but in this work was chosen to use only nitrogen as gas, and 1 Pascal seem suitable for the achievement of $ZnSnN_2$ films with tunable properties and composition. Zn shows a binding energy of a half with respect to Sn when sputtered with nitrogen gas at 1 Pa [66], indeed for obtaining stoichiometric films the power of the Tin cathode was twice the power of Zinc cathode: 49 W for Zn and 103 W for Sn. Experimental results show a linear relation between the power ratio Zn/Sn applied on cathodes and the ratio of Zn over Zn+Sn in the films.

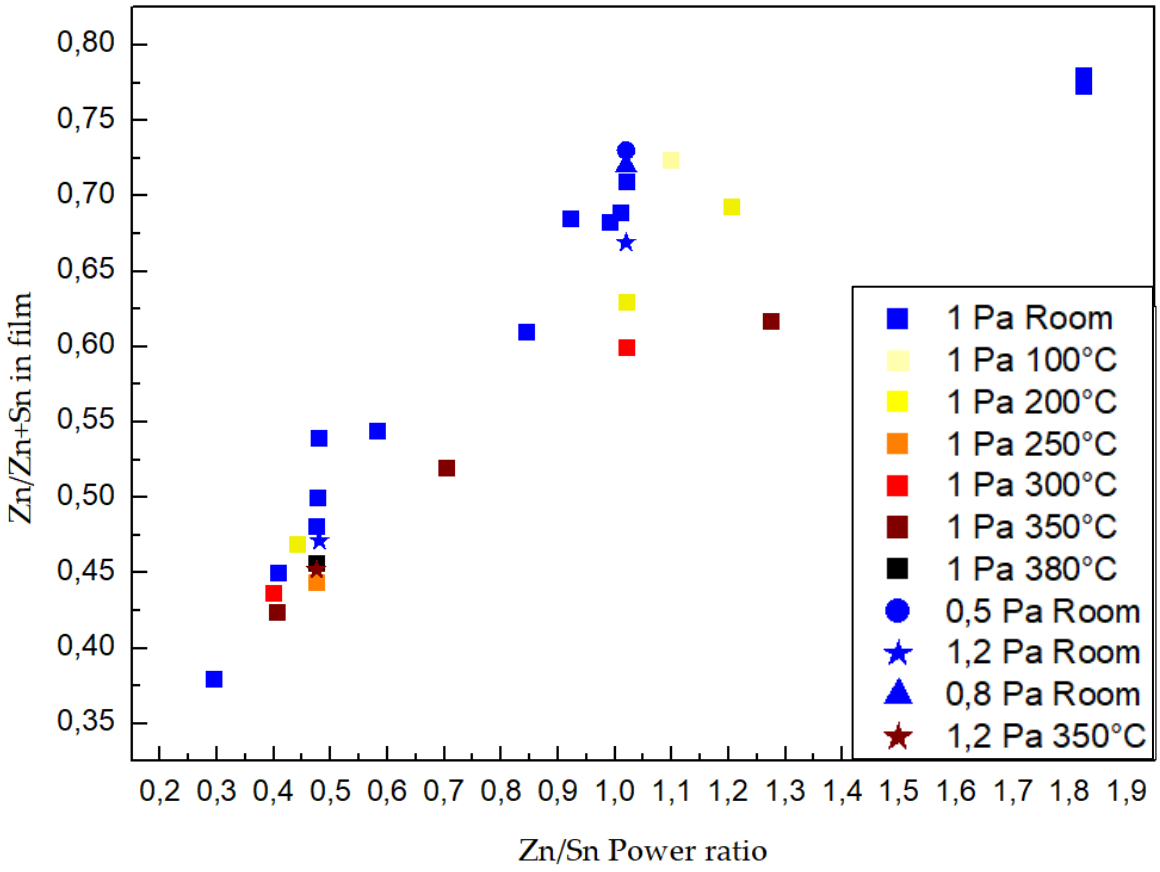

Figure 3.1: Zn/(Zn+Sn) content in the film deriving from different Zn/Sn power ratio applied on the cathode.

Some samples tend to oxidize within two days after the deposition, and the oxidation continues during the following days changing the colour becoming yellow, green, and violet as seen in Figure 3.2. From what we can observe due to the colour changing, the oxidation process is very fast in the first hours while continue in the next days.

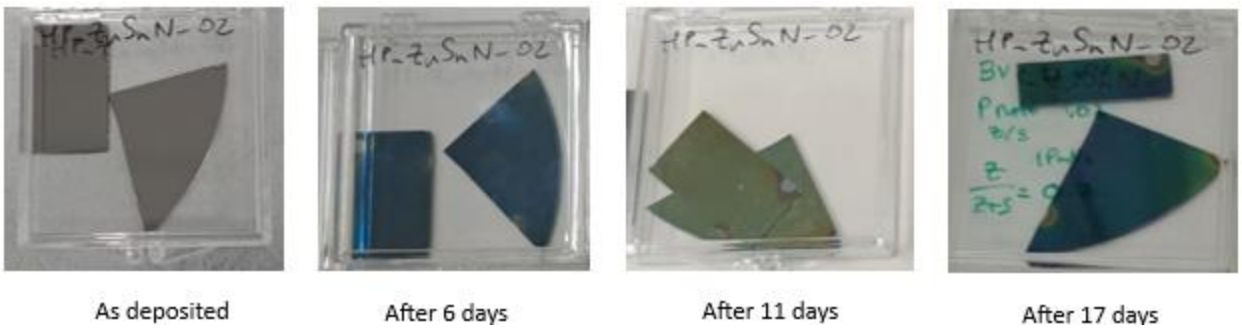

Figure 3.2: Evolution of color changing in the sample with Zn/(Zn+Sn) of 0.71 due to the oxidation.

Surely for further development, this process must be monitored right after the deposition to the complete oxidation. Also, a quantification of the elements present in the oxide during the evolution of the process must be carried out. This change in colour can be attributed to the formation of an oxide that modify the way it interacts with light acting as a dielectric.

All the samples obtained shows the presence of oxygen and this affect the films properties, having precise control over the oxygen concentration within the film is crucial when customizing the material for specific applications [67]. The oxygen content in each sample was quantified through EDXs analyses.

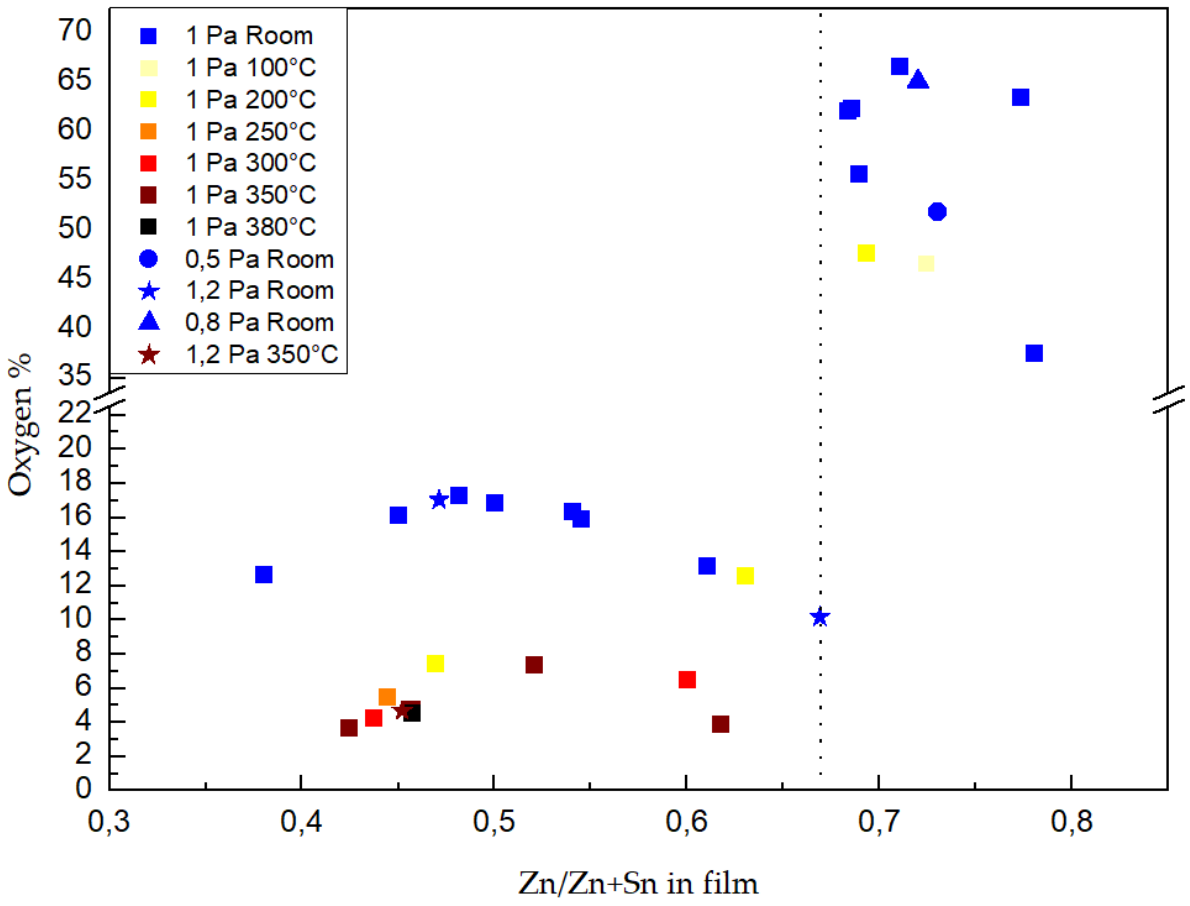

Figure 3.3: Atomic oxygen content inside the film, the dashed line indicates when the oxygen content in the film increases abruptly.

As we can deduct from the Figure 3.3, the uncontrolled oxidation with subsequent formation of oxide layer happens only in over stoichiometric samples. The plotted graph shows value of oxygen in stabilized samples, so when they are already oxidized. Considering all the samples deposited, is evident that the ZTN films that possesses over 0,67 Zn/(Zn+Sn) ratio shows oxygen atomic content over 35% inside the film.

This suggest that over stoichiometric samples may underwent a different phase transformation, and the excess of Zinc became interstitial, reacting with oxygen and forming a compound increasing its volume (indeed the oxidized film shows a very thick layer of oxide above the film) [46]. It's important to remind that this oxygen comes from the reaction of the ZTN with the exposition in ambient air while in the heated substrate specimen and films with Zn/(Zn+Sn) lower than 0.67, the oxygen contamination [19] is given by the residual oxygen inside the vacuum chamber, and it was reduced at its minimum by reaching a pressure of $3*10^{-6}$ mbar during the deposition.

As this material oxidize firmly [67], during the last deposition set five samples were put in a vacuum bell jar for making comparison. All the samples as deposited show value of oxygen in the range of 4-17% (atomic) indicating that all the excess of oxygen come from the atmosphere [32] due to the ambient exposure of Zinc rich samples.

The most interesting result, as visible in graph Figure 3.3, is that the samples synthesized at room temperature show oxygen content in the range of 10%-17%, while at higher temperatures the oxygen content fall in the range of 3,7-7,5% in accordance with literature [22], [32]

A peculiar parabolic trend can be seen both in deposited film growth at room and high temperature. The maximum of this parabola is in the vicinity of 0,5 Zn/(Zn+Sn) the film has embedded the maximum concentration of oxygen and at higher percentages of oxygen it decreases as well as the percentage of nitrogen suggesting a more metal rich samples.

It should be noted that the nitrogen content, that when the Zn/(Zn+Sn) is higher than 0,67 the nitrogen content abruptly decreases, and it can be observed in Figure 3.4. This is because in over-stoichiometric samples, an oxidation process began, and the nitrogen it is not incorporated in the matrix [36]. The effect of high temperature at deposition is beneficial for having a correct intake of nitrogen inside the matrix.

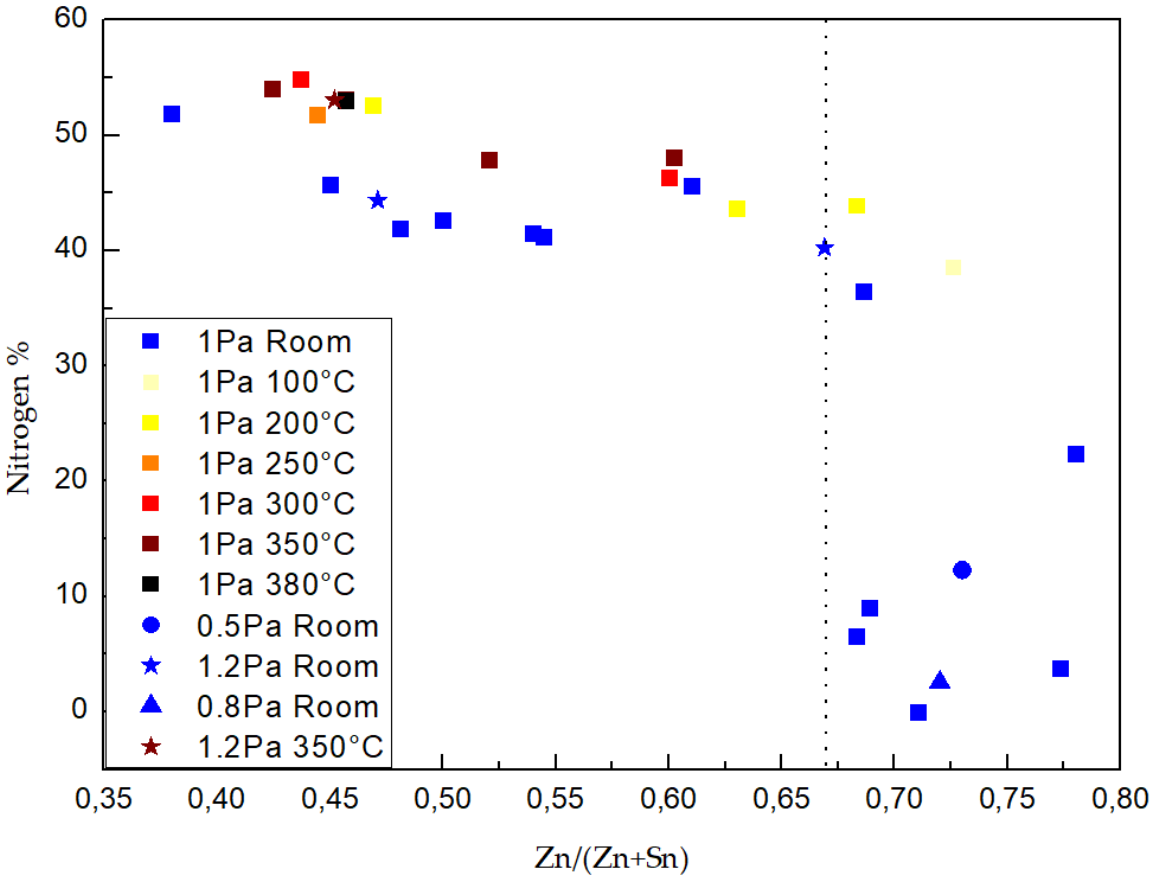

Figure 3.4: Nitrogen atomic content in the film, the dashed line indicates a range in which the Nitrogen content decrease abruptly. Values of nitrogen in the proximity of 40% for Zn-rich samples are exhibited for samples put in vacuum bell jar.

To understand better the composition of all the samples, a graph considering only the Zinc, Tin and Nitrogen is shown, in Figure 3.5 only the samples that present an atomic oxygen concentration lower than 17% are considered. Note that all the samples near the red circle are expected to arrange as $ZnSnN_2$ with a correct stoichiometry having atomic proportion near $Zn_{0.25}Sn_{0.25}N_{0.5}$.

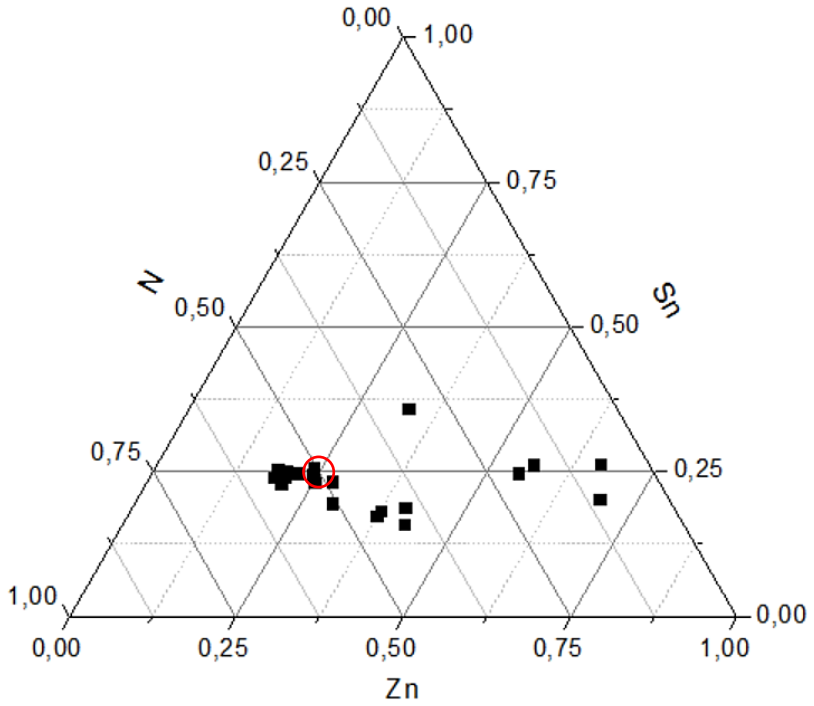

Figure 3.5: Triangular diagram that shows the composition for the deposited samples. The oxygen content is considered as an impurity, hence is not here underlined.

In the is clearly seen Figure 3.6 that the nitrogen content in the film decrease linearly from 54,9% to 0% as the atomic oxygen content increase from 3,7% to 66,8%.

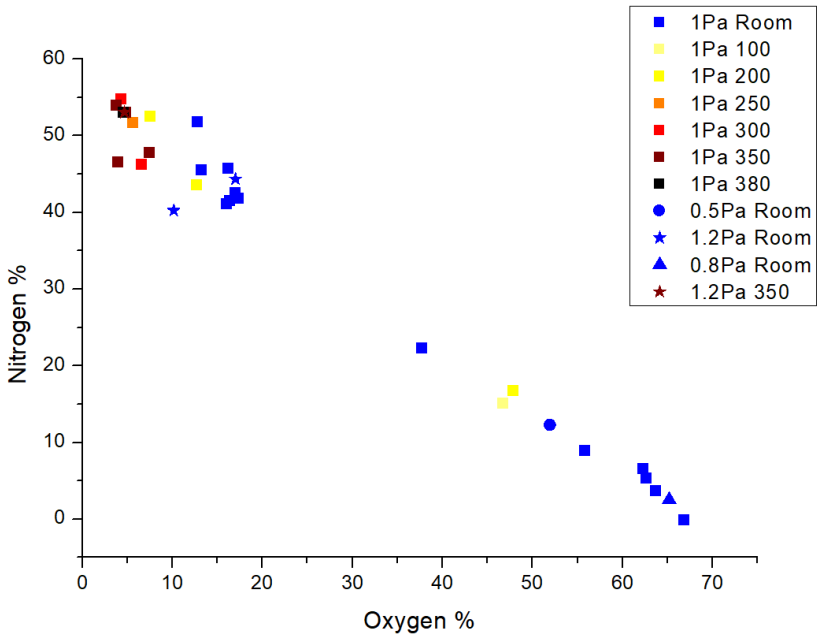

Figure 3.6: Oxygen vs Nitrogen content in the film, it underlines the mutual exclusivity of oxygen toward nitrogen.

This means that the nitrogen presents inside the as deposited film tend to leave the sample favouring the oxygen uptake. A linear trend can be observed, and the stable sample are present in the left part of the graph.

The thickness of the deposited samples is shown in Figure 3.7, it is achieved after 15 min of deposition. When the film is deposited on a non-heated substrate the thickness is in the range of 350 ±40 nm while with hated substrate is in the range of 250 ±25 nm. The measurements are affected by an uncertainty of ±10 nm since the magnetron sputtering allows a homogenous deposition. The heated substrate led to a decrease in thickness, this could be since as the grain coalescence closing the voids present in the columnar structure. For films grown at room temperature, when increasing the Zn/Sn power, also the thickness increases linearly. Further investigations are needed on the density of the films.

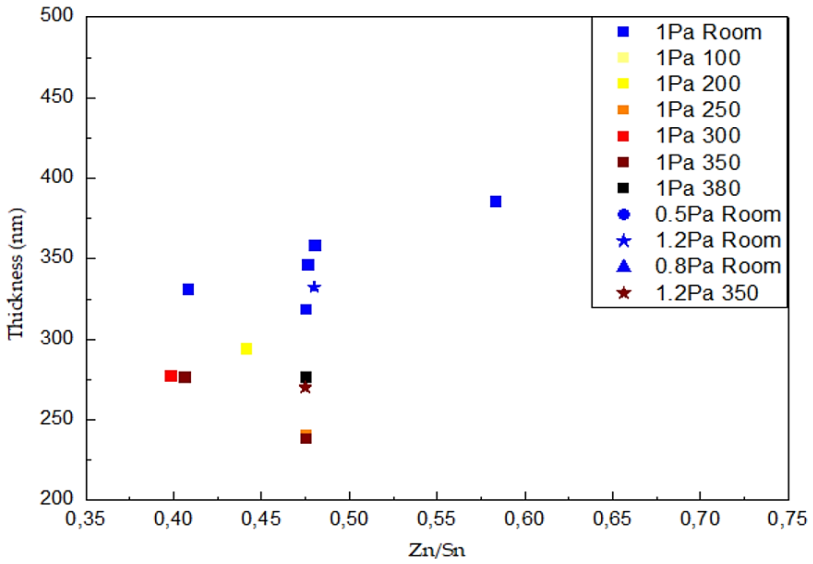

Figure 3.7: Thickness of non-oxidized film as function of Zn/Sn cathodes power ratio.

3.1.1. Growth temperature and gas pressure

Starting from this initial condition, the effect of growth temperature and gas pressure on the deposition were investigated. The substrate temperature was increased from room temperature to 380°C that's the maximum that our instrument holds while the nitrogen pressure was modified from 0,5 Pa to 1,2 Pa. In the Figure 3.1 is shown the Zn/(Zn+Sn) in the film while varying the deposition condition.

Two sets of measurements, one keeping the power ratio equal to 0,475 and the other to 1,02 were investigated. At 0.475 Zn/Sn power ratio, the ratio of Zn/(Zn+Sn) was in the range of 0.50 ±0.04 when deposited at Room temperature and with 1-1,2 Pa of nitrogen and for films deposited at higher temperatures the ratio of Zn/(Zn+Sn) in the range of 0.455 ±0.02. When considering a Zn/Sn power ratio of 1.02, the Zn/(Zn+Sn) value is of 0.70 ±0.03 for films grown at Room temperature and of 0.615 ±0.15 for heated substrate samples. The increase in the gas pressure gives a slight decrease in Zn/(Zn+Sn) nut is negligible with respect to the effect of the growing temperature.

This slight decrease in Zn/(Zn+Sn) in the film while increasing the growth temperature can be attributed to a thermally activated reemission of excess Zn particles during growth [68], [69]. Moreover, the deposition rate of the zinc is expected to decrease when increasing the substrate temperature and this is in accordance with what found during these depositions [68]. Another effect needs to be considered as the substrate is placed near the metal targets, a possible increase of the target's temperature may happen due to radiation [68].

The influence of the substrate temperature is difficult to explain since as the cathode is near the substrate, the substrate temperature may influence the plasma properties and so the final characteristics.

Considering the pressure effect, according to literature, pressure under 1 Pa may be detrimental for the film's stability and further ZTN synthesis will move toward pressure higher than 1,2 Pa. A possible explanation for the pressure trend is that the gas pressure is strictly correlated with the metal content in the film and since the zinc is less heavy than the Tin, it will suffer more the nitrogen pressure hence, lower the background pressure, the less the material is sputtered toward the substrate.

Cross section analyses done using the SEM allows to see the growth of this oxide patina during the time. First, many samples show a thickness in the range of 340 ± 100 nm depending on the deposition conditions. Moreover, the growth temperature and pressure influence hardly the stability of the films and this will be discussed more in detail in the next chapter.

3.2. Morphology

3.2.1. In plane images

SEM scans were performed to see the microstructure of the ZTN (Figure 3.8). For SEM analyses a magnification of 300.000 X is performed to clearly see the microstructure. In this chapter all the images present a white box with the name of the sample, the Zn/(Zn+Sn) the deposition condition and the oxygen content.

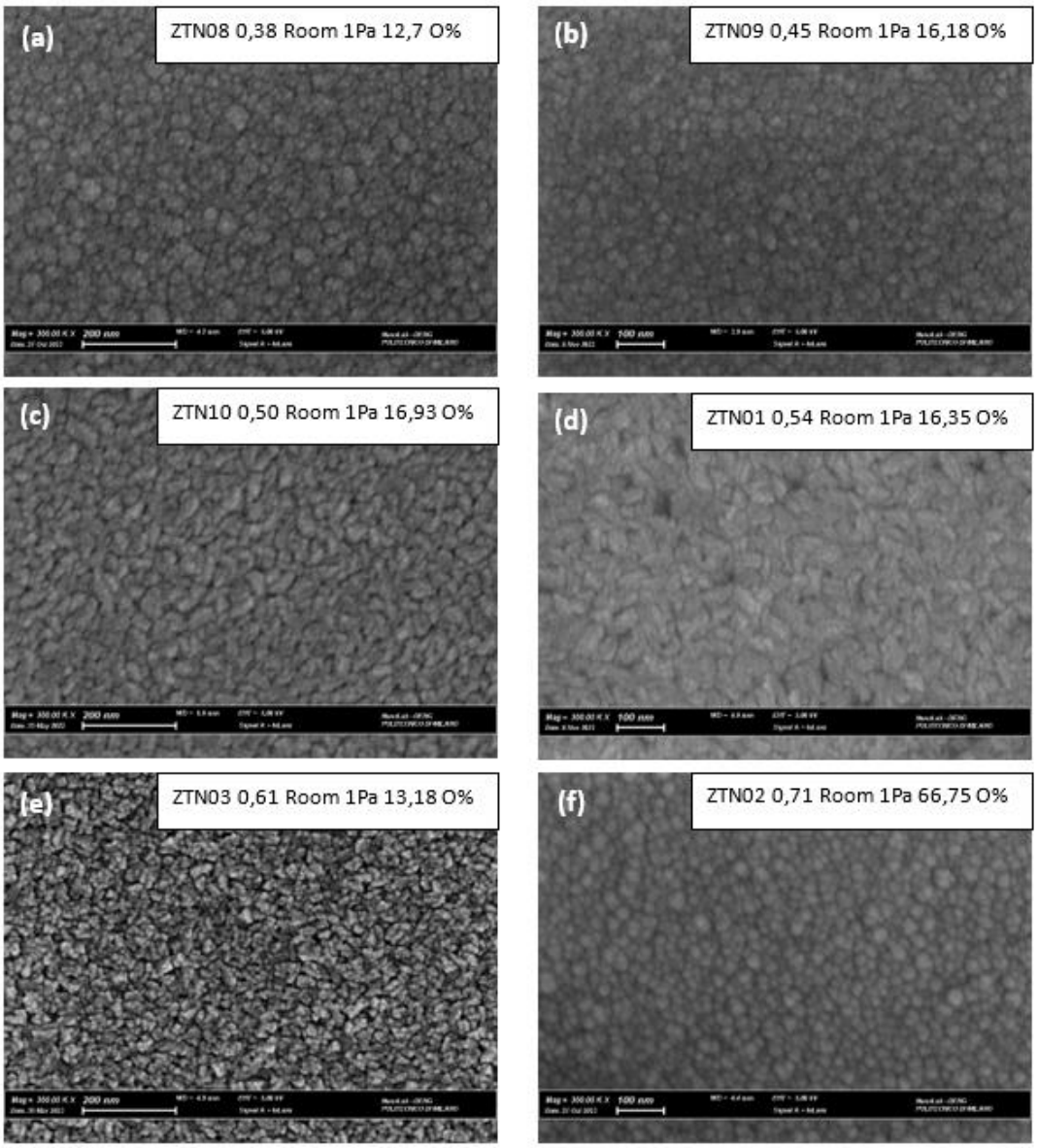

Figure 3.8: SEM images in planes showing samples with different Zn/(Zn+Sn), magnification of 300.000X.

All the samples that exhibit an oxygen content lower than 18% present a quasi-stoichiometric content of nitrogen (Figure 3.4).

First, an inspection on the samples grown at room temperature and nitrogen gas pressure of 1Pa need to be investigated. Later, a comparison with different deposition parameters can be achieved. A peculiar trend can be seen due to these images, when the film is under-stoichiometric in zinc, a small agglomeration of grains can be observed, as the zinc content inside the film increase up to 0,54 Zn/(Zn+Sn), the grains assume an irregular shape [34] and are distributed homogeneously and comparable to what found in literature [9], [17].

Increasing the Zn content in over-stoichiometric samples, the grains became smaller in size and tend to separate. It's interesting that in the samples (a,b,c,d) in Figure 3.8 the small grains are covered with smaller circular grains, this could be derived from a little oxidation on the sample.

Instead, when the film oxidizes (f) in Figure 3.8 only a compact and circular pattern deriving from oxide patina is observed [34]. When turning on the effect of temperature on the substrate, a major modification on substrate's surface appears (Figure 3.9).

Seeing the effect of temperature (Figure 3.9) on the morphology of the ZTN, the sample grown at 300°C with a Zn/(Zn+Sn) equal to 0.6 present the best compact crystal, that means the temperature helped the growth of a more crystalline structure [33], [70]. Even if all these four samples were deposited on a heated substrate, the morphology changes due to a slight difference in Zn concentration. When the film is in an under-stoichiometric condition, the grains are small and difficult to identify giving this low defined image. When the film has an excess of zinc, the grains tend to separate and there's a similarity between the sample 31 and 3 in which the shape of the grains remains the same while increasing the size.

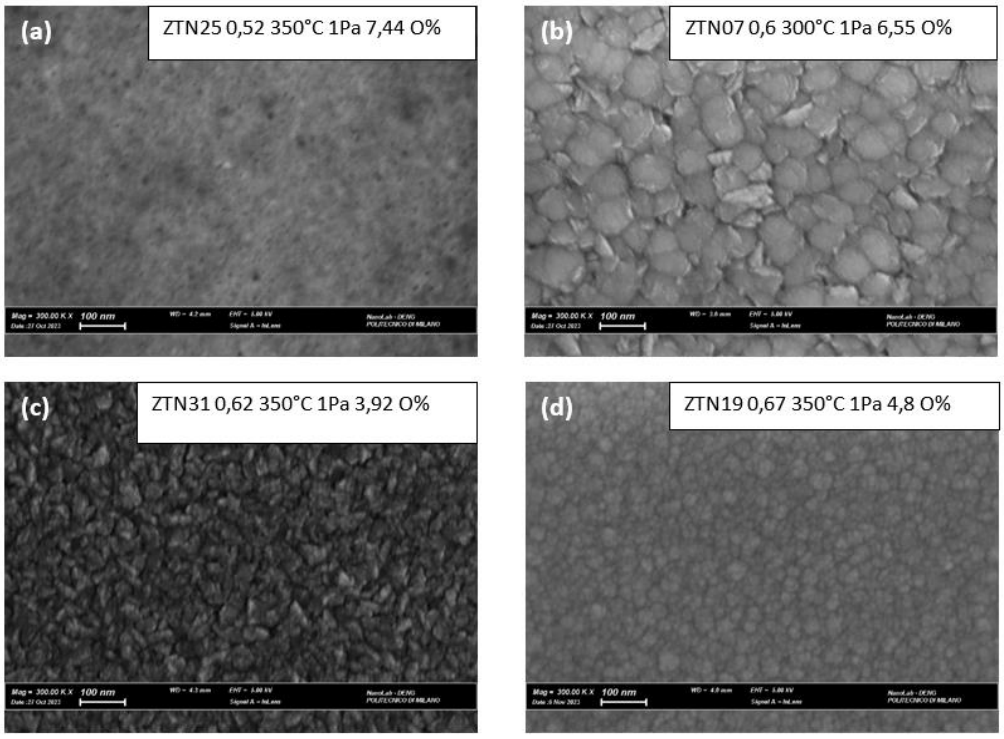

Figure 3.9: SEM images of in plane samples, from (a) to (d) is shoes the effect of growth temperature on different Zn/(Zn+Sn) of samples grown with 1Pa of Nitrogen, 300.000x magnification.

The effect of nitrogen gas pressure during the deposition (Figure 3.10) doesn't seem to affect the morphology of the film indeed the Zn content inside the film has a preponderant role in the morphology of the samples.

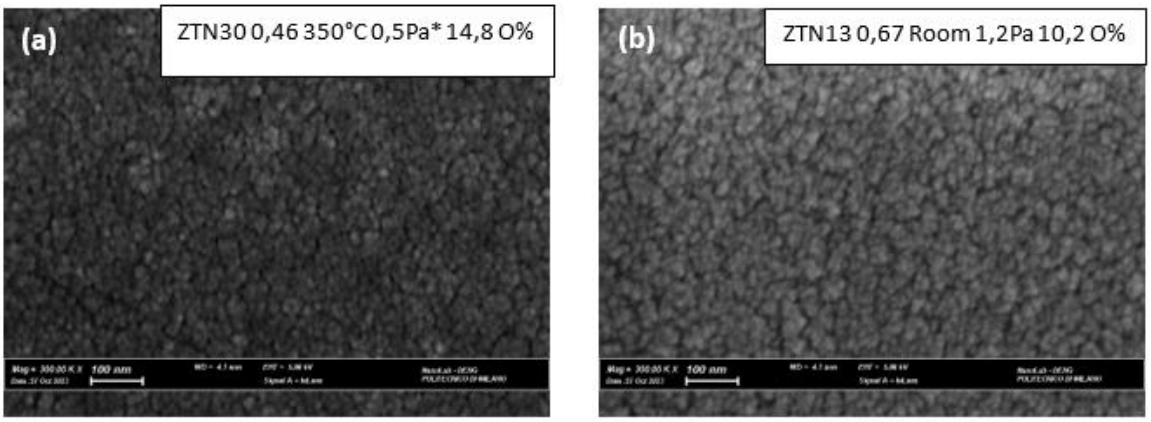

Figure 3.10: SEM images in plane on different samples in different condition, (a) 0,5 Pa of Nitrogen and 0,5 Pa of Argon and (b) with 1Pa of Nitrogen, the deposition condition are indicated in the upper part of the images, magnification of 300.000x.

In the oxidize samples, the SEM analyses (Figure 3.11) shows a uniform compact coverage with small protuberance all over the sample. These features can be seen at lower magnification. Note that all the samples that shows this oxide patina, changed the colour.

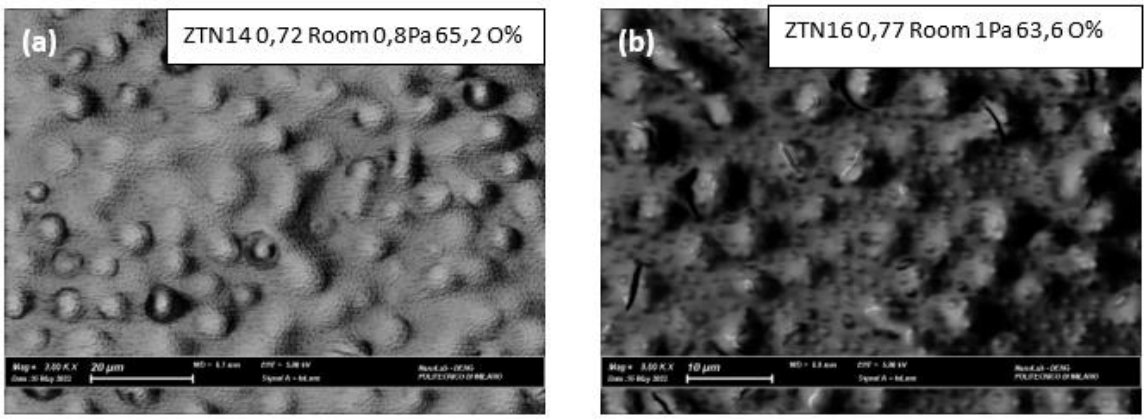

Figure 3.11: SEM images in plane of oxidized sample (a) and (b) taken with 7000 and 5000 magnification respectively.

3.2.2. Cross-section images

SEM measurements was also done in cross section in order to see the microstructure and a typical columnar structure is shown in all the samples [71], the main difference is that increasing the zinc content as seen in Figure 3.12, the structure became more and more oriented reaching a perfectly vertical direction when the Zn/(Zn+Sn) is 0.69 (here the cross-section measurement were done before the oxidation of this sample and the oxygen value is marked as *). As noticed in Figure 3.13 the lower nitrogen pressure led to a formation of a different structure with dispersed grains, as the pressure of 1.2Pa is reached the images reveals a defined columnar structure.

So, an increasing of Nitrogen pressure is beneficial for the film growth, in particular the structure is well defined at 1.2 Pa while values of 0.5 and 0.8 Pa are detrimental for a correct columnar growth, this could be explained due to the scarcity of energy given by the nitrogen to the metal's atoms to grow properly. with cross section an increase in width of the columns can be observed. As seen with in-plane measurements, the higher growth temperature favours the coalescence of grains [72],

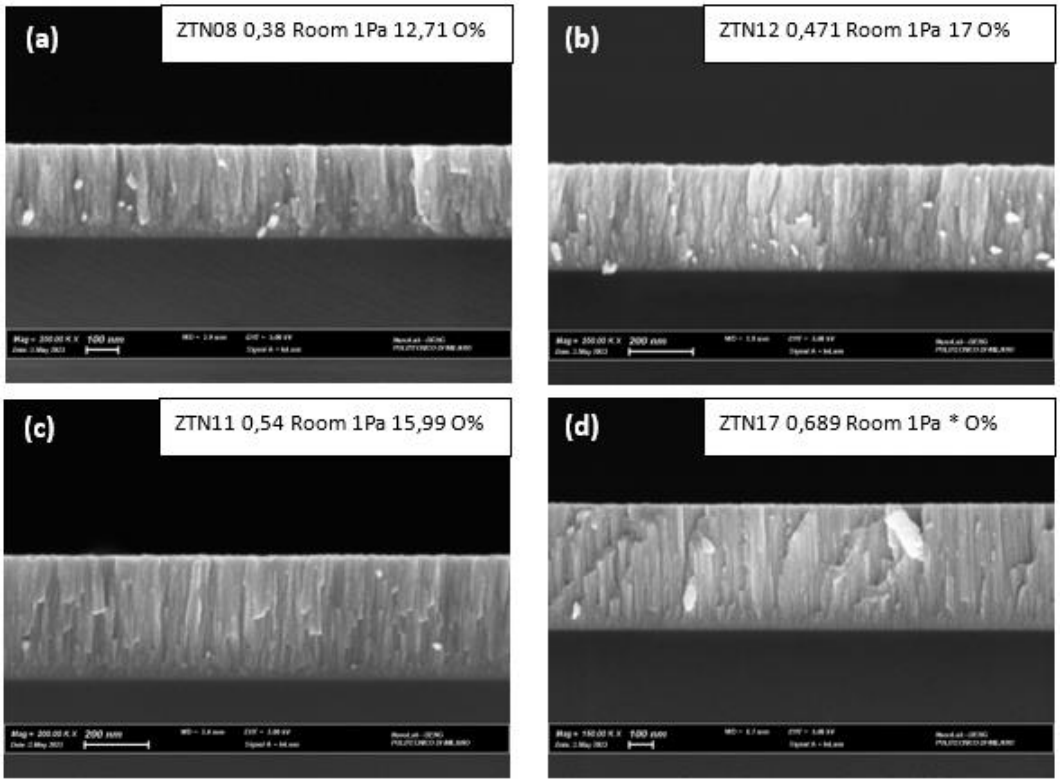

Figure 3.12: Cross section images of samples that features different Zn/(Zn+Sn) ratio.

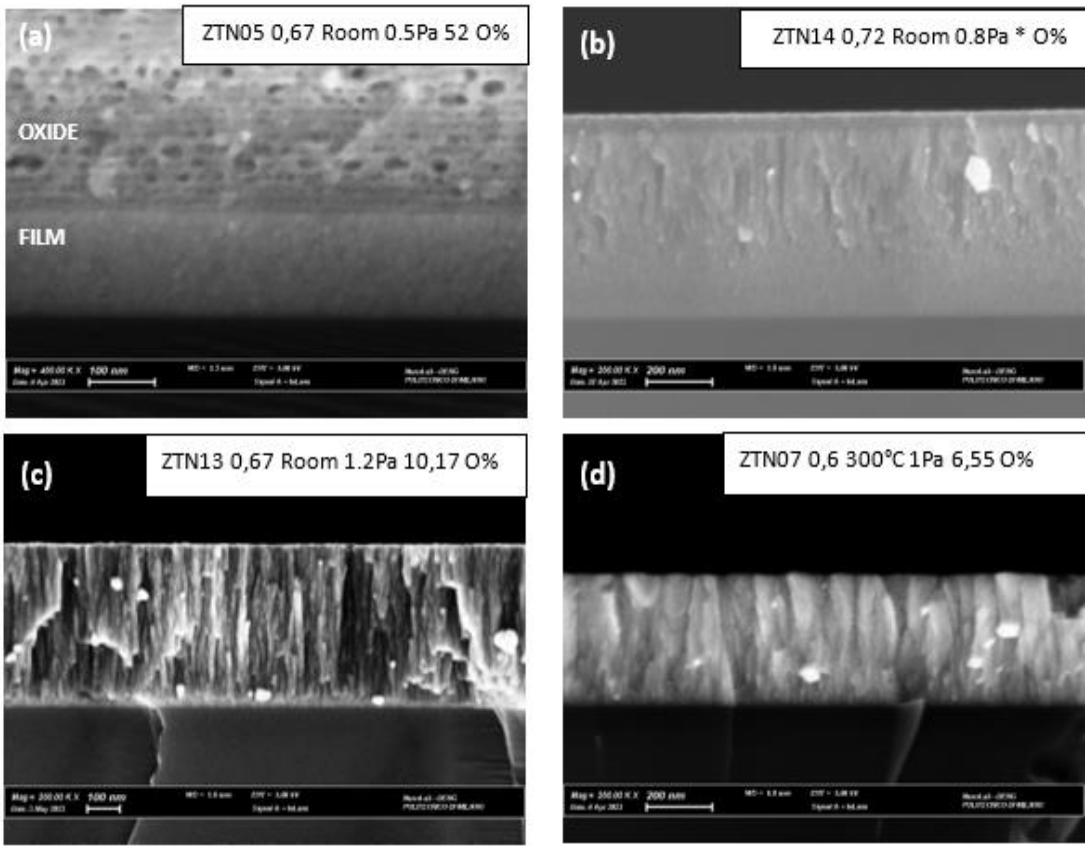

Figure 3.13: Cross section images of samples that are grown with different Nitrogen gas pressure (a) to (c) or with a growth temperature of 300°C.

From Figure 3.14, the structure modifies losing the columnar structure when the growth temperature is high as 300°C while for Zn/(Zn+Sn) composition lower than 0.69, the heated substrate doesn't modify the columnar shape. This particular effect is shown also for samples grown at 100°C with a Zn/(Zn+Sn) of 0.72.

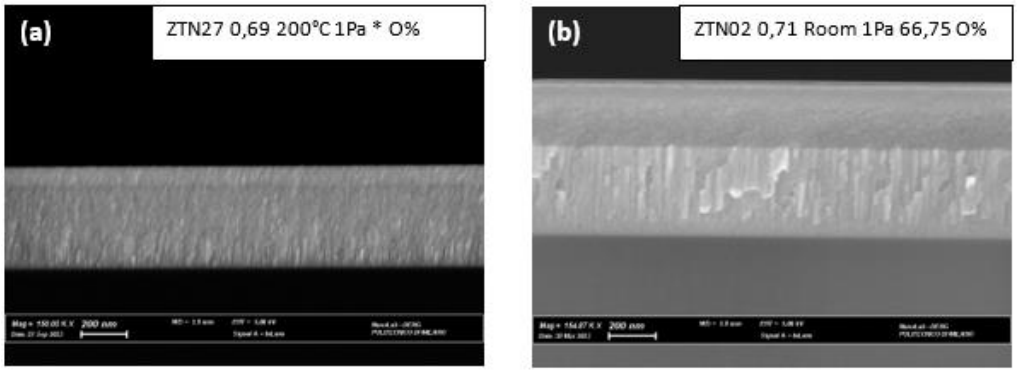

Figure 3.14: SEM Cross section images, (a) deposited on a heated substrate (200°C) and (b) deposited at room temperature; effect of growth temperature on Zinc rich samples.

This behaviour may be due to the formation of another compound that is favoured at high temperature, due to the high Zn concentration in the film. This trend is not shown in literature and further investigation need to be done, a route could be to perform an XRD analyses to see if another phase is formed.

Also, an investigation on the oxidation process was developed for one sample. In Figure 3.15 are shown the step of oxidation process. The sample considered was deposited without heating the substrate and with 0.8 Pa of nitrogen and features a Zn/(Zn+Sn) of 0.72- The microstructure became to change from the bottom and is granular while columnar at the top, in the following days the columnar appearance disappears indicating a loss in crystallinity and here began the exchange of nitrogen-oxygen with the environment forming a spongy oxide patina. It interesting to note that the sample does not form the patina during the first six days after the deposition but the increasing in thickness happens very fast in only one day (b) to (c).

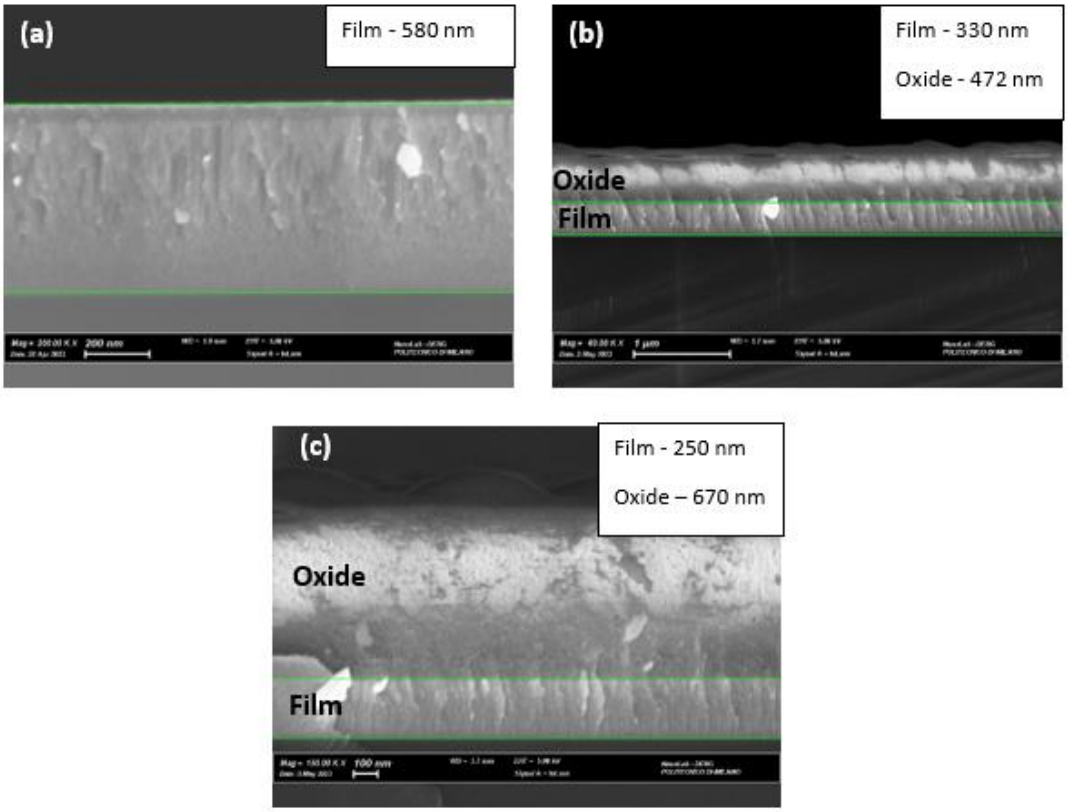

Figure 3.15: SEM cross section images showing the evolution of the oxide layer, (a) after 6 days from the deposition, (b) after 10 days, (c) after 11 days; the thickness of the film and oxide are shown in the white box.

3.3. XRD analysis

The understanding of the crystalline phase of the $ZnSnN_2$ is a key point to control the material's properties. XRD measurements (Figure 3.16) were performed on 11 samples that varies in composition as well as in the growing temperature spanning from room temperature to 300°C. For comparison, the peaks related to wurtzite arrangement are taken from [73]–[76].

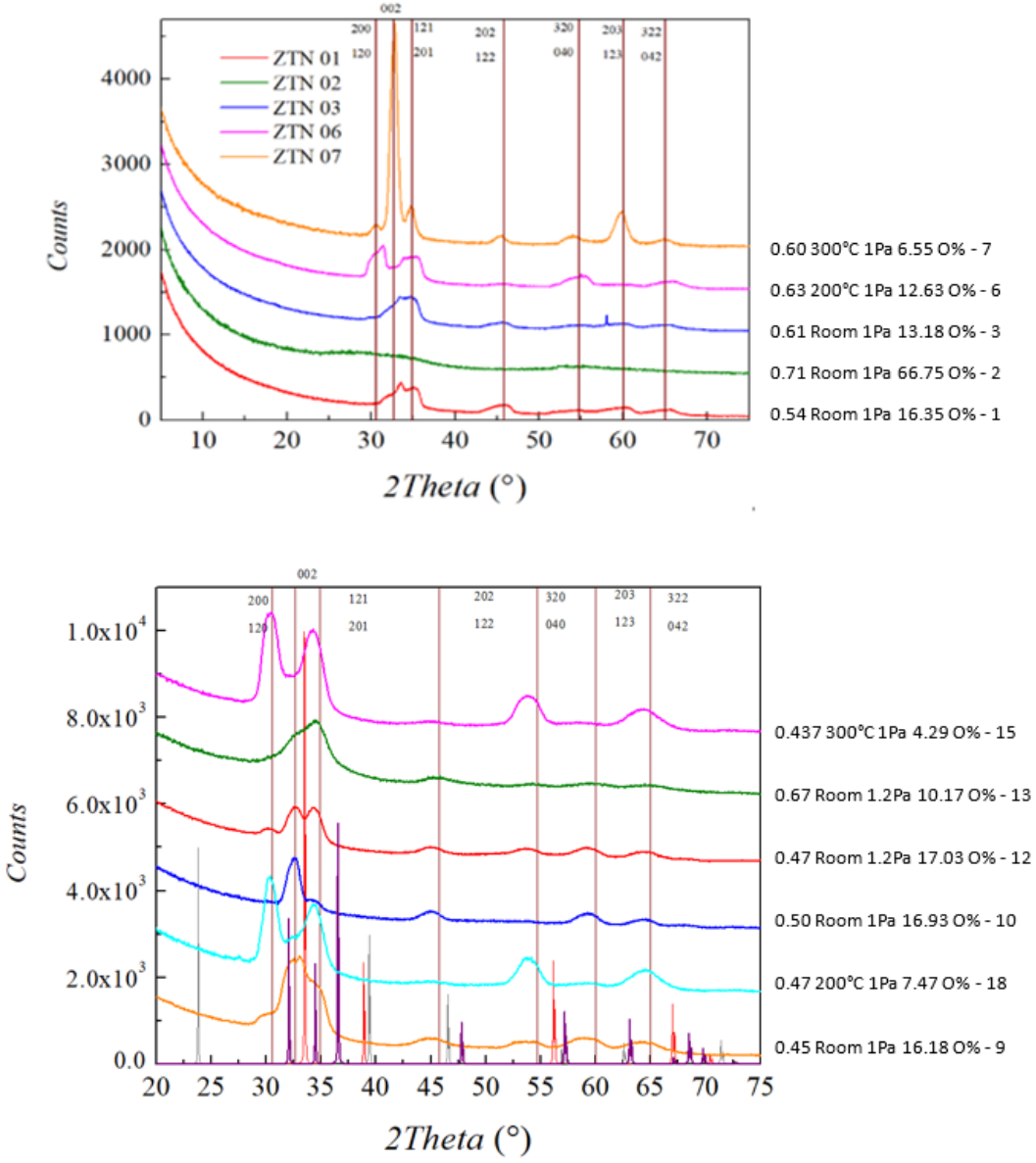

Figure 3.16: XRD spectra, each spectrum is labelled as follows: Zn/(Zn+Sn), deposition condition, oxygen percentage and number of the sample. Red reference line are referred to ZnO cubic standard, Blue to ZnO hexagonal standard and gray to α-Sn standard [74]–[76].

The best matching spectra is exhibited by the sample 7 done at 300°C with 1Pa of pure nitrogen and the film has a Zn/(Zn+Sn) of 0.6, more precisely has a composition of $Zn_{0.3}Sn_{0.2}N_{0.5}$ with a 6.55% of oxygen impurity. The wurtzitic peaks and orthorhombic pna21 peaks are matching with except of additional peaks can be found in the proximity of 30.6° and 34.9° (Figure 1.10). Moreover, observing the FWMH that is the full width at half maximum of the 30.6° and 34.9° peaks is about the double of the peak at 32.7° indicating a possible Pna21 structure arrangement only for sample 7 [15][33]. With a similar composition, the sample 13 that matches with most of the predicted peaks but shows a lower degree of crystallinity, the peak located near 31° has a very low intensity. The peaks don't match perfectly in all the samples since the peak intensity is related to the distance of the crystalline plane that can be modified due to the presence of oxygen or unreacted metal atoms.

The ratio Zn/(Zn+Sn) strongly influence the growth of ZTN (as seen in previous paragraphs) hence the position of the peaks. For a high concentration of zinc, the four peaks located at values higher than 45° are precisely located in the predicted position. For lower concentration of Zn/(Zn+Sn), the peaks are shifted toward left. That means that the growth planes are more distant with respect to theoretically predicted. This could be explained since the atomic radius of Tin (140 pm) is higher than the atomic radius of zinc (134 pm) so it occupies more space inside the cell and deforms the sublattice [31].

It's interesting that samples synthesized at different deposition conditions but having the same Zn/(Zn+Sn) composition, shows different crystalline structures [18]. Considering the first three samples (7,6,3) that possesses a content of Zn/(Zn+Sn) in the range of 0.61-0.63 it's clearly that the film shows crystalline structure only when the substrate temperature is of 300°C. A trend can be observed due to this measurements, that is the peak located at 31° is characteristic only for samples grown at temperature higher than ambient temperature or grown with a pressure of nitrogen equal to 1.2 Pa. At high growth temperatures when the film is poor in zinc, the film growth in two preferential directions: 200 and 121.

It's possible that all the zinc deposited doesn't bond perfectly with nitrogen and Tin, and when the Zn/(Zn+Sn) is almost 0.5, the four peaks predicted are shifted toward left and a precise real stoichiometry in the film isn't fulfilled.

Stoichiometric ZTN (sample 10) exhibit all the peaks but shifted and the peak related to 31° is missing. At higher zinc content, 0.67 Zn/(Zn+Sn) all peaks are matched but with poor degree of crystallinity. Going to higher growth temperatures of 200° and 300° in samples with 0.43-0.47 Zn/(Zn+Sn) the peak located at 32.5° is missing while is shown for the same composition when It's deposited at room temperature.

That is, a combination of high-pressure deposition, a temperature higher than 300°C and an over-stoichiometric zinc content favours a correct growth of predicted ZTN wurtzite structure, more calculations need to be done to see if the phase is orthorhombic, since the peaks related to wurtzite and orthorhombic phase are very close. Our samples can be compared with literature results [18] giving the same trend regarding the content of zinc and the growth temperature. It's clear from Figure 3.17 that increasing the temperature the first and third peak increases in height while increasing the zinc content all the peaks became more defined. The same trend it's exhibited by our samples.

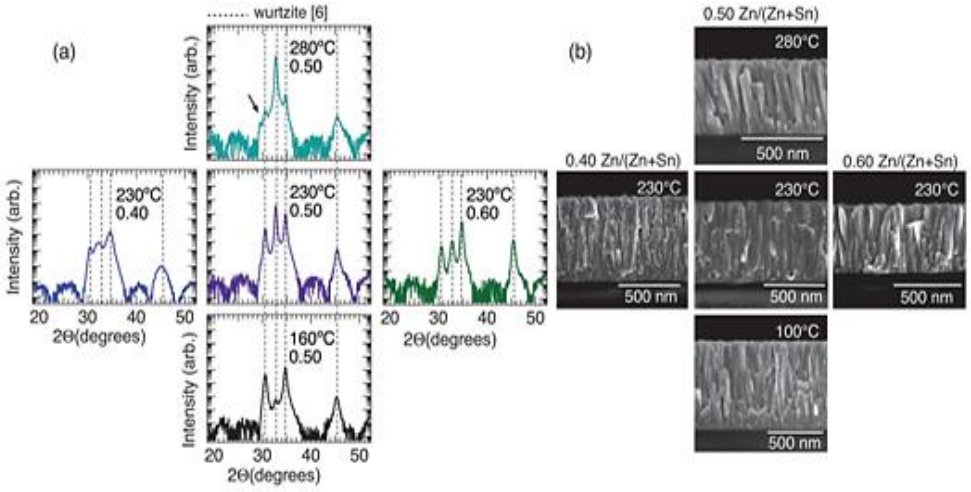

Figure 3.17: (a) XRD patterns for different film composition and growth temperature. numbers in each pattern shows the Zn/(Zn+Sn) composition and dotted lines refer to Pna21 orthorhombic crystal structure. (b) SEM cross section images corresponding to the XRD shown [18].

3.4. Raman analysis

During the master thesis a Raman analysis was performed for each of the 31 samples (Figure 3.18). What can be achieved are the differences in Raman spectra of our samples. Since the vibrational modes are characteristic for each bond, when the composition of the film changes, the vibrational modes change according to the disorder introduced in the film. Theoretically in the Raman spectra the peaks are sharp indicating a specific k-vector selection rule. It's interesting that none of our samples show the predicted peaks. Our Raman pattern resemble what found by Quayle et al. and it's very close to the phonon density-of-state spectrum of $ZnSnN_2$. When there's a very disordered lattice i.e., wurtzite, this kind of phonon-glasslike characteristics is exhibited [34].

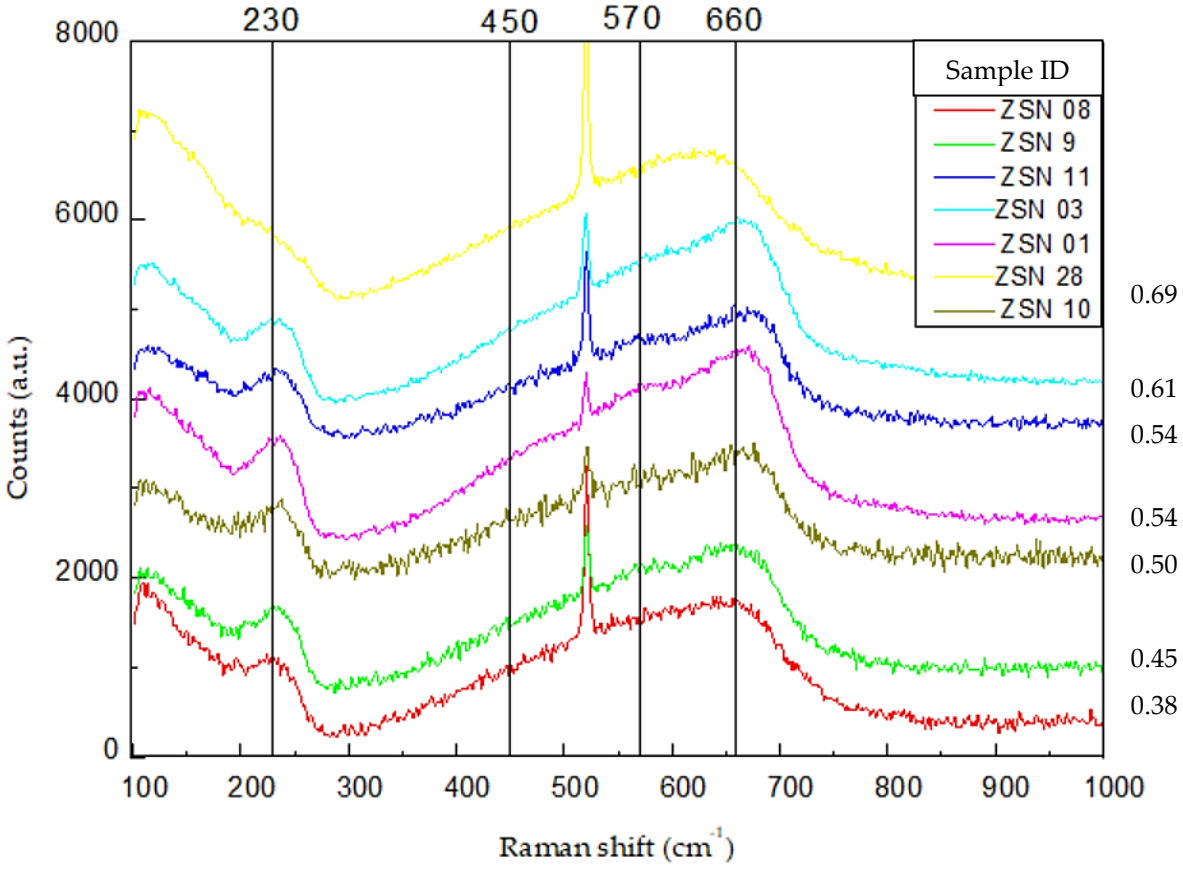

Figure 3.18: Raman spectrum of different sample based of various Zn/(Zn+Sn) ratio (in the right) , deposited with 1Pa of Nitrogen at room temperature, the lines indicate the broad bands observed, the peak at 450 is taken from [34] as reference.

Although all the samples are not perfectly stoichiometric, the Raman spectra resemble the one of $ZnSnN_2$ structure, indicating that the excess of atoms act as defects while maintaining a wurtzite-like structure. Since the Raman spectra peaks aren't really defined, it suggests that the structure is composed of mixed crystallographic phase [31], [70].

Particularly we found a region of stability that goes from 0.44 to 0.67 Zn/(Zn+Sn) in which the main peaks are observed accordingly to literature [31], [71]. They are slightly shifted with respect to the theoretical peaks, and we found peaks at 230, 450, 570 and 660 cm^{-1}.

The observed peak at 570 doesn't perfectly match with what found in literature while the other peaks are very close to the predicted peaks. Also, in literature a slight difference in peaks location is founded as the peaks are broad, the precise position is difficult to determine [31], [34], [71].

The peaks at 100 cm^{-1} theoretically related to a glass-like structure [39] can't be observed since our instrument has a full scale at 100 cm^{-1} that can deflect the real results and so values near 100 cm^{-1} can't be considered. In Figure 3.18 the focus is on the Zn/(Zn+Sn) ratio while the effect of Temperature is treated in the next chapter. Starting from an under-stoichiometric sample, a peak at 230 cm^{-1} is observed and it's always present for each sample deposited at every condition and its shape and intensity isn't modified for samples that possesses a Zn/(Zn+Sn) under 0.67. A trend that can be seen in the Raman comparison is that when increasing the zinc content in the film the peak at 660 cm^{-1} became more intense with respect to the peak located at 565 cm^{-1} [34]. Furthermore, the peak related to 450 cm^{-1} vibrational bond is weak and broad for every sample, so the exact position is difficult to determine. The peaks related to 230 and 660 cm^{-1} are related to $ZnSnN_2$ structure, to Zn-N bonds, and cannot be related to other zinc or Tin mixed phase with nitride such as Zn_3N_2 or Sn_3N_4 [34]. Sample that possesses a Zn/(Zn+Sn) in the range of 0.52 to 0.54 shows the peak at 670 cm^{-1} slightly shifted toward right.

No peaks related to Sn phase located at 126.6 cm^{-1} can be observed, this could be due to the intense light absorption related to the strong light absorption caused by the metallic particles [34].

As a quasi-stoichiometric balance of zinc is reached, a new stable phase may appear modifying the Raman spectra [31]. For off stoichiometric samples when the zinc content is increased up to 0.67 Zn/(Zn+Sn), the peak at 660 cm^{-1} shifts at 625 cm^{-1}.

According to literature, the peak at 556 cm^{-1} is clearly related to the Zn_3N_2 [31] film fabricated with DC-sputtering, and this explains why the peaks related to 660 cm^{-1} [34]shifts by the left when the zinc content is higher than 0.67. Is difficult to clearly assign a vibrational mode for each peak since also the role of oxygen must be considered and the bonds modifies. The trend is that the peaks are well resolute in the range of 0.437-0.67, if the ratio is under this value the zinc cannot bond properly with giving broad peaks related to Zn-N bonds while if the ratio is higher an excess of zinc is incorporated in the film giving a broad peak that may hinder other secondary peaks and giving rise to a different disordered crystalline structure.

Recalling the fact that if the Zn/(Zn+Sn) is higher than 0.67, the atomic oxygen content % in the film increase abruptly. To see if this broad peak is related to any contamination of oxygen, five samples were put in a vacuum bell jar for doing more consideration.

Since the trend remain unchanged for the samples put in jar, only the sample fabricated in standard condition i.e., 1Pa of pure nitrogen and at room growth temperature are depicted in Figure 3.18. In Figure 3.19 the comparison between the same sample left in atmosphere and put in vacuum right after the deposition is shown.

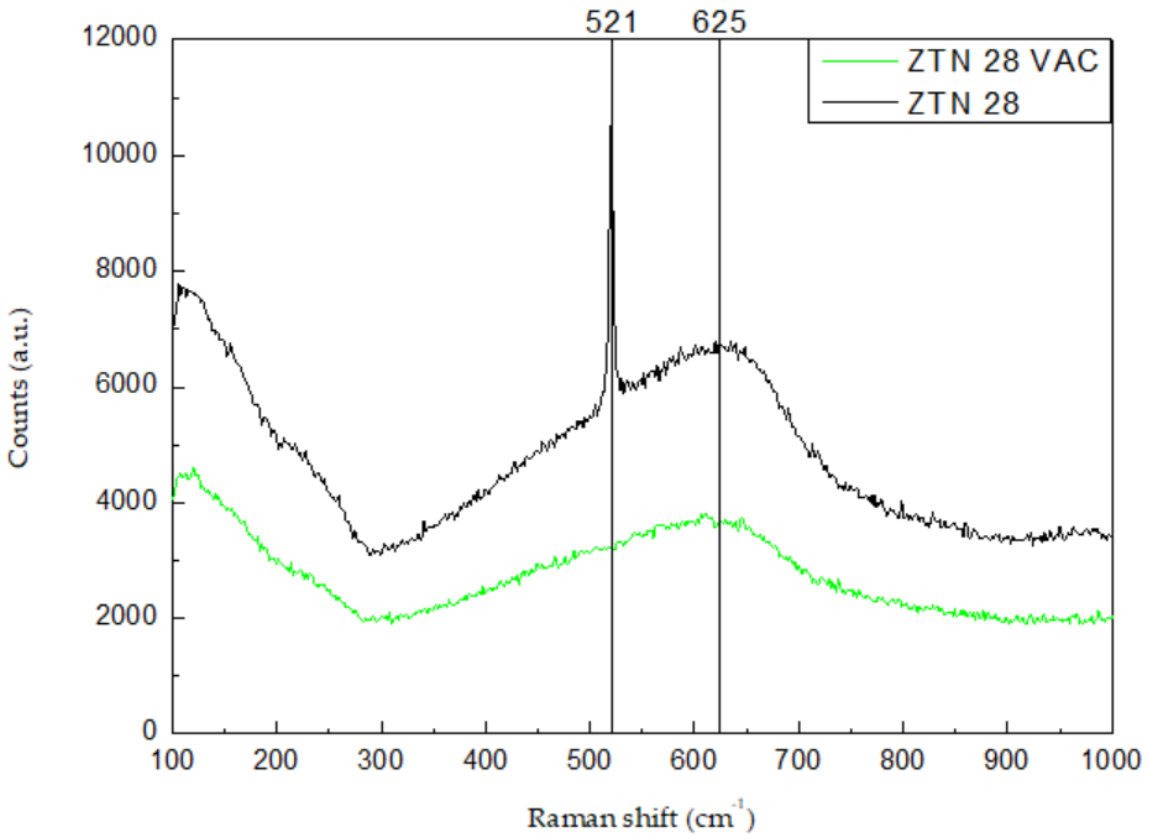

Figure 3.19: Raman spectra of sample growth at room temperature with 1Pa of Nitrogen with a Zn/(Zn+Sn) of 0.685, the green line indicate that the sample was put in vacuum and so a little oxygen contamination has happened. The peak at 521 cm^{-1} indicates the presence of Si while the broad band at 625 is showed for doing comparison and no peak shift is observed.

It's evident that the Raman spectra of the same sample put in two different conditions shows the same broad peak in the same position. So, this peak cannot be related to any vibrational modes given by oxygen but instead to the Zn-N bonds. Another interesting result that can be seen through this Spectra is that the peak related to Si substrate hence at 521 cm^{-1} [77] is missing in the sample put in vacuum while is shown in the sample left in an open environment. A consideration can be given to explain the presence of this peak. When considering this sample, the atomic oxygen content of the sample put in vacuum was of 9.51% while after leaving the sample in an open room it raises up to 62.54%.

The Si peak appears only in oxidized sample, suggesting that the green light used to make Raman measurements can pass through the film and so the bandgap is higher than the energy related to the green light. In the non-oxidized sample, we expect a bandgap smaller than the energy related to green wavelength. As explained, the presence of the Silica peak can discern immediately the sample that present a high bandgap without doing any further measurements.

Moreover, the Raman spectra of deposited samples at different growth temperatures (Figure 3.20) is analyzed. The spectra seem quite similar with no difference in the peaks shape or position for the same content of Zn/(Zn+Sn) in the film. A comparison between different gas pressure is here reported. For samples grown at pressure higher than 1 Pa, the vibrational modes remain unchanged [70].

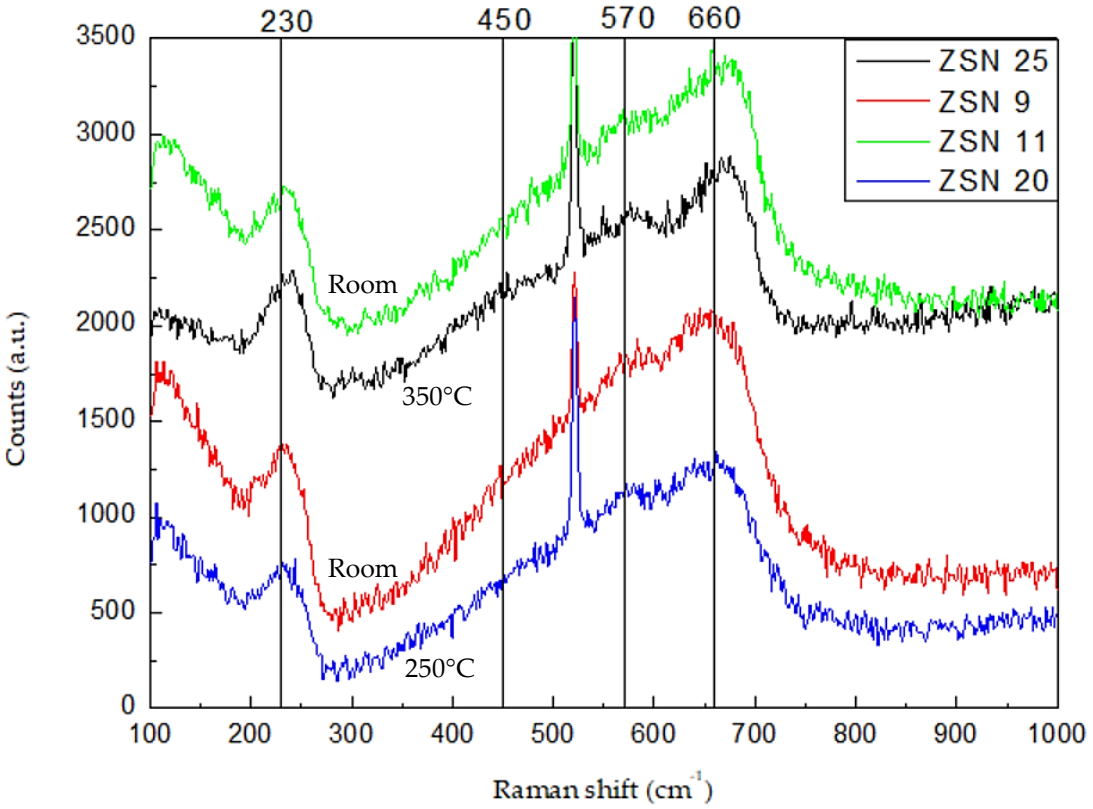

Figure 3.20: Raman spectra of samples with similar composition Zn/(Zn+Sn): red and blue 0.45, black and green of 0.53. The temperature indicates the growth temperature of the related sample.

In the Figure 3.21 it's shown the difference between samples deposited at 1 Pa and samples deposited at 0.5 Pa of N_2 and 0.5 Pa of Ar for a total pressure of 1Pa.

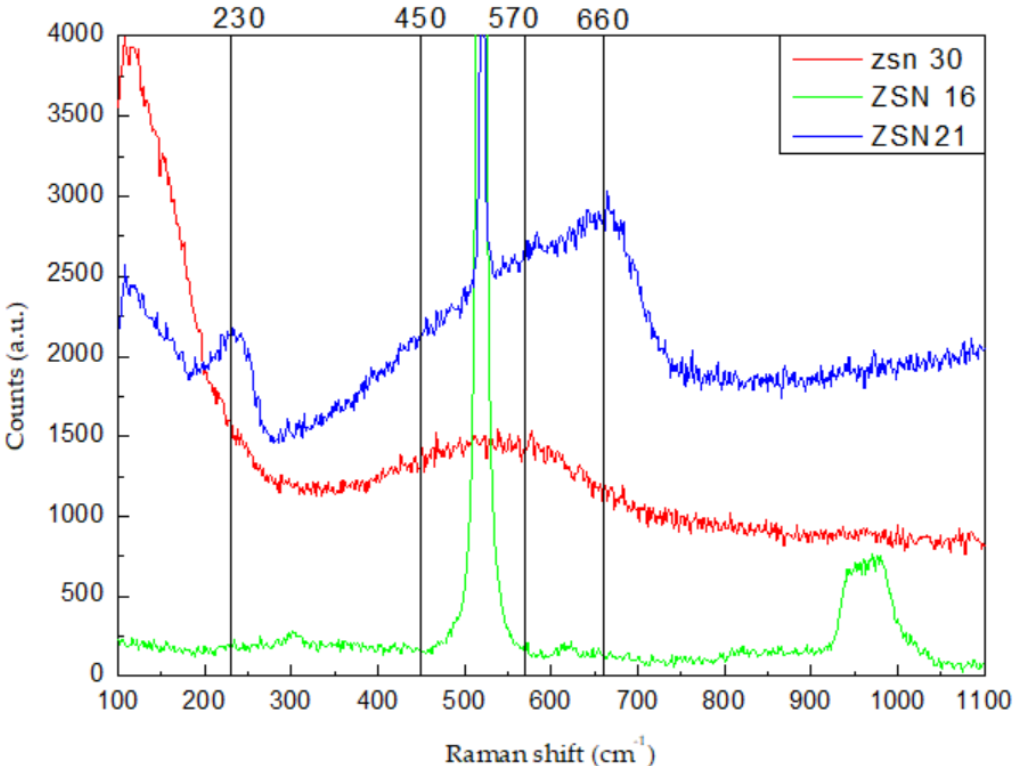

Figure 3.21: Raman spectra of samples growth in different condition, the blue Raman spectra is the typical spectra associated to ZTN, the red spectra is shown by a sample growth with 0.5Pa of Nitrogen and the peak at 230 cm^{-1} is missing, the green spectra is of a sample exposed to ambient for weeks and no peaks with exception of Si can be noted.

In addition, the green sample shows only the peak related to Si, 521 cm^{-1} [77] and around 960 cm^{-1} [78].

It is evident that the peak related to Zn-N vibration located at 230 cm^{-1} [31] is not present in the sample deposited with 0.5 Pa. So, the Nitrogen pressure lower than 1 Pa doesn't give the formation of the correct $ZnSnN_2$ structure in these deposition condition Table 1.

3.5. Electrical properties

The interaction with materials and light is studied thanks to optical measurements [79]. A total of 56 measurements were performed on 13 samples but since Hall measurements are very sensitive and not always precise, only 18 results are here considered. Not all the data collected present a standard deviation since in most of cases measurements gives reliable data only one time. The reliability of electric measurements data relies in the FoM (see Van der Pauw method) that was around 1. In this paragraph is shown the connection between the composition of the film and its related electrical properties. As stated, the content of zinc inside the material strongly affects the optical and electrical properties [16], [35], [47], to perfectly tailor the bandgap of this material, an investigation is needed. The interplay between the defects inside the material are of paramount importance for the related properties. The carrier density is depicted in Figure 3.22.

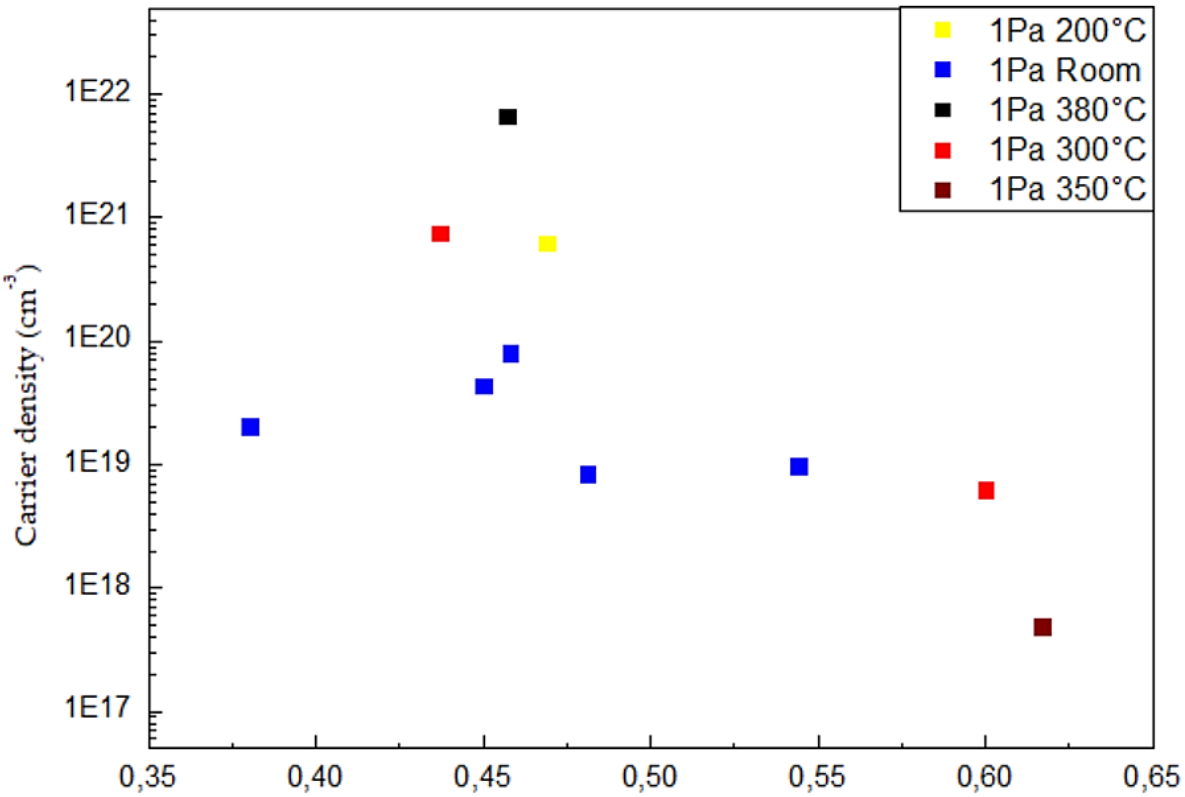

Figure 3.22: Plot of carrier density based on the Zn/(Zn+Sn), as the Zinc content increase in the film, the carrier density lowers.

The Figure 3.22 shows a linear decrease in the carrier density from $8x10^{21}$ to $5x10^{17}cm^{-3}$ as the Zn/(Zn+Sn) increase from 0.43 to 0.63 in samples grown on a heated substrate (200-350°C) while for samples grown at room temperature the carrier density remains stable in the range of 10^{19} cm^{-3}. This carrier density values are in accordance with what found in literature [29], [31], [47].

As seen in literature (Figure 3.23), increasing the zinc content in the film transmute in a decreasing of carrier concentration, that is explained by the suppression of the donor defect Sn_{Zn} [19], [29]. Furthermore, Zn substitutional on Tin act as acceptor and the combined effect gives rise to an abrupt decrease in carrier density up to two orders of magnitude [31]. This trend is showed also by this samples synthesized in laboratory [29]. At higher values of zinc in the film, the carrier density is promising since the lowest value of carrier density for ZTN ever found (July 2023) is of 6.46 x 10^{16} cm^{-3} for a DC magnetron sputtered thin film [34].

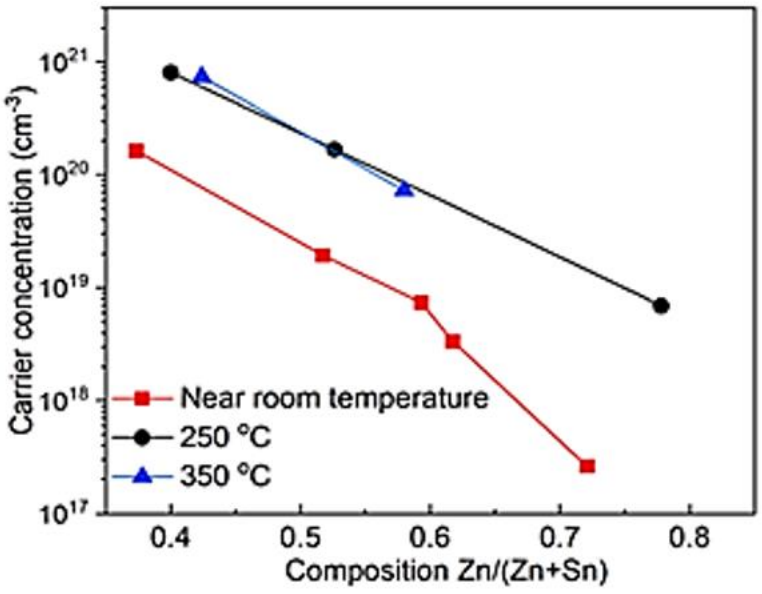

Figure 3.23: Carrier concentration as a function of Zn/(Zn+Sn) in ZTN films deposited at different temperatures [29].

Thanks to electrical measurements also the resistivity value can be obtained, our samples shown very low values of conductivity when deposited at room temperature or when the Zn/(Zn+Sn) is 0.60. In the range of Zn/(Zn+Sn) equal to 0,45 the

temperature affects the conductivity, in particular when the samples are grown at higher temperatures, they exhibit a greater conductivity. Our results are in good agreement with what found in literature [29], [40] since each deposition method gives different values for conductivity but always in the range of 1-100 S cm^{-1}.

A similar effect can be found in Ren et al. work [34], for Zn rich film the conductivity is very low even when a post annealing treatment takes place while for lower content of Zn the thermal effect largely impacts on the conductivity of the films. Even if the post-annealing process was not performed on the samples considered for this thesis, the high growth temperature shows the same trend.

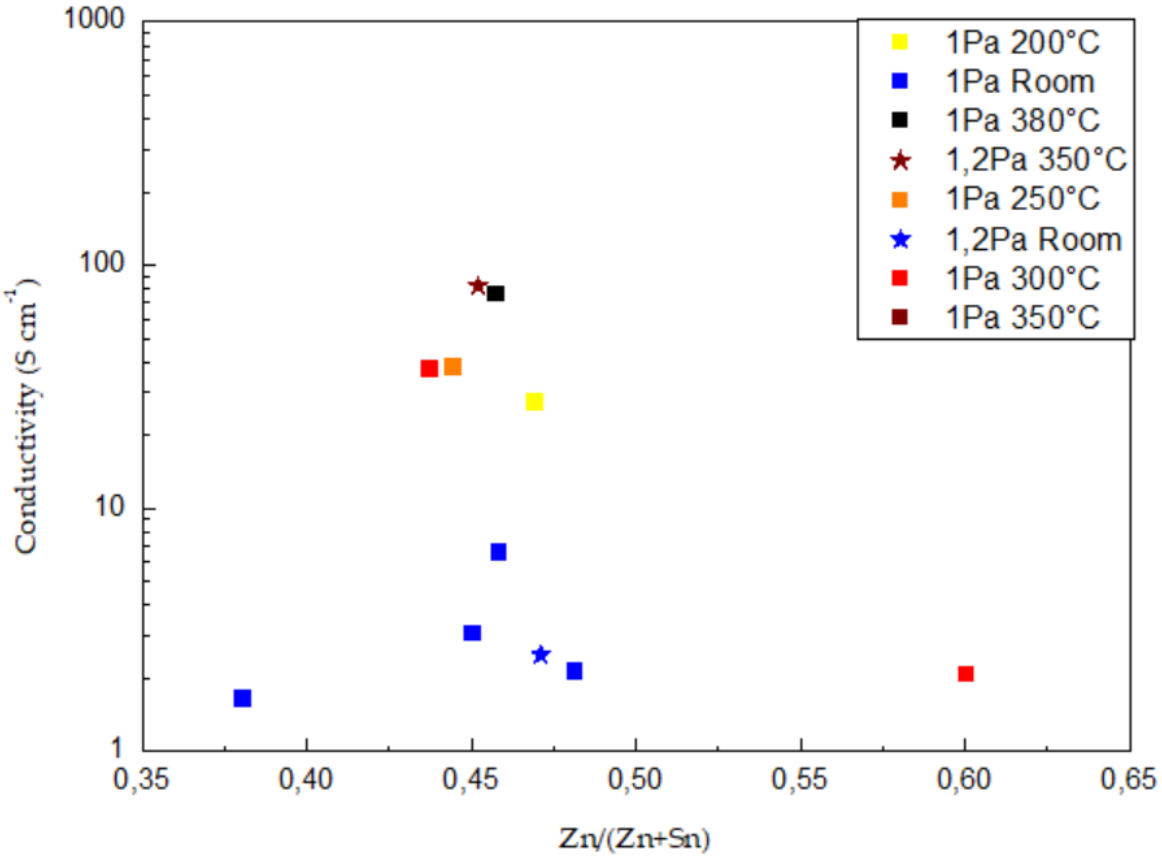

Figure 3.24: Plot of conductivity as a function of Zn/(Zn+Sn), the samples deposited at different temperatures, the heated samples show a conductivity higher up to 10 times.

By plotting the Energy gap value (Figure 3.25), a promising result of 2.15 eV is observed for sample that has a Zn/(Zn+Sn) equal to 0.67 and deposited at Room temperature with a nitrogen pressure of 1.2 Pa.

There is a correlation of the energy gap and the content of Zn/(Zn+Sn), in particular higher value of Zn/(Zn+Sn) are beneficial for achieving a low energy gap. Moreover, when in a situation of under stoichiometry of Zn, the energy gap range from 2.6 to 3.2 eV and no specific correlation with deposition parameters can be found except for samples deposited at 1.2 Pa of nitrogen gas. This could be due to a large quantity of material sputtered toward the substrate deriving from high gas pressure.

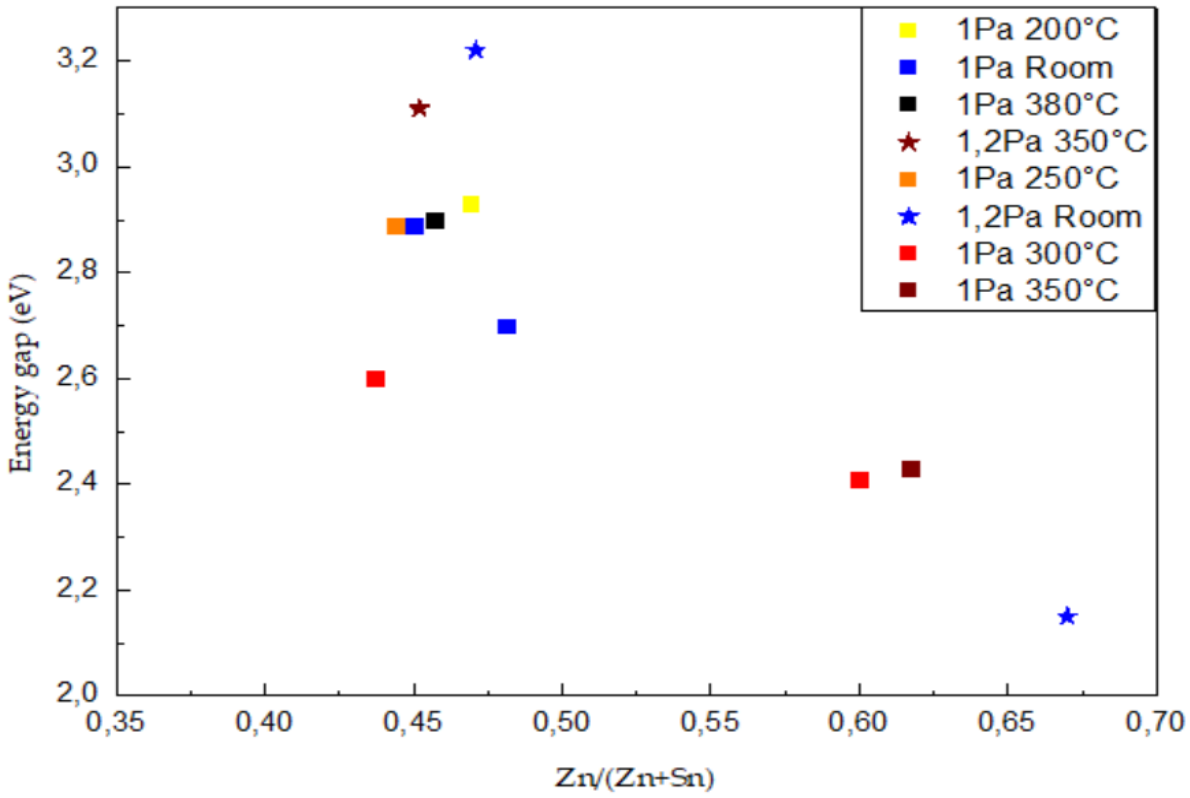

Figure 3.25: Plot of energy gap derived trough Tauc plot as function of Zn/(Zn+Sn), The energy gap id decreasing when increasing the Zn/(Zn+Sn) ratio.

When performing the electrical measurements also the mobility values were detected. The measurements exhibited high variability across each recorded value, and they are not showed here but they stand in the range of 0.3-12 cm^2/Vs in accordance with literature [22].

As both a correlation of the energy gap and carrier density with the increasing of carrier concentration, a graph with a correlation of Energy gap and carrier density need to be plotted. The Burstein Moss effect can be observed also in these synthesized thin films. Observing (Figure 3.26) the energy gap moves from 2.43 to 2.90 eV when increasing the carrier density from $5x10^{17}$ to $6.5x10^{21}$ cm^{-3} in samples grown with high temperature. In samples grown in room temperature the energy gap varies from 2.7 to 2.89 eV when the carrier density moves from $8.4x10^{18}$ to $4.4x10^{19}$ cm^{-3}.

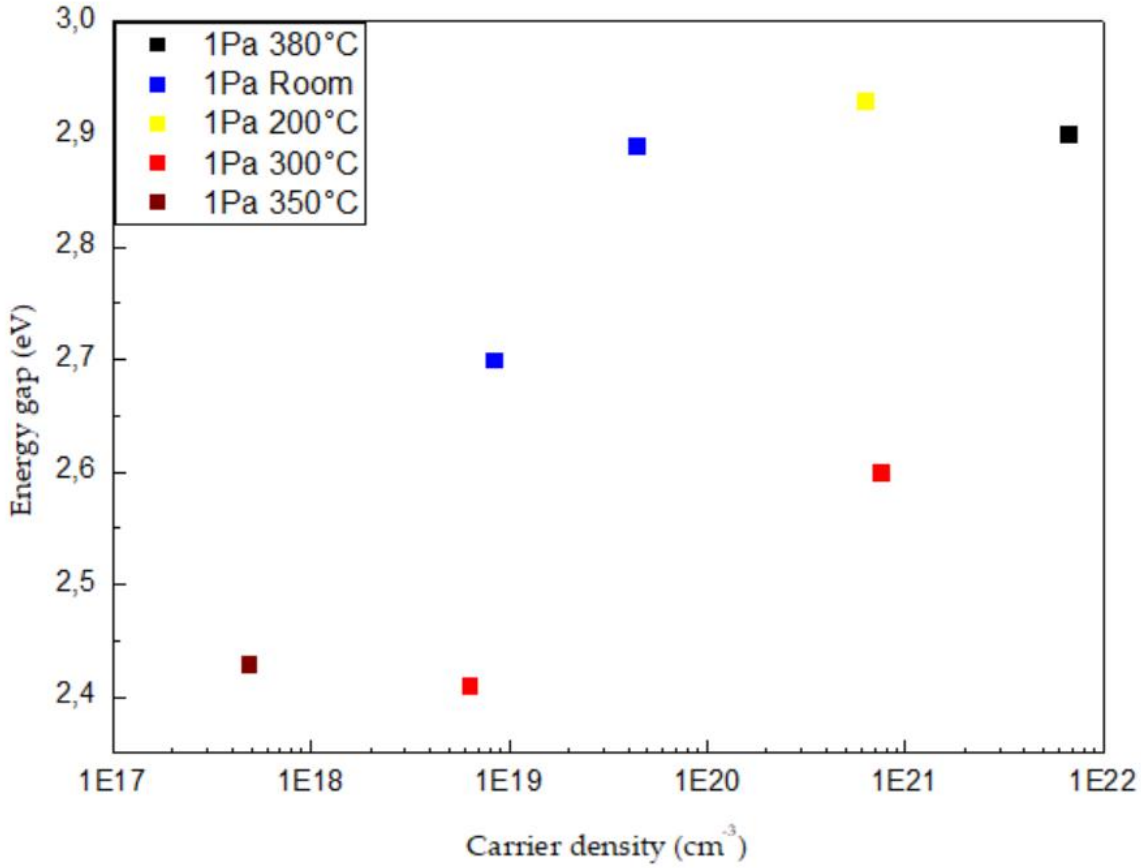

Figure 3.26: Plot of Energy gap as function of carrier density, the energy gap increase as the carrier density increase, hence a Burstein moss shift takes place.

From it can be achieved an increasing in the bandgap value while increasing the carrier density when fixing the growth temperature. Since the data of samples that have both the carrier density and the energy gap value, the graph presents a few numbers of points and further measurements are needed. Furthermore, the pressure doesn't affect the electrical properties of these samples.

3.6. Optical properties

As said before, the Zn/(Zn+Sn) content inside the films affects the optical properties and this behavior is clearly shown trough the Transmittance, Reflectance and Absorbance curves here depicted. In particular when the film exhibits a low Zn content (<0.5 Zn/(Zn+Sn)) the minimum of absorption is reached at 900 nm (Figure 3.27) while increasing the Zn content up to 0.5 Zn/(Zn+Sn) (Figure 3.28 , Figure 3.29) the maximum absorption percentage rise up to 90% instead of 85% and the minimum of absorption il located at 1000 nm. The absorption is related to the energy gap value as follows: when the minimum of absorption shift toward higher wavelengths, the energy gap decrease. With oxidized sample instead the Energy gap becomes very high (up to 3.2 eV) and so the Absorption curve decreases abruptly towards low wavelengths as the material behaves as a dielectric (high transparency).

The optimal condition is shown in the sample with a slight over-stoichiometry of zinc where the minimum absorption is reached at 1200 nm. As seen in Figure 3.25 the energy gap value shift due to the Zn/(Zn+Sn) content and the other deposition parameters seem not to significantly affect the energy gap.

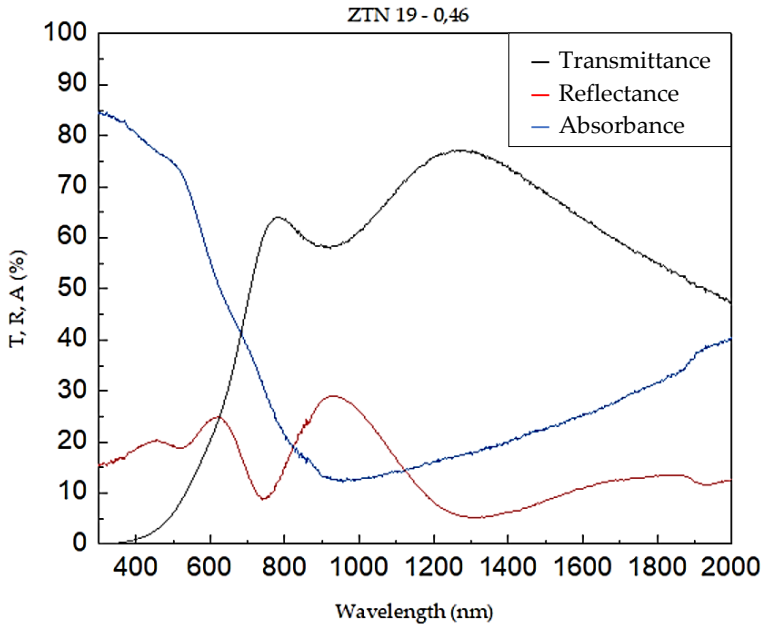

Figure 3.27: Transmittance, reflectance and absorbance of a sample grown at 350°C with 1Pa of Nitrogen is shown, the minimum of absorption Is located in the range of 900 nm. the sample features a Zn/(Zn+Sn) of 0.46.

This trend cab be also seen in optical measurements and only four graphs related to different composition of samples are here reported.

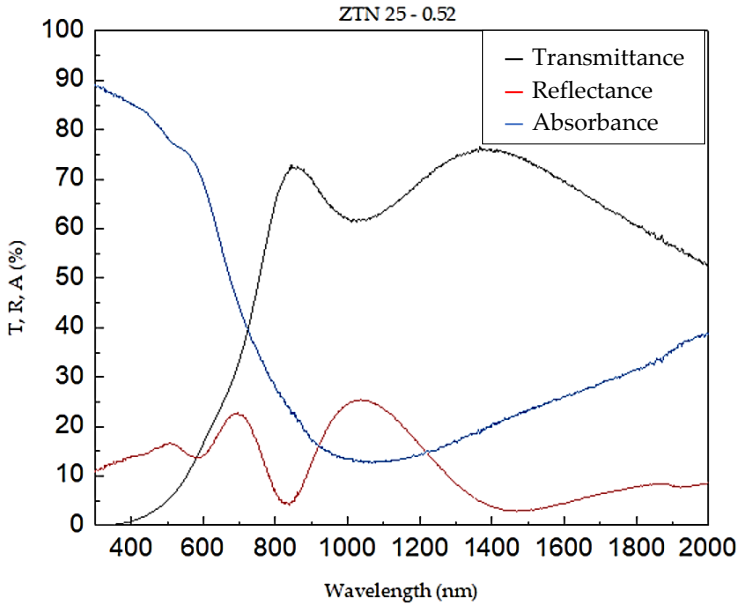

Figure 3.28: Transmittance, reflectance and absorbance of a sample grown at 350°C with 1 Pa of Nitrogen and a composition of Zn/(Zn+Sn) of 0.52.

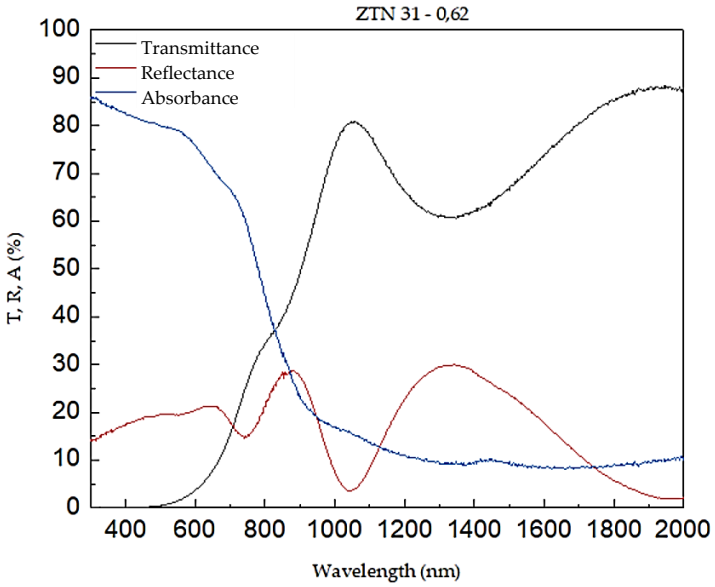

Figure 3.29: Transmittance, reflectance and absorbance of a film deposited at 350°C with 1Pa of Nitrogen that features a Zn/(Zn+Sn) of 0.62.

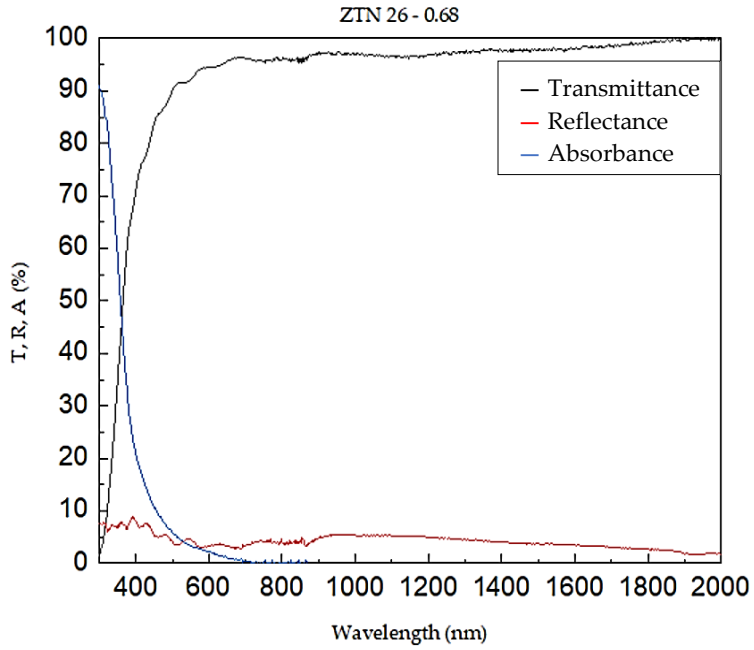

Figure 3.30: Transmittance, reflectance, and absorbance of an oxidized film, the Zn/(Zn+Sn) is of 0.68, the sample is grown at ambient temperature and 1Pa of Nitrogen.

Taking into consideration the values of Transmittance and Reflectance of the sample, the Energy gap can be obtained through the Tauc plot method (Figure 3.31). The energy gap value is given by the intersection between x axis and the oblique linearization of the Tauc plot itself [80].

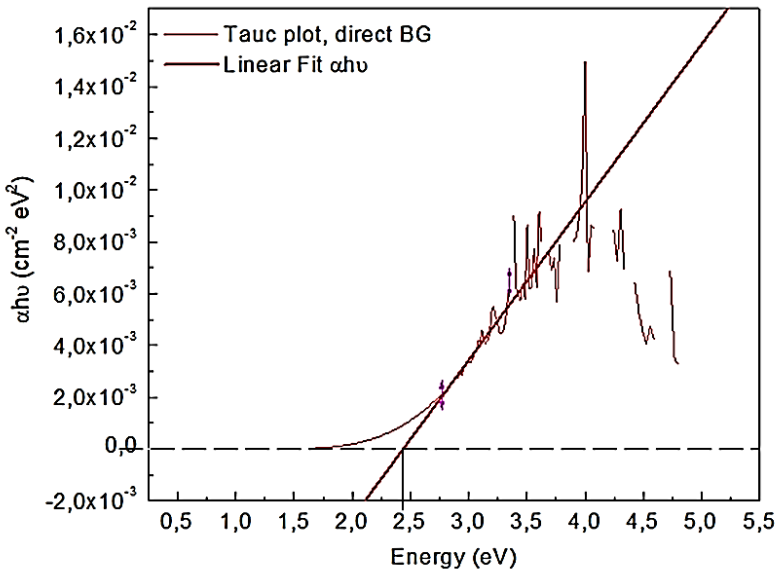

Figure 3.31: Tauc plot of sample with a 0.62 Zn/(Zn+Sn), a bandgap value of 2,4 eV is achieved. Tauc plot referred to sample in Figure 3.29.

4 Conclusions and perspectives

The aim of this thesis was to investigate and explore the properties of $ZnSnN_2$ thin films. This novel material for photovoltaics, in particular this semiconductor was never synthesized in the Nanolab of Politecnico di Milano, so this work is considered as a first explorative approach to the synthesis of ZTN films. Since this material is relatively new, different information about ZTN properties can be found in literature. The understanding of the material properties based on the deposition conditions had a key role in this work, and a full characterization of the morphology, structural, electrical, and optical measurements were performed. Understanding the direct relationship between the material's composition and its energy gap value is crucial. This comprehension is of paramount importance for tailoring the bandgap for specific photovoltaic applications, particularly in the context of tandem solar cells.

During this thesis, the deposition technique chosen was Magnetron Sputtering in DC current mode. It has demonstrated several advantages when depositing $ZnSnN_2$ films on Si substrate. This deposition technique ensures a uniform film, this is crucial when fabricating semiconductors as the surface need to be homogeneous to have reliable performances. With two independent cathodes made of high purity zinc and tin different elemental composition in the films were achieved by modifying the voltage applied to the single cathodes. As the Zn/(Zn+Sn) plays a crucial role in the behavior of this material, the results will be discussed based on this parameter.

The key achievements of this work include:

- **Control over film composition**: Exploiting two different cathodes allows the precise tailoring of all the films composition, featuring a Zn/(Zn+Sn) ratio from 0.38 to 0.78. Depositing at different temperatures (from room to 380°C) was proven to be beneficial to lower the oxygen content inside the film up to 10%, moreover, when working at the same cathode power, the increasing of temperature will lead to a less incorporation of Zinc in the film. Having a correct Nitrogen pressure (≥1Pa) helps the reaching of correct stoichiometry of Zn, Sn and N_2 in the film. A correlation between the cathode's powers and the film composition is founded.
- **Oxidation study**: A precise value of Zinc content, 0.68 Zn/(Zn+Sn) and over, will lead to an uncontrolled oxidation that will be detrimental for electrical application. This oxidation is manifested visibly by a changing in the color of the surface, shifting from green to blue. EDXs measurements highlighted that all the oxidized samples shown an oxygen content up to 67% in the film. Moreover, cross section investigation reveals the formation of a thick oxide layer within days in zinc rich samples, that grows to the detriment of Nitrogen present in the film.
- **Correlation of structure and deposition condition**: The trend is that Zn rich films grown at 300°C features the best grains, the increasing of zinc translates in a defined columnar growth while the temperature increase the size and the packing of the grains, XRD spectra showed a possible Pna21 arrangement but more detailed analyses on FWDH need to be performed. The effect of the substrate temperature in Zn poor films, promote the crystallization on different planes. The films that possess a Zn/(Zn+Sn) ranging from 0.46 to 0.61 shows all the predicted bands that resemble the phonon density of states, the broad bands are shown due to the break of k-selection rule, so a phonon-glasslike structure is exhibited. Moreover, the samples with Zn/(Zn+Sn) higher than 0.67 shows only a broad band due to high Zn concentration. The temperature does not affect the vibrational modes of the deposited films. Additionally, a gas pressure

below 1 Pa hinders the formation of the correct $ZnSnN_2$ structure, as the scarcity of nitrogen does not permit the correct stoichiometry.

- **Contribution to photovoltaics**: An understanding of the correlation between the carrier density and the bandgap value is achieved, of paramount importance for specific solar cells applications as tandem solar cells. A direct correlation between the film composition and the bandgap value is understood, essential for photovoltaics application. As seen in literature, the difficult interplay between the defects and the charge carriers is mainly correlated to the Zn/(Zn+Sn) ratio. To observe this correlation, electrical and optical measurements were performed. The carrier concentration decreased from $8x10^{21}$ to $5x10^{17}$ cm^{-3} as the Zn/(Zn+Sn) increase from 0.45 to 0.62. The Burstein moss shift is observed due to an increasing of the energy gap value when increasing the carrier concentration. The most promising film shown a bandgap value of 2.11 eV.

Future research is moving toward the implement of the High Impulse Power regime Magnetron Sputtering (HiPIMS) applied on the zinc cathode to see the effect of a high intensity source on the film for improving its stability [14].

I will suggest performing post annealing treatment on the deposited samples to investigate the variation in optoelectronic properties as the annealing will lead to a reorganization of the sublattice modifying the structure. Since the oxidation arise when the Zn-rich films are exposed to air for few days, the annealing could be beneficial to stop the oxidation process. Similarly to the HiPIMS, to decrease the oxygen content inside the film, a bias could be applied to the DC magnetron sputter to give more energy to the charged species in the plasma when impinging the substrate. Would be interesting to see the development of oxide layer during the days after the deposition, performing both EDXs and SEM analyses for tailoring the growth of the oxide for specific applications.

For further deposition I suggest performing a pre sputter on the zinc cathode to avoid any oxygen poisoning. This research shows that the best films feature a little over-stoichiometry in zinc and a deposition on a heated substrate, so, for further deposition, this path Is the best to follow.

For having more specific data on electrical measurements, the number of measurements need to be increased, also moving toward a more precise instrument will lead to understand finely the correlation of the carrier density with the composition of the film. For having a better tailor toward electrical properties, a doping of the ZTN with other metals such as Li, Na, K would enhance the semiconductor properties acting as shallow acceptor to lower the carrier concentration [81]. Moreover, the deposition could be done on substrate-oriented lattice to have a precision control of the structure [28].

The information obtained through this work will serve as a solid base for future research.

5 Bibliography

[1] D. M. Nielsen, "Tailoring functional properties of earth-abundant II-IV-nitride alloys: towards tandem solar cell applications," 2023.

[2] V. V. Mitin, D. I. Sementsov, and N. Z. Vagidov, *Quantum Mechanics for Nanostructures*. Cambridge University Press, 2010. doi: 10.1017/CBO9780511845161.

[3] T. Edvinsson, "Optical quantum confinement and photocatalytic properties in two-, one- and zerodimensional nanostructures," *R Soc Open Sci*, vol. 5, no. 9, Sep. 2018, doi: 10.1098/rsos.180387.

[4] A. N. Fioretti, "Development of zinc tin nitride for application as an earth abundant photovoltaic absorber."

[5] F. Martinho, "Challenges for the future of tandem photovoltaics on the path to terawatt levels: A technology review," *Energy and Environmental Science*, vol. 14, no. 7. Royal Society of Chemistry, pp. 3840–3871, Jul. 01, 2021. doi: 10.1039/d1ee00540e.

[6] R. Corkish, "Solar Cells."

[7] M. A. Green and J. Hansen, "Catalog of Solar Cell Drawing," 2003.

[8] "pveducation.org/pvcdrom/tandem-cells."

[9] F. Deng *et al.*, "Determination of the basic optical parameters of ZnSnN_2," *Opt Lett*, vol. 40, no. 7, p. 1282, Apr. 2015, doi: 10.1364/ol.40.001282.

[10] "The Spectral p-n Junction Model for Tandem Solar-Cell Design."

[11] A. Zakutayev, "Design of nitride semiconductors for solar energy conversion," *Journal of Materials Chemistry A*, vol. 4, no. 18. Royal Society of Chemistry, pp. 6742–6754, 2016. doi: 10.1039/c5ta09446a.

[12] I. S. Khan, K. N. Heinselman, and A. Zakutayev, "Review of ZnSnN2 semiconductor material," *JPhys Energy*, vol. 2, no. 3. IOP Publishing Ltd, Jul. 01, 2020. doi: 10.1088/2515-7655/ab8b69.

[13] K. Javaid *et al.*, "Band Offset Engineering in ZnSnN2-Based Heterojunction for Low-Cost Solar Cells," *ACS Photonics*, vol. 5, no. 6, pp. 2094–2099, Jun. 2018, doi: 10.1021/acsphotonics.8b00427.

[14] V. S. Olsen *et al.*, "ZnSnN2 in Real Space and k-Space: Lattice Constants, Dislocation Density, and Optical Band Gap," *Adv Opt Mater*, vol. 9, no. 16, Aug. 2021, doi: 10.1002/adom.202100015.

[15] P. C. Quayle *et al.*, "Charge-neutral disorder and polytypes in heterovalent wurtzite-based ternary semiconductors: The importance of the octet rule," *Phys Rev B Condens Matter Mater Phys*, vol. 91, no. 20, May 2015, doi: 10.1103/PhysRevB.91.205207.

[16] T. D. Veal *et al.*, "Band Gap Dependence on Cation Disorder in ZnSnN2 Solar Absorber," *Adv Energy Mater*, vol. 5, no. 24, Dec. 2015, doi: 10.1002/aenm.201501462.

[17] A. Virfeu *et al.*, "Approaching Theoretical Band Gap of ZnSnN2Films via Bias Magnetron Cosputtering at Room Temperature," *ACS Appl Electron Mater*, vol. 3, no. 9, pp. 3855–3866, Sep. 2021, doi: 10.1021/acsaelm.1c00478.

[18] A. N. Fioretti *et al.*, "Combinatorial insights into doping control and transport properties of zinc tin nitride," *J Mater Chem C Mater*, vol. 3, no. 42, pp. 11017–11028, Sep. 2015, doi: 10.1039/c5tc02663f.

[19] I. S. Khan, K. N. Heinselman, and A. Zakutayev, "Review of ZnSnN2 semiconductor material," *JPhys Energy*, vol. 2, no. 3. IOP Publishing Ltd, Jul. 01, 2020. doi: 10.1088/2515-7655/ab8b69.

[20] "NREL Materials Database."

[21] T. Dhakal, M. Hamasha, S. Sunkari, L. Ganta, P. Vasekar, and C. Westgate, "Fabrication of Cu 2ZnSnS 4 thin film solar cell using chemical method," in *Conference Record of the IEEE Photovoltaic Specialists Conference*, 2011, pp. 001267–001270. doi: 10.1109/PVSC.2011.6186188.

[22] R. Qin *et al.*, "Semiconducting ZnSnN2 thin films for Si/ZnSnN2 p-n junctions," *Appl Phys Lett*, vol. 108, no. 14, Apr. 2016, doi: 10.1063/1.4945728.

[23] E. Arca *et al.*, "Band edge positions and their impact on the simulated device performance of ZnSnN2-based solar cells," *IEEE J Photovolt*, vol. 8, no. 1, pp. 110–117, Jan. 2018, doi: 10.1109/JPHOTOV.2017.2766522.

[24] M. R. Karim and H. Zhao, "Design of InGaN-ZnSnN2 quantum wells for high-efficiency amber light emitting diodes," *J Appl Phys*, vol. 124, no. 3, Jul. 2018, doi: 10.1063/1.5036949.

[25] A. S. Pawar, H. Shaik, R. K. Naina, K. Naveen Kumar, P. Aishwarya, and R. Imran Jafri, "Growth Of ZnSnN2 Semiconductor Films For Gas Sensor Applications," in *AIP Conference Proceedings*, American Institute of Physics Inc., Nov. 2022. doi: 10.1063/5.0120097.

[26] P. C. Quayle, G. T. Junno, K. He, E. W. Blanton, J. Shan, and K. Kash, "Vapor–liquid–solid synthesis of ZnSnN2," *Phys Status Solidi B Basic Res*, vol. 254, no. 8, Aug. 2017, doi: 10.1002/pssb.201600718.

[27] N. Feldberg, J. D. Aldous, P. A. Stampe, R. J. Kennedy, T. D. Veal, and S. M. Durbin, "Growth of ZnSnN2 by molecular beam epitaxy," *J Electron Mater*, vol. 43, no. 4, pp. 884–888, Apr. 2014, doi: 10.1007/s11664-013-2962-8.

[28] N. Senabulya *et al.*, "Stabilization of Orthorhombic Phase in Single-Crystal ZnSnN 2 Films."

[29] Y. Wang, T. Ohsawa, X. Meng, F. Alnjiman, J. F. Pierson, and N. Ohashi, "Suppressing the carrier concentration of zinc tin nitride thin films by excess zinc content and low temperature growth," *Appl Phys Lett*, vol. 115, no. 23, Dec. 2019, doi: 10.1063/1.5129879.

[30] X. Cao, F. Kawamura, Y. Ninomiya, T. Taniguchi, and N. Yamada, "Conduction-band effective mass and bandgap of ZnSnN2 earth-abundant solar absorber," *Sci Rep*, vol. 7, no. 1, Dec. 2017, doi: 10.1038/s41598-017-14850-7.

[31] A. Nezhdanov *et al.*, "Mixed phase ZnSnN2 thin films for solar energy applications: Insight into optical and electrical properties," *Opt Mater (Amst)*, vol. 144, Oct. 2023, doi: 10.1016/j.optmat.2023.114335.

[32] F. Alnjiman *et al.*, "Chemical environment and functional properties of highly crystalline ZnSnN2 thin films deposited by reactive sputtering at room temperature," *Solar Energy Materials and Solar Cells*, vol. 182, pp. 30–36, Aug. 2018, doi: 10.1016/j.solmat.2018.02.037.

[33] L. Lahourcade, N. C. Coronel, K. T. Delaney, S. K. Shukla, N. A. Spaldin, and H. A. Atwater, "Structural and optoelectronic characterization of RF sputtered ZnSnN 2," *Advanced Materials*, vol. 25, no. 18, pp. 2562–2566, May 2013, doi: 10.1002/adma.201204718.

[34] J. Ren, L. Liang, X. Liu, and H. Cao, "Physical properties of Zn-Sn-N films governed by the Zn/(Zn + Sn) ratio," *Journal of Vacuum Science & Technology A*, vol. 41, no. 3, May 2023, doi: 10.1116/6.0002454.

[35] N. Feldberg *et al.*, "Growth, disorder, and physical properties of ZnSnN2," *Appl Phys Lett*, vol. 103, no. 4, Jul. 2013, doi: 10.1063/1.4816438.

[36] F. Ye *et al.*, "Nanocrystalline ZnSnN2 Prepared by Reactive Sputtering, Its Schottky Diodes and Heterojunction Solar Cells," *Nanomaterials*, vol. 13, no. 1, Jan. 2023, doi: 10.3390/nano13010178.

[37] X. Wu *et al.*, "Carrier Tuning in ZnSnN2 by Forming Amorphous and Microcrystalline Phases," *Inorg Chem*, vol. 58, no. 13, pp. 8480–8485, Jul. 2019, doi: 10.1021/acs.inorgchem.9b00649.

[38] T. R. Paudel and W. R. L. Lambrecht, "First-principles study of phonons and related ground-state properties and spectra in Zn-IV-N2 compounds," *Phys Rev B Condens Matter Mater Phys*, vol. 78, no. 11, Sep. 2008, doi: 10.1103/PhysRevB.78.115204.

[39] M. González-Jiménez *et al.*, "Understanding the emergence of the boson peak in molecular glasses," *Nat Commun*, vol. 14, no. 1, Dec. 2023, doi: 10.1038/s41467-023-35878-6.

[40] A. N. Fioretti, E. S. Toberer, A. Zakutayev, and A. C. Tamboli, "Effects of low temperature annealing on the transport properties of zinc tin nitride," in *2015 IEEE 42nd Photovoltaic Specialist Conference, PVSC 2015*, Institute of Electrical and Electronics Engineers Inc., Dec. 2015. doi: 10.1109/PVSC.2015.7355694.

[41] X. M. Cai *et al.*, "Fabricating ZnSnN2 with cosputtering," *Surf Coat Technol*, vol. 359, pp. 169–174, Feb. 2019, doi: 10.1016/j.surfcoat.2018.12.080.

[42] S. Chen, P. Narang, H. A. Atwater, and L. W. Wang, "Phase stability and defect physics of a ternary ZnSnN2 semiconductor: First principles insights," *Advanced Materials*, vol. 26, no. 2, pp. 311–315, Jan. 2014, doi: 10.1002/adma.201302727.

[43] J. W. Choi, B. Shin, P. Gorai, R. L. Z. Hoye, and R. Palgrave, "Emerging Earth-Abundant Solar Absorbers," *ACS Energy Lett*, vol. 7, no. 4, pp. 1553–1557, Apr. 2022, doi: 10.1021/acsenergylett.2c00516.

[44] C. L. Melamed *et al.*, "Short-Range Order Tunes Optical Properties in Long-Range Disordered ZnSnN2-ZnO Alloy," *Chemistry of Materials*, 2021, doi: 10.1021/acs.chemmater.1c03938.

[45] P. C. Quayle, K. He, J. Shan, and K. Kash, "Synthesis, lattice structure, and band gap of ZnSnN2," *MRS Commun*, vol. 3, no. 3, pp. 135–138, 2013, doi: 10.1557/mrc.2013.19.

[46] A. N. Fioretti *et al.*, "Exciton photoluminescence and benign defect complex formation in zinc tin nitride," *Mater Horiz*, vol. 5, no. 5, pp. 823–830, Sep. 2018, doi: 10.1039/c8mh00415c.

[47] J. Pan, J. Cordell, G. J. Tucker, A. C. Tamboli, A. Zakutayev, and S. Lany, "Interplay between Composition, Electronic Structure, Disorder, and Doping due to Dual Sublattice Mixing in Nonequilibrium Synthesis of ZnSnN 2 :O," *Advanced Materials*, vol. 31, no. 11, Mar. 2019, doi: 10.1002/adma.201807406.

[48] M. Ohring, *Materials science of thin films*. Academic press, 2002.

[49] J. Mahan, *Physical Vapor Deposition of Thin Films*. New York: Wiley, 2000.

[50] P. Sigmund, "2. Sputtering by Ion Bombardment: Theoretical Concepts."

[51] F. Mirani, M. Passoni, C. S. Casari, and V. Dossena, "Politecnico di Milano - Department of energy doctoral programme in energy and nuclear science and

technology numerical and experimental investigation of laser-driven radiation sources for materials characterization the chair of the doctoral program: year 2021-cycle xxxiii."

[52] P. Sigmund, "Theory of Sputtering. I. Sputtering Yield of Amorphous and Polycrystalline Targets," *Physical Review*, vol. 184, no. 2, pp. 383–416, Aug. 1969, doi: 10.1103/PhysRev.184.383.

[53] J. P. Sibilia, *A guide to materials characterization and chemical analysis*. 1988.

[54] W. E. Kosimaningrum, "Modification of Carbon Felt for Contruction of Air-Breathing Cathode and Its Application in Microbial Fuel Cell," Université Montpellier, 2018.

[55] A. Ul-Hamid, *A Beginners' Guide to Scanning Electron Microscopy*. Cham: Springer International Publishing, 2018. doi: 10.1007/978-3-319-98482-7.

[56] D. Brandon and W. D. Kaplan, "Microstructural Characterization of Materials 2nd Edition."

[57] N. B. Colthup, L. H. Daly, and S. E. Wiberley, *Introduction to infrared and raman spectroscopy*. 1975.

[58] L. Ian R and E. Howell, *Handbook of Raman spectroscopy: from the research laboratory to the process line*. CRC Press, 2001.

[59] Y. C. Cho and S. Il Ahn, "Fabricating a Raman spectrometer using an optical pickup unit and pulsed power," *Sci Rep*, vol. 10, no. 1, Dec. 2020, doi: 10.1038/s41598-020-68650-7.

[60] P. E. J. Flewitt and R. K. Wild, *Physical Methods for Materials Characterisation*. CRC Press, 2015. doi: 10.1201/b20721.

[61] D. N. Stratis-Cullum, "Enabling Technologies for Point and Remote Sensing of Chemical and Biological Agents Using Surface Enhanced Raman Scattering (SERS) Techniques," 2009. [Online]. Available: https://www.researchgate.net/publication/235158125

[62] G. Artioli, "X-ray Diffraction (XRD)," in *Encyclopedia of Geoarchaeology*, 2017, pp. 1019–1025. doi: 10.1007/978-1-4020-4409-0_29.

[63] P. Gondoni, C. S. Casari Andrea Li Bassi, and C. E. Bottani, "Nanostructured Transparent Conducting Oxides for Advanced Photovoltaic Applications Year 2014-Cycle XXVI."

[64] L. J. van der Pauw, "A method of measuring the resistivity and Hall coefficient on lamellae of arbitrary shape, Philips technical review," 1958.

[65] O. Stenzel and M. Ohlídal, "Optical Characterization of Thin Solid Films ," in *Springer Series in Surface Sciences book*, vol. 64, Springer International Publishing AG, 2018.

[66] "TU Wien."

[67] J. W. Choi *et al.*, "Oxidation-Resistant Amorphous Zinc Tin Nitride Films with Tunable Optical and Electrical Properties," *Chemistry of Materials*, vol. 34, no. 15, pp. 6802–6808, Aug. 2022, doi: 10.1021/acs.chemmater.2c00940.

[68] T. K. Subramanyam, B. S. Naidu, and S. Uthanna, "E€ect of substrate temperature on the physical properties of DC reactive magnetron sputtered ZnO ®lms."

[69] A. Trapalis, J. Heffernan, I. Farrer, J. Sharman, and A. Kean, "Structural, electrical, and optical characterization of as grown and oxidized zinc nitride thin films," *J Appl Phys*, vol. 120, no. 20, Nov. 2016, doi: 10.1063/1.4968545.

[70] F. Ye *et al.*, "Electrical and optical properties of nanocrystalline ZnSnN2," *Thin Solid Films*, vol. 772, May 2023, doi: 10.1016/j.tsf.2023.139804.

[71] N. Beddelem *et al.*, "Structural and functional properties of Zn(Ge,Sn)N2 thin films deposited by reactive sputtering Structural and functional properties of Zn(Ge,Sn)N 2 thin films deposited by reactive sputtering," *Thin Solid Films*, vol. 709, 2020, doi: 10.1016/j.tsf.2020.138192ï.

[72] S. Mahieu, R. De Gryse, D. Depla, and P. Ghekiere, "Biaxial alignment in sputter deposited thin films," *Thin Solid Films 515* , pp. 1229-1249., 2006.

[73] *Surface and Coatings Technology*, vol. 359. 2019.

[74] "alfa-Sn Fd-3m:1 cod_database_code 7222459 as input".

[75] "ZnO Fm-3m cod_database_code 1534836 as input".

[76] "ZnO P63mc cod_database_code 1011258 as input."

[77] S. Utamuradova, S. Daliyev, K. Fayzullayev, D. Rakhmanov, and Js. Zarifbayev, "RAMAN SPECTROSCOPY OF DEFECTS IN SILICON DOPED WITH CHROMIUM ATOMS," 2023.

[78] P. Mishra and K. P. Jain, "First- and second-order Raman scattering in nanocrystalline silicon," *Phys Rev B Condens Matter Mater Phys*, vol. 64, no. 7, pp. 733041–733044, Aug. 2001, doi: 10.1103/PhysRevB.64.073304.

[79] D. Usanov *et al.*, "Some insights into the mechanism of photoluminescence of As-S-based films synthesized by PECVD," *J Non Cryst Solids*, vol. 513, pp. 120–124, Jun. 2019, doi: 10.1016/j.jnoncrysol.2019.03.015.

[80] Tauc, *AMORPHOUS AND LIQUID SEMICONDUCTORS Edited by PLENUM PRESS. LONDON AND NEW YORK. 1974*. 1974.

[81] T. Wang, C. Ni, and A. Janotti, "Band alignment and p-type doping of ZnSnN2," *Phys Rev B*, vol. 95, no. 20, May 2017, doi: 10.1103/PhysRevB.95.205205.

List of Figures

List of Tables

Ringraziamenti

Ringrazio i miei genitori, Laura ed Andrea, per avermi "educato" alla curiosità sin da piccolo e per avermi sempre spronato ed appoggiato durante questo percorso. Ringrazio mio fratello Filippo, parte essenziale della mia vita. Ringrazio tutta la mia famiglia per essere sempre stata presente. Ringrazio me stesso, per averci sempre creduto. Ringrazio i miei amici e compagni di corso, senza i quali, questo periodo sarebbe stato meno gioioso. Ringrazio il professor David Dellasega per avermi dato l'opportunità di aver fatto ricerca su un argomento così interessante ed attuale. Ringrazio la dottoressa Cristina Mancarella e il dottor Davide Vavassori per esser sempre stati disponibili ed avermi seguito durante questo lavoro di tesi.

Ringrazio mio nonno Carlo, che non è più fisicamente tra di noi, ma rimarrà sempre un punto di riferimento per me.